

ERCOFTAC

Bulletin

September 2012

92

European Research Community on Flow, Turbulence and Combustion

ERCOFTAC is a leading European association of research, education and industry groups in the technology of flow, turbulence and combustion. The main objectives of ERCOFTAC are: To promote joint efforts of European research institutes and industries with the aim of **exchanging technical and scientific information**; to promote **Pilot Centres** for collaboration, stimulation and

application of research across Europe; to stimulate, through the creation of **Special Interest Groups**, well-coordinated European-wide research efforts on specific topics; to stimulate the creation of advanced training activities; and to be influential on funding agencies, governments, the European Commission and the European Parliament.

www.ercoftac.org

Honorary Presidents

Mathieu, J. Spalding, D.B.

Executive Committee

Chairman

Hutton, A.G.
Airbus UK
Building 09B
Bristol BS99 7AR
United Kingdom
Tel: +44 117 936 7519
anthony.hutton@airbus.com

Deputy Chairman

Tomboulides, A.

Deputy Chairman

Hirsch, C.

Treasurer

Duursma, R.P.J.

Deputy Treasurer

Ooms, G.

SPC Chairman

Geurts, B.J.

SPC Deputy Chairman

Von Terzi, D.

IPC Chairman

Geuzaine, P.

IPC Deputy Chairman

Oliemans, R.V.A.

Horizon 10 Chairman

Jakirlic, S.

Ind. Engagement Officer

Seoud, R.E.

Knowledge Base Editor

Rodi, W.

Bulletin Editor

Elsner, W.

Observer

Hunt, J.

Observer

Jacquin, L.

Secretary

Borhani, N.

ERCOFTAC Seat of the Organisation

Director

Hirsch, C.
Numea International
Chaussée de la Hulpe 189
Terhulpesteenweg
B-1170 Brussels
Belgium
Tel: +32 2 643 3572
Fax: +32 2 647 9398
ado@ercoftac.be

Secretaries

Bongaerts, S.
stephane.bongaerts@ercoftac.be
Laurent, A.
anne.laurent@ercoftac.be

Scientific Programme Committee

Chairman

Geurts, B.J.
University of Twente
Mathematical Sciences
PO Box 217
NL-7500 AE Enschede
The Netherlands
Tel: +31 53 489 4125
b.j.geurts@utwente.nl

Deputy Chairman

Von Terzi, D.

Industrial Programme Committee

Chairman

Geuzaine, P.

Deputy Chairman

Oliemans, R.V.A.

Engagement Officer

Seoud, R.E.
ERCOFTAC
Crown House
72 Hammersmith Road
London W14 8TH
United Kingdom
Tel: +44 207 559 1430
Fax: +44 207 559 1428
richard.seoud-ieo@ercoftac.org

ERCOFTAC Central Administration Development & Outreach

ERCOFTAC CADO
Crown House
72 Hammersmith Road
London W14 8TH
United Kingdom
Tel: +44 207 559 1427
Fax: +44 207 559 1428

CADO Manager and Industrial Engagement Officer

Richard Seoud
Tel: +44 207 559 1430
Richard.Seoud-ieo@ercoftac.org

Admin Manager

Magdalena Jakubczak
Tel: +44 207 559 1429
Fax: +44 207 559 1428
magdalena.jakubczak@ercoftac.org

TABLE OF CONTENTS

Introduction to the Special Theme Synthetic Turbulence Models <i>F.C.G.A. Nicolleau and A.F. Nowakowski</i>	3
Randomisation and Phase Coherence in Quasi-Homogeneous Turbulence, and Interactions <i>C. Cambon</i>	4
Manufactured Turbulence with Langevin Equations <i>A. A. Mishra and S. Girimaji</i>	11
Subgrid-scale Statistics in Synthetic Helical Turbulent Fields Generated by the Multi-scale Turnover Lagrangian Map <i>Y. Li and C. Rosales</i>	16
Singularities in the Particle Concentration Field of Inertial Particles in Turbulent Flows <i>E. Meneguz and M. W. Reeks</i>	22
Clustering of Laden Particles in Kinematic Simulation Flows <i>F.C.G.A. Nicolleau, M. Farhan, and A.F. Nowakowski</i>	27
On the Complex Motion of Inertial Particles Near Unsteady Vortices <i>J. R. Angilella, T. Nizkaya and M. Bués</i>	32
Applications of Synthetic Turbulence to Filament Models of Magnetic Flux Ropes and Quantum Turbulence <i>A. Baggaley</i>	35
Synthetic Turbulence via the Minimal Lagrangian Map <i>C. Rosale</i>	41



Over the two days, ERCOFTAC will hold its scientific meetings and committee meetings at the Adriatico Guest House. For the 25th of October 2012, ERCOFTAC has coordinated a set of pertinent talks, with our local host Prof. V. Armenio, in order to present a picture of FTAC, in Italy. Thereafter, the Leonardo da Vinci Award takes place, and here we have five finalists. Each finalist will deliver a presentation on a topic that is underpinned by their PhD research programme. On the next page one can observe full programme details.

On the 26th of October, ERCOFTAC conducts its committee meetings, where in the morning we have the SPC and IPC meetings, followed in the afternoon by the MB-GA meeting. Continual member participation in these meetings is as ever key to ERCOFTAC's progress, as we are here to serve and explore your needs and views in FTAC.

EDITOR	Marek, M.
TECHNICAL EDITOR	Kuban, Ł.
CHAIRMAN	Elsner, W.
EDITORIAL BOARD	Armenio, V. Dick, E. Geurts, B.J.
DESIGN & LAYOUT	Borhani, N. Nichita, B.A.
COVER DESIGN	Aniszewski, W.
SUBMISSIONS	
ERCOFTAC Bulletin Institute of Thermal Machinery Czestochowa University of Technology Al. Armii Krajowej 21 42-201 Czestochowa Poland	
Tel:	+48 34 3250 507
Fax:	+48 34 3250 507
Email:	ercoftac@imc.pcz.czest.pl

HOSTED, PRINTED & DISTRIBUTED BY



CZESTOCHOWA UNIVERSITY OF TECHNOLOGY

The reader should note that the Editorial Board cannot accept responsibility for the accuracy of statements made by any contributing authors

A note from the Editor:

We would like to apologize for the mistaken number on the cover of the March 2012 issue (paper version only).

The correct number is, of course, 90 and the successive issues are numbered from there to retain the continuity with the previous issues of the Bulletin.



The ERCOFTAC Best Practice Guidelines for Industrial Computational Fluid Dynamics

The Best Practice Guidelines (BPG) were commissioned by ERCOFTAC following an extensive consultation with European industry which revealed an urgent demand for such a document. The first edition was completed in January 2000 and constitutes generic advice on how to carry out quality CFD calculations. The BPG therefore address mesh design; construction of numerical boundary conditions where problem data is uncertain; mesh and model sensitivity checks; distinction between numerical and turbulence model inadequacy; preliminary information regarding the limitations of turbulence models etc. The aim is to encourage a common best practice by virtue of which separate analyses of the same problem, using the same model physics, should produce consistent results. Input and advice was sought from a wide cross-section of CFD specialists, eminent academics, end-users and, (particularly important) the leading commercial code vendors established in Europe. Thus, the final document can be considered to represent the consensus view of the European CFD community.

Inevitably, the Guidelines cannot cover every aspect of CFD in detail. They are intended to offer roughly those 20% of the most important general rules of advice that cover roughly 80% of the problems likely to be encountered. As such, they constitute essential information for the novice user and provide a basis for quality management and regulation of safety submissions which rely on CFD. Experience has also shown that they can often provide useful advice for the more experienced user. The technical content is limited to single-phase, compressible and incompressible, steady and unsteady, turbulent and laminar flow with and without heat transfer. Versions which are customised to other aspects of CFD (the remaining 20% of problems) are planned for the future.

The seven principle chapters of the document address numerical, convergence and round-off errors; turbulence modelling; application uncertainties; user errors; code errors; validation and sensitivity tests for CFD models and finally examples of the BPG applied in practice. In the first six of these, each of the different sources of error and uncertainty are examined and discussed, including references to important books, articles and reviews. Following the discussion sections, short simple bullet-point statements of advice are listed which provide clear guidance and are easily understandable without elaborate mathematics. As an illustrative example, an extract dealing with the use of turbulent wall functions is given below:

- Check that the correct form of the wall function is being used to take into account the wall roughness. An equivalent roughness height and a modified multiplier in the law of the wall must be used.
- Check the upper limit on y^+ . In the case of moderate Reynolds number, where the boundary layer only extends to y^+ of 300 to 500, there is no chance of accurately resolving the boundary layer if the first integration point is placed at a location with the value of y^+ of 100.

- Check the lower limit of y^+ . In the commonly used applications of wall functions, the meshing should be arranged so that the values of y^+ at all the wall-adjacent integration points is only slightly above the recommended lower limit given by the code developers, typically between 20 and 30 (the form usually assumed for the wall functions is not valid much below these values). This procedure offers the best chances to resolve the turbulent portion of the boundary layer. It should be noted that this criterion is impossible to satisfy close to separation or reattachment zones unless y^+ is based upon y^* .
- Exercise care when calculating the flow using different schemes or different codes with wall functions on the same mesh. Cell centred schemes have their integration points at different locations in a mesh cell than cell vertex schemes. Thus the y^+ value associated with a wall-adjacent cell differs according to which scheme is being used on the mesh.
- Check the resolution of the boundary layer. If boundary layer effects are important, it is recommended that the resolution of the boundary layer is checked after the computation. This can be achieved by a plot of the ratio between the turbulent to the molecular viscosity, which is high inside the boundary layer. Adequate boundary layer resolution requires at least 8-10 points in the layer.

All such statements of advice are gathered together at the end of the document to provide a 'Best Practice Checklist'. The examples chapter provides detailed expositions of eight test cases each one calculated by a code vendor (viz FLUENT, AEA Technology, Computational Dynamics, NUMECA) or code developer (viz Electricité de France, CEA, British Energy) and each of which highlights one or more specific points of advice arising in the BPG. These test cases range from natural convection in a cavity through to flow in a low speed centrifugal compressor and in an internal combustion engine valve.

Copies of the Best Practice Guidelines can be acquired from:

ERCOFTAC CADO
Crown House
72 Hammersmith Road
London W14 8TH, United Kingdom
Tel: +44 207 559 1429
Fax: +44 207 559 1428
Email: Richard.Seoud-ieo@ercoftac.org

The price per copy (not including postage) is:

ERCOFTAC members		
First copy		Free
Subsequent copies		45 Euros
Students		30 Euros
Non-ERCOFTAC academics		
		75 Euros
Non-ERCOFTAC industrial		
		150 Euros

INTRODUCTION TO THE SPECIAL THEME SYNTHETIC TURBULENCE MODELS

F.C.G.A. Nicolleau and A.F. Nowakowski

*Sheffield Fluid Mechanic Group, University of Sheffield, Department of Mechanical Engineering
Mappin Street, Sheffield S1 3JD, United Kingdom.*

The special interest group on ‘Synthetic Turbulence Model’ SIG42, is relatively recent. It was established in 2008 as an offshoot of SIG35 which is devoted to ‘Multipoint Turbulence Structure’¹.

SIG35 focuses on fundamental Eulerian descriptions of turbulence, by contrast SIG42 aims first at Lagrangian applications. For such applications, an Eulerian accurate description is not paramount as long as the details of the Eulerian field have little effect on the Lagrangian predictions. As far as these predictions are concerned, the Eulerian velocity and hence the resolution of the Navier Stokes equations is not necessary per se. So an ultimate very economical way of generating Lagrangian trajectories is to build ad hoc analytical ‘pseudo-Eulerian’ fields that can be easily integrated. This is what is meant by ‘Synthetic Turbulence Models’ (STM).

It may seem obvious that specific approaches and modelling tactics are needed when it comes to Lagrangian problems and that Eulerian structures (as referred to in SIG35) and Lagrangian structures (as needed in SIG42) may be two separate things. However, it was only after the IMS/ERCOFTAC/SIG 35/COST 20 workshop, at Imperial College London, in 2007 that it was decided to create an independent SIG for what was then mainly referred to as Kinematic Simulations (KS). These latter have now become a particular case of a much wider Synthetic Turbulence Modelling (STM) community.

The modelling strategy involved in STM and the difference between the ‘flow structure’ needed for Lagrangian predictions and the ‘Multipoint Turbulence Structure’ that SIG35 is referring to is particularly salient in the problem of stratified flows. This remains an important area of application of synthetic turbulence models (see e.g the second contribution). The recognition of the determinant role of the linear terms in the capping of the vertical dispersion of particles in stratified flows owes a lot to the different KS studies conducted on this subject. So that apart from SIG35, SIG14² has always been an important partner of SIG42.

This special theme bulletin reflects the variety of problems tackled using some Synthetic Models of Turbulence. Theoretical issues about the generations of synthetic flows are reflected in the first three papers:

- Randomisation and phase coherence in quasi-homogeneous turbulence, and interactions
by C. Cambon *Ecole Centrale de Lyon, France*
- Manufactured Turbulence with Langevin equations
by A. A. Mishra and S. Girimaji *Aerospace Engineering Department, Texas A&M University, College Station, Texas, USA*

- Subgrid-scale statistics in synthetic helical turbulent fields generated by the multi-scale turnover Lagrangian map
by Y. Li and C. Rosales *School of Mathematics and Statistics, University of Sheffield, UK, Universidad Tecnica Federico Santa Maria, Chile*

An important area of application of STM has been the study of the effect of particle inertia on concentration and clustering as reflected in the next three contributions:

- Singularities in the particle concentration field of inertial particles in turbulent flows
by E. Meneguz & M. W. Reeks *School of Mechanical and Systems Engineering, Newcastle University, UK*
- Clustering of laden particles in Kinematic Simulation flows
by F.C.G.A. Nicolleau, M. Farhan, and A.F. Nowakowski *Sheffield Fluid Mechanic Group, Sheffield UK*
- On the Complex Motion of Inertial Particles Near Unsteady Vortices.
by J.-R. Angilella, T. Nizkaya & M. Buès *Nancy-Université, LAEGO, France*

Beyond applications to classical turbulence, KS have been widely applied to superfluids as illustrated in the next paper:

- Applications of synthetic turbulence to filament models of magnetic flux ropes and quantum turbulence
by A. Baggaley *School of Mathematics and Statistics Newcastle University, UK*

If KS remains a popular approach it is not by far the only synthetic turbulence model. More refined models exist as illustrated in the last contribution:

- Synthetic Turbulence via the Minimal Lagrangian Map
by C. Rosales *Department of Mechanical Engineering, Universidad Técnica Federico Santa María, Chile.*

This introduction only gives an overview of SIG42 activities. There are more, in particular it is worth mentioning the recent extension of KS to channel flows [2] as a first attempt at including wall effects.

We would like to take the opportunity of this first special theme bulletin to thanks ERCOFTAC for its constant support of SIG42’s activities.

References

- [1] Cambon, C.: Special Theme : Multipoint Turbulence Structure and Modelling. *Ercoftac Bul.* **88** (2011).
- [2] Clark, N.R., Vassilicos, J.C.: Kinematic Simulation of Fully Developed Turbulent Channel Flow. *Flow Turbulence Combustion* **86**, 263-293 (2011). doi:10.1007/s10494-010-9316-x

¹SIG35 coordinated by C. Cambon was the subject of a recent special theme in 2011 [1]

²SIG14 devoted to Stably Stratified and Rotating Flows is coordinated by J.M. Redondo

RANDOMISATION AND PHASE COHERENCE IN QUASI-HOMOGENEOUS TURBULENCE, AND INTERACTIONS

C. Cambon

*Laboratoire de Mécanique des Fluides et d'Acoustique, UMR 5509
École Centrale de Lyon, 69134 Ecully cedex, France*

1 Introduction

Kinematic Simulation is an important theme for SIG 42. The generation of synthetic turbulence models by a superposition of random Fourier modes is a very old procedure. Following pioneering studies by Kraichnan [14], a practical model was proposed by Fung *et al.* [10] with application to Lagrangian diffusion. Surprisingly, the same model has been used by several authors until now *without the smallest change* for various applications, from Lagrangian diffusion to aeroacoustics. Several improvements are discussed in a recent paper [6], accounting for anisotropy and linear dynamics, or Spectral linear Theory (SLT) as generalized Rapid Distortion Theory. Prescription of a unique energy spectrum, or $E(k)$, in isotropic turbulence, can be replaced by prescription of the most general set of basic spectra for generating second-order two-point statistics of homogeneous, arbitrary anisotropic, incompressible turbulence: energy (but with directional anisotropy) / polarization / helicity ($\mathbf{e}(\mathbf{k}), Z(\mathbf{k}), \mathcal{H}(\mathbf{k})$) decomposition [3].

Refinement of the spectral description of anisotropic turbulence at the second order is associated with construction of individual realizations of the velocity field, in which randomization is given again by synthetic phases. On the one hand, randomization is useful for creating a large set of realizations, to which an ensemble average, denoted by brackets from now on, can be applied. This is discussed in connection with initialization of DNS, in which random phases are introduced, but for *a single* realization of initial data.

On the other hand, independently of the way of introducing synthetic phases in individual realizations, spatial two-point second-order correlations lose some *real phase* information. This is obvious in homogeneous turbulence using Fourier space, but a similar statement can be established in the POD decomposition of the spatial two-point correlation in inhomogeneous turbulence, as pointed out by Lumley. Such a drawback was overcome by him through the consideration of three-point statistics under certain conditions [17].

Importance of three-point cubic correlations is demonstrated in a recent paper on anisotropic homogeneous turbulence [7], and we will emphasize here some related general features using new insights from pod, and revisit connections with KS and DNS in Fourier space. As our best example, phase coherence of three-point cubic velocity correlations is essential for understanding the dynamics of decaying rotating turbulence. Even if we agree with the Davidson's group on the creation of inhomogeneous structures from compact sources by purely linear dynamics, we think that the effect of three-point cubic correlations — with their crucial phase information — is not correctly accounted for in their interpretation of the decay of rotating homogeneous turbulence [26]. The case of

homogeneous rotating turbulence is addressed in section 3, and contrasted to more general cases of rotating shear flows. In addition, the very subtle saturated transition from 3D to 2D structure, shown in rotating turbulence, is contrasted with a complete two-dimensionalization obtained in quasi-static magnetohydrodynamics, allowing a mutual better physical understanding in both cases.

Since our favorite theme is essentially homogeneous turbulence with extensive use of 3D Fourier space, why looking first at POD decomposition? Firstly, I remain very grateful to Marie-Pierre Chauve for an enlightening talk, given many years ago (1987) almost without any sophisticated mathematical tool, for POD applied to transition to turbulence on a rotating flat disk (e.g. [1] for mathematical details). Key concepts, such as the degree of randomization, possibly measured by a dedicated entropy, can be introduced at a better degree of generality than in Fourier space. It is generally said that POD modes naturally reduce to Fourier modes in homogeneous turbulence, but nothing is said on the diagonalization of two-point second order spectral tensors, which is a natural application of the analysis in principal components, or POD, diagonalization which can be shown as a byproduct of our ($\mathbf{e}(\mathbf{k}), Z(\mathbf{k}), \mathcal{H}(\mathbf{k})$)-decomposition. Accordingly, a very simple review of POD tools, following Marie-Pierre Chauve, give a new insight to some procedures used in anisotropic theory carried out in Fourier space, with application to pseudo-spectral DNS and KS.

This paper, or essay, is organised as follows. A caricature of POD is given in section 2, application to second order statistics in Fourier space, diagonalizing the spectral tensor and discussing what degree of randomness is reflected in it, from DNS and KS as well. The main theme of cubic correlations in dynamics is addressed in section 4, and section 5 is devoted to conclusions and perspectives.

2 Starting from a caricature of POD analysis

As a first example, let us consider a N -component vector denoted a_i , $i = 1, N$. The dyadic second-order tensor, $R_{ij} = a_i a_j$, or $\mathbf{R} = \mathbf{a} \otimes \mathbf{a}$, is first considered looking at its intrinsic diagonalized representation. This tensor, obviously of rank 1, is thus characterized by a single nonzero eigenvalue, equal to $a_n a_n$, so that its diagonalized form is

$$\mathbf{R} = \begin{pmatrix} a_n a_n & 0 & \dots & 0 \\ 0 & 0 & \dots & 0 \\ \dots & \dots & \dots & \dots \\ 0 & 0 & \dots & 0 \end{pmatrix}. \quad (1)$$

This structure is easily found by calculating the determinant

$$\text{Det}(\mathbf{a} \otimes \mathbf{a} - \lambda \mathbf{I}) = \lambda^{N-1} (a_n a_n - \lambda).$$

Of course, the unique non-zero eigenvalue has the vector \mathbf{a} as its eigenvector, according to

$$(a_i a_j) a_j = (a_n a_n) a_i, \quad (2)$$

whereas the subspace of rank $N - 1$ related to the $N - 1$ -multiple 0 eigenvalue is just the subspace of vectors *normal* to \mathbf{a} , such that $(a_i a_j) v_j = 0$.

Only when statistical averaging is applied, it is possible to give rise to N nonzero positive different eigenvalues, $s_1^2, s_2^2, \dots, s_N^2$, with $\langle a_n a_n \rangle = \sum_{i=1, N} s_i^2$, and with the following diagonal form

$$\langle \mathbf{R} \rangle = \begin{pmatrix} s_1^2 & 0 & \dots & 0 \\ 0 & s_2^2 & \dots & 0 \\ \dots & \dots & \dots & \dots \\ 0 & 0 & \dots & s_N^2 \end{pmatrix}. \quad (3)$$

By ensemble averaging, the tensor $\langle a_i a_j \rangle$ recovers a possible rank N , with different N eigenvalues related to an orthogonal eigenframe, because the averaged tensor is definite positive. The obvious relationship that gave $a_n a_n$ as the unique nonzero eigenvalue with eigenvector \mathbf{a} no longer works in average because

$$\langle a_i a_j \rangle \langle a_j \rangle \neq \langle a_n a_n \rangle \langle a_i \rangle,$$

in general.

This simple decomposition applies to an Hermitian tensor, with a_i a complex vector with complex conjugate a_i^* : The non-averaged Hermitian tensor $a_i a_j^*$ has a single nonzero eigenvalue $a_n a_n^*$, related to the eigenvector \mathbf{a} . Only by statistical averaging, the spectrum of eigenvalues $a_n a_n^*, 0, \dots, 0$ can be populated by N different real positive eigenvalues s_1, s_2, \dots, s_n , whose sum is $\langle a_n a_n^* \rangle$.

The Reynolds stress tensor is found for $\mathbf{a} = \mathbf{u}$, the velocity fluctuation. Without averaging, the unique nonzero eigenvalue is twice the kinetic energy q^2 , and the set of eigenvalues is $(q^2, 0, 0)$. This value q^2 is dispatched among the three eigenvalues when statistical averaging holds. The maximum dispatching is obtained in the isotropic case with the three eigenvalues equal to $q^2/3$.

More generally, the so-called POD decomposition, or analysis in principal components revisited by John Lumley in fluid mechanics, gives a systematic ranking of eigenvalues $s_1^2 > s_2^2 > \dots > s_N^2$. For instance, a very interesting study of turbulence in rotating discs was performed by Aubry *et al.* [1], in which a_i represent a set of scalar velocity components at different discrete radial positions, $a_i \sim v(r_i)$. In this case, the rapid decrease of the spectrum of eigenvalues characterizes an optimal ranking of the most energetic structures. It is possible to define an entropy, which is zero in the deterministic case, with all the energy concentrated on the single nonzero eigenvalue, and increases in term of less peaked distribution of the spectrum of eigenvalues. Maximum entropy is found at equipartition, when all the eigenvalues are equal. In our oversimplified example, total energy is $E = (1/2) \mathbf{a} \cdot \mathbf{a}$, $E = (1/2) \sum_{n=1}^N s_n^2$ and the ‘‘entropy’’ is

$$H = -\frac{1}{\ln N} \sum_{n=1}^N p_n \ln p_n, \quad \text{with } p_n = \frac{s_n^2}{2E}.$$

Deterministic (dyadic) case and equidistribution correspond to $H = 0$ (minimum) and $H = 1$ respectively. Note that the high concentration of total energy in terms of a little number of decreasing eigenvalues in various pod analyses is not a characteristic of increasing (statistical)

inhomogeneity in the flow, as often said, but more generally a characteristic of decreasing randomness. Going back to the Reynolds stress tensor, isotropy is related to maximum randomness, whereas the strong dominance of a single eigenvalue reflects a dominant deterministic effect. This is shown with kinetic energy concentrated on the streamwise component of the RST in a — highly non-homogeneous — wall-bounded flow, but a similar effect is obtained from the sole effect of the mean shear in the quasi-deterministic rapid distortion context.

3 Revisiting the structure of homogeneous turbulence, via the second-order spectral tensor

3.1 Second-order statistics, continuous and discrete formulation

We will now consider the most general two-point and single-point second-order statistics. All this information derives in physical space from the correlation tensor

$$R_{ij}(\mathbf{r}) = \langle u_i(\mathbf{x}) u_j(\mathbf{x} + \mathbf{r}) \rangle, \quad (4)$$

which only depends on the separation vector \mathbf{r} assuming statistical homogeneity. Its 3D Fourier transform gives the second-order spectral tensor

$$\hat{R}_{ij}(\mathbf{k}) = \frac{1}{(2\pi)^3} \iiint_{-\infty}^{\infty} R_{ij}(\mathbf{r}) \exp(-i\mathbf{k} \cdot \mathbf{r}) d^3 \mathbf{r}, \quad (5)$$

in the continuous case, and similarly in the discrete case, using integrals over the periodic domain: The velocity field is periodized in the three directions of space, so that the components of the wave-vector are discretized as

$$k_{n_1} = n_1(2\pi)/L_1, \quad k_{n_2} = n_2(2\pi)/L_2, \quad k_{n_3} = n_3(2\pi)/L_3,$$

with n_1, n_2, n_3 a set of relative integers.

Of course, the same information is included in \mathbf{R} and $\hat{\mathbf{R}}$, but the latter presents a simpler structure due to the algebraic form of the divergence-free constraint in 3D Fourier space. Using the reduced rank of the velocity vector in Fourier space, the spectral tensor is shown to be rank-2 using

$$\langle \hat{u}_i^*(\mathbf{p}) \hat{u}_j(\mathbf{k}) \rangle = \hat{R}_{ij}(\mathbf{k}) \delta^3(\mathbf{k} - \mathbf{p}), \quad (6)$$

and $k_i \hat{u}_i(\mathbf{k}) = 0$. Using, e.g., DNS, the discrete counterpart of the preceding equation is

$$\langle \hat{u}_i^*(\mathbf{k}_m) \hat{u}_j(\mathbf{k}_n) \rangle = \hat{R}_{ij}(\mathbf{k}_n) \delta_{nm} \frac{L_1 L_2 L_3}{(2\pi)^3}, \quad (7)$$

with often $L_1 = L_2 = L_3 = L$. We prefer not use the conventional short-hand notation $L = 2\pi$ of DNS, in order to display the correct dimension for both the Dirac delta ‘function’ in (6) and the prefactor $(L/(2\pi))^3$ in (7).

From the most general definition of the spectral tensor, Hermitian definite-positive, with $k_i \hat{R}_{ij} = \hat{R}_{ij} k_j = 0$ (incompressibility from $k_i \hat{u}_i = 0$), is found its explicit rank-2 form:

$$\hat{\mathbf{R}} = \begin{pmatrix} e - \Re Z & \Im Z + i\mathcal{H} & 0 \\ \Im Z - i\mathcal{H} & e + \Re Z & 0 \\ 0 & 0 & 0 \end{pmatrix} = \begin{pmatrix} e - \mathcal{H} & Z & 0 \\ Z^* & e + \mathcal{H} & 0 \\ 0 & 0 & 0 \end{pmatrix}. \quad (8)$$

The first expression is found in the orthonormal Craya-Herring frame of reference ($\mathbf{e}^{(1)}, \mathbf{e}^{(2)}, \mathbf{e}^{(3)}$), so that the third line and the third column correspond to the direction of \mathbf{k} , along $\mathbf{e}^{(3)} = \mathbf{k}/k$. The reduced non-zero contribution in the plane normal to \mathbf{k} is generated by four real scalar terms, the 3D spectrum of energy $e(\mathbf{k}) = (1/2)\hat{R}_{ii}$, depending on the full vector \mathbf{k} in arbitrary anisotropic flow, the 3D helicity spectrum $k\mathcal{H}(\mathbf{k}) = \imath k_n \epsilon_{nij} \hat{R}_{ij}$, and the polarization term $Z = (1/2)\hat{R}_{ij} N_i^* N_j^*$. The last term is complex-valued and appears in a more intrinsic form in the second expression in (8), using the frame of helical modes ($\mathbf{N} = \mathbf{e}^{(2)} - \imath \mathbf{e}^{(1)}, \mathbf{N}^* = \mathbf{e}^{(2)} + \imath \mathbf{e}^{(1)}, \mathbf{e}^{(3)}$) derived from the Craya-Herring frame [3, 24]. It is clear that its modulus $|Z|$ is invariant to any change of orthonormal frame of reference, as e and \mathcal{H} are.

The exact splitting of the spectral tensor in terms of four contributions, a purely isotropic one (iso), a contribution from directional anisotropy (dir), a contribution from polarization anisotropy (pol) and a contribution from helicity (hel) comes from a trace-deviator decomposition but restricted to the plane normal to \mathbf{k} , so that

$$\begin{aligned} \hat{R}_{ij} = & \underbrace{\frac{E(k)}{4\pi k^2} P_{ij}(\mathbf{k})}_{\hat{\mathbf{R}}^{(iso)}} + \underbrace{\left(e(\mathbf{k}) - \frac{E(k)}{4\pi k^2} \right) P_{ij}(\mathbf{k})}_{\hat{\mathbf{R}}^{(dir)}} \\ & + \underbrace{\Re(Z(\mathbf{k}) N_i(\mathbf{k}) N_j(\mathbf{k}))}_{\hat{\mathbf{R}}^{(pol)}} + \underbrace{\imath \epsilon_{ijn} \frac{k_n}{k} \mathcal{H}(\mathbf{k})}_{\hat{\mathbf{R}}^{(hel)}}. \end{aligned} \quad (9)$$

Without looking at the detail of the helical base, the decomposition is completely intrinsic with $\hat{R}_{ij}^{(iso)} + \hat{R}_{ij}^{(dir)} = (1/2)\hat{R}_{nn} P_{ij}$, $\hat{R}_{ij}^{(pol)} = \Re(\hat{R}_{ij} - (1/2)\hat{R}_{nn} P_{ij})$ and $\hat{R}_{ij}^{(hel)} = \imath \Im(\hat{R}_{ij} - (1/2)\hat{R}_{nn} P_{ij})$, using the projection operator $P_{ij} = \delta_{ij} - k_i k_j / k^2 = \Re(N_i^* N_j)$. This above decomposition is reflected in any two-point, in physical and in Fourier space, or single-point statistical descriptor.

Due to the reduced rank-2 form of the spectral tensor, diagonalisation is very easy to perform, with two nonzero (in general) positive eigenvalues given by the trace and the determinant of the non-zero part of the matrix in (8): $s_1^2 + s_2^2 = 2e$, $s_1^2 s_2^2 = e^2 - |Z|^2 - \mathcal{H}^2$. Accordingly,

$$s_1^2 = e + \sqrt{|Z|^2 + \mathcal{H}^2}, \quad s_2^2 = e - \sqrt{|Z|^2 + \mathcal{H}^2}. \quad (10)$$

A general realisability condition is found as

$$e \geq \sqrt{|Z|^2 + \mathcal{H}^2}. \quad (11)$$

3.2 Conventional DNS started with a single realization

It is important to point out that conventional pseudo-spectral DNS started with a single realisation, even using — a unique — random set of phases, give no access to the statistical definition of $\hat{\mathbf{R}}$, but only to its dyadic form

$$\hat{R}_{ij}^{DNS}(\mathbf{k}_{n_1 n_2 n_3}) = \hat{\mathbf{u}}_i^*(\mathbf{k}_{n_1 n_2 n_3}) \hat{u}_j(\mathbf{k}_{n_1 n_2 n_3}) \frac{(2\pi)^3}{L_1 L_2 L_3},$$

so that further statistical averaging can be only obtained by spatial or temporal averaging.

What happens if the spectral tensor is dyadic, in the absence of effective statistical averaging, as in DNS

started with a single realisation? The nonzero part reduces to

$$\begin{pmatrix} u^{(1)*} u^{(1)} & u^{(1)*} u^{(2)} \\ u^{(1)} u^{(2)*} & u^{(2)*} u^{(2)} \end{pmatrix},$$

(e.g. using the nonzero, poloidal-toroidal-type, components of $\hat{\mathbf{u}}$ in the Craya-Herring frame,) so that the determinant, which gives the product of eigenvalues, with sum equal to the trace, is zero. Accordingly, the preceding inequality for realizability becomes an equality, $e = \sqrt{|Z|^2 + \mathcal{H}^2}$ and the only nonzero eigenvalue is $2e$, as in our more general model problem in POD caricature, section 2. In this case, the eigenvector related to the eigenvalue $2e$ is the velocity vector in Fourier space $\hat{\mathbf{u}}$, the second eigenvector attached to the zero eigenvalue $e - \sqrt{|Z|^2 + \mathcal{H}^2}$ is, said, $\mathbf{e}^{(3)} \times \hat{\mathbf{u}}$, and the third eigenvector is $\mathbf{e}^{(3)}$, or \mathbf{k} by virtue of incompressibility.

A more realistic randomness can be obtained in KS following [6].

Of course, this does not solve one of the main drawback of KS: Gaussian statistics is favoured, at least for the velocity field and probably for their increments.

4 Restoring cubic correlations in the dynamics of two-point second-order statistics

In conventional isotropic turbulence, it is clear that all information for two-point and single-point second-order statistics is given by the energy spectrum $E(k)$. It is well known that very different types of velocity realizations can have the same spectrum. For instance, a realistic ‘turbulent’ realization, with tube-like vortex structures, e.g. [12], is turned into an unstructured one, by multiplying the individual velocity Fourier modes by uncorrelated phases, or

$$\hat{\mathbf{u}}(\mathbf{k}) \rightarrow \hat{\mathbf{u}}(\mathbf{k}) e^{2\phi_{\mathbf{k}}}. \quad (12)$$

Of course, the realistic turbulent field and the ‘phase-randomized’ one have the same energy spectrum, according to (6) and (9) (first term).

From a dynamical viewpoint, the role of the nonlinear spectral transfer term in creating, or restoring, phase coherence, is essential, from the basic Lin equation

$$\frac{\partial E}{\partial t} + 2\nu k^2 E = T. \quad (13)$$

$T(k, t)$ is mediated by cubic velocity correlations and reflects the cascade process. Its triadic structure follows from the exact derivation of (13) from

$$\frac{\partial \hat{\mathbf{u}}}{\partial t} + \nu k^2 \hat{\mathbf{u}} + \mathbf{P} \widehat{\boldsymbol{\omega}} \times \hat{\mathbf{u}} = 0, \quad (14)$$

in which $\boldsymbol{\omega}$ is the vorticity fluctuation, and $\widehat{\cdot}$ denotes Fourier transform. Accordingly, the transfer term results from spherically averaging a contribution from $\langle \hat{u}_i(\mathbf{k}) \widehat{\omega}_n(\mathbf{p}) \hat{u}_m(\mathbf{q}) \rangle$, with $\mathbf{k} + \mathbf{p} + \mathbf{q} = 0$ using the expression of the Fourier transform of the Lamb vector in (14) as a convolution product. The third-order triadic tensor $S_{imn}(\mathbf{k}, \mathbf{p}, t)$ resulting from

$$\langle \hat{u}_i(\mathbf{k}) \hat{u}_m(\mathbf{p}) \hat{u}_n(\mathbf{q}) \rangle = S_{imn}(\mathbf{k}, \mathbf{p}) \delta^3(\mathbf{k} + \mathbf{p} + \mathbf{q}), \quad (15)$$

is eventually called into play in the integrand of $T(k)$, using the velocity Fourier modes only, via $\widehat{\boldsymbol{\omega}}(\mathbf{k}) = \imath \mathbf{k} \times \hat{\mathbf{u}}(\mathbf{k})$.

In pseudo-spectral DNS, for decaying isotropic turbulence, conventional initialization prescribes a narrow-band energy spectrum with an initial realization of the velocity field such that

$$u^{(1)} \sim \sqrt{\frac{E(k)}{4\pi k^2}} \cos \alpha_k e^{i\phi_k}, \quad u^{(2)} \sim \sqrt{\frac{E(k)}{4\pi k^2}} \sin \alpha_k e^{i\phi_k}, \quad (16)$$

in agreement with Craya and Rogallo. With simple choice of ‘translative’ phases ϕ_k and ‘rotative’ ones α_k , rediscussed below, the initial field is not skewed, as for a Gaussian distribution, and contains no structure. A realistic velocity field with tube-like vortex structures, however, can emerge via nonlinear evolution. This evolution is consistent with creation of inertial spectrum and spectral transfer for a skewed velocity field. This behaviour is obtained by directly solving the Lin equation (13), with $T(k, t)$ given by a robust ‘triadic’ closure, e.g. EDQNM-type [21]. In contrast with DNS, EDQNM has no limitation in term of Reynolds number, allowing recent results on finite-Reynolds number effects [27] and prediction of two-point and single-point skewness factors.

4.1 The best example: decaying homogeneous rotating turbulence

Phase coherence is essential in rapidly rotating turbulence, which reduces to *inertial wave turbulence* at low Rossby number. The effect of the Coriolis force is immediately accounted for by replacing $\boldsymbol{\omega}$ in (14) by the absolute vorticity $2\boldsymbol{\Omega} + \boldsymbol{\omega}$, in which $\boldsymbol{\Omega}$ is the angular velocity of the rotating frame. Because the basis of the helical modes is convenient for both the rotating (they are eigenmodes of the linear regime) and the non-rotating case (they diagonalize the Curl operator), the velocity field in Fourier space is expressed as

$$\hat{\mathbf{u}}(\mathbf{k}, t) = a_+(\mathbf{k}, t)e^{i\sigma_k t} \mathbf{N}(\mathbf{k}) + a_-(\mathbf{k}, t)e^{-i\sigma_k t} \mathbf{N}(-\mathbf{k}), \quad (17)$$

which displays the dispersion law of inertial waves

$$\sigma_k = 2\boldsymbol{\Omega} \cdot \mathbf{k} / k = 2\Omega k_{\parallel} / k, \quad \text{with } k = |\mathbf{k}|. \quad (18)$$

The linear regime of inertial waves is immediately recovered in replacing the *slow amplitudes* $a_s, s = \pm 1$ by constant terms, related to initial data at $t = 0$. The regime of weak nonlinearity for wave turbulence theory corresponds to a multiscale time separation between ‘rapid’ phases and ‘slow’ amplitudes, leading to $a_s(\mathbf{k}, t) \rightarrow a_s(\mathbf{k}, \epsilon t)$ with ϵ really a small parameter of the order of the Rossby number. On the other hand, if nothing is specified on the time dependency of a_s in (17, 18), arbitrary nonlinearity, and arbitrary Rossby number from 0 to infinite (no rotation) can be accommodated: One just define from (17) the most convenient set of variables, $a_s, s = \pm 1$ to study rotating turbulence.

Injecting (17) into (14) (with $\boldsymbol{\omega} \rightarrow \boldsymbol{\omega} + 2\boldsymbol{\Omega}$), an exact, purely nonlinear equation for a_s is derived as

$$\begin{aligned} & \left(\frac{\partial}{\partial t} + \nu k^2 \right) a_s(\mathbf{k}, t), s = \pm 1 \\ &= \sum_{s', s'' = \pm 1} \iiint_{k+p+q=0} \exp \left(2i\Omega t \left(s \frac{k_{\parallel}}{k} + s' \frac{p_{\parallel}}{p} + s'' \frac{q_{\parallel}}{q} \right) \right) \\ & \quad \times M_{ss's''}(\mathbf{k}, \mathbf{p}) a_{s'}^*(\mathbf{p}, t) a_{s''}^*(\mathbf{q}, t) d^3\mathbf{p}. \quad (19) \end{aligned}$$

Without rotation, $\Omega = 0$, the typical triadic phase term in the exponential is zero, and one recovers the alternative of basic Navier-Stokes equations using helical Fourier

modes, with the purely geometric ‘tradic’ factor $M_{ss's''}$ specified in [3], Waleffe (1990, 1993) and [24]. In the presence of rotation, the classical triadic interaction is weighted by the exponential term, often referred to as the resonance operator. It is clear that the linear regime (first line of eq. (19) is favoured by this phase term, which damps the nonlinearity in general by *tradic phase-mixing*. Significant nonlinearity can survive at small Ωt , but at very large Ωt , it is strongly reduced by phase-mixing and eventually, (small) nonlinearity is restricted to *resonant triads*, those for which the phase is almost zero in the exponential term.

Accordingly, eqs. (17) and (19) help understanding the limit of inertial wave turbulence (see [24] and the recent review of wave turbulence theory by Newell [20]) but here their use is more general, for any Rossby number, and at any time.

As for the basic dynamical equation, from (14) to (19), it is possible to derive a set of generalized Lin equation for the set (e, Z, \mathcal{H}) for arbitrary anisotropic, homogeneous rotating turbulence, as

$$\left(\frac{\partial}{\partial t} + 2\nu k^2 \right) e(\mathbf{k}, t) = T^{(e)}(\mathbf{k}, t), \quad (20)$$

and similar ones for the polarization term and the helicity spectrum [3, 4, 24]. We have now all the basic formalism to discuss the role of coherent phases in homogeneous rotating turbulence, as follows.

- Exact phase cancellation result from homogeneity looking at two-point second-order correlations. The absence of a typical Coriolis effect on the energy equation, in the linear regime, is not exactly due to the cancellation of a translative phase, as in (12), because the phase terms are twice (plus and minus) in (17) and they will affect a rotative phase instead. For instance, the linear regime is found, starting from Craya / Rogallo initialization (16) by changing α_k into $\alpha_k + \sigma_k t$. Anyway, phase cancellation is recovered looking at energy modes, proportional to $(1/2)\hat{\mathbf{u}}^* \cdot \hat{\mathbf{u}}$, also equal to $(1/2)(a_+^* a_+ + a_-^* a_-)$, whose $e(\mathbf{k}, t)$ is the ensemble average.
- Looking at the energy equation, a crucial Coriolis effect alters only the transfer term $T^{(e)}$ in (20). This effect is responsible for the alteration of the dynamics by rotation. It reduces the interscale energy transfer in average by triadic phase mixing, as the triadic phase term does in (19), resulting in a reduced dissipation rate. Because of the anisotropic structure of the phase term in (19), isotropy, if initially stated, is broken, so that a angle-dependent energy spectrum is dynamically created, but slaved to the spectral transfer term. Anisotropic shape of the energy spectrum, $e(k, k_{\parallel}/k)$ or $e(k_{\parallel}, k_{\perp})$, is consistent with axisymmetry without mirror symmetry, and compatible with an incomplete, or saturated, two-dimensionalization.

4.2 Quasi-static MHD : a toy model with linear forcing of two-dimensional structure

Two-dimensionalization by the sole effect of the Coriolis force remains an open problem in decaying homogeneous turbulence. On the other hand, complete two-dimensionalization can be achieved in quasi-static magnetohydrodynamics (QSMHD), and new insights are

found contrasting homogeneous rotating turbulence and homogeneous QSMHD.

The QSMHD case is sufficiently simple to be disconnected from the complex coupling of Navier-Stokes and induction equation for the magnetic field, present in MHD. At very small magnetic Prandtl number, e.g. in a liquid metal, under strong external magnetic field, Alfvén waves are inhibited, and the fluctuating magnetic field is enslaved to the velocity field in such a way that it can be removed from consideration.

The basic equation replacing (14), and replacing the one in a rotating frame is

$$\left(\frac{\partial}{\partial t} + \nu k^2\right) \hat{\mathbf{u}} + M_0^2 \left(\frac{k_{\parallel}}{k}\right)^2 \hat{\mathbf{u}} + \mathbf{P} \widehat{\boldsymbol{\omega}} \times \mathbf{u} = 0. \quad (21)$$

May I ask to the reader, at this stage, to forget all about MHD, such as the relationship of the parameter M_0 with the external magnetic field and the physical meaning of the related term with Ohmic dissipation? Equation (21) will be considered from now on as a basic Navier-Stokes equation with additional *linear term, leading to force two-dimensional structure*.

Starting from isotropic turbulence, in which all directions of the wavevector are populated with the same density of energy, the linear term will selectively damp velocity contributions with inclined wavevectors, so that it will tend to concentrate the spectral density of turbulent kinetic energy towards purely transverse wavevectors $k_{\parallel} \sim 0$. Of course, $k_{\parallel} = 0$ characterizes the two-dimensional manifold, or the contribution of modes in which the axial variability $\partial/\partial x_{\parallel}$ is removed by integration in physical space. The fully nonlinear equations are consistent with axisymmetry with mirror symmetry, so that all two-point second-order statistics derive from the previously mentioned energy spectrum $e(k_{\parallel}, k_{\perp}, t)$ and from its polarization term $Z(k_{\parallel}, k_{\perp}, t)$. Governing equations derive from (21) as

$$\left(\frac{\partial}{\partial t} + 2\nu k^2 + 2M_0^2 \left(\frac{k_{\parallel}}{k}\right)^2\right) e(\mathbf{k}, t) = T^{(e)}(\mathbf{k}, t), \quad (22)$$

and

$$\left(\frac{\partial}{\partial t} + 2\nu k^2 + 2M_0^2 \left(\frac{k_{\parallel}}{k}\right)^2\right) Z(\mathbf{k}, t) = T^{(Z)}(\mathbf{k}, t). \quad (23)$$

In this case, because of the mirror symmetry, the complex-valued polarization term Z is real, and e and Z are given by the sum and the difference, respectively, of the two eigenvalues, s_1^2 and s_2^2 of the spectral tensor $\hat{\mathbf{R}}$.

Pseudo-spectral DNS were used for solving eq. (21), with axisymmetry used for evaluating directly e and Z , by averaging on sectors in Fourier space around both k and its polar angle with respect to the axial direction, or $\cos\theta_k = k_{\perp}/k$: This gives simultaneously the ring-to-ring and shell-to-shell spectral distribution. The same information was obtained by directly solving eqs. (22, 23), in which $T^{(e)}$ and $T^{(z)}$ are closed by a dedicated, fully axisymmetric, EDQNM model. All statistical quantity, two-point as well as single-point, is derived from this information. Details of both approaches, with cross-fertilization, are given in [9].

4.2.1 Linear inviscid regime, as in Rapid Distortion Theory

This regime is well known since the pioneering study of Keith Moffatt (1967). Exponentially growing

anisotropic structure is found from the linear — with $T^{(e,Z)} = 0$ — solution of (22,23). All related second-order statistics are analytically derived, combining algebraic and Erf functions.

Three-dimensional isotropic initial data are given by $e = E(k, 0)/(4\pi k^2)$ and $Z = 0$. Z remains zero, whereas e concentrates towards its 2D limit, or

$$e(k_{\perp}, k_{\parallel}) = \frac{E(k, \infty)}{2\pi k} \delta(k_{\parallel}), Z = 0$$

Typical asymptotic anisotropic ratios are found for the Reynolds stress tensor and the vorticity tensor as

$$\frac{\langle u_{\parallel}^2 \rangle}{\langle u_{\perp}^2 \rangle} = 2, \quad \frac{\langle \omega_{\parallel}^2 \rangle}{\langle \omega_{\perp}^2 \rangle} = 2.$$

At least the first result is counter-intuitive. Initially, the Reynolds stress is spherical (3D isotropic), with $\frac{\langle u_{\parallel}^2 \rangle}{\langle u_{\perp}^2 \rangle} = 1$, and this ratio increases monotonically from 1 to 2. The explanation comes from the divergence-free constraint, which means orthogonality of the Fourier mode and the wavevector. Accordingly, a relative depletion of energy around axial wavevectors means a depletion of energy in the transverse direction. More physically, a 2D-3C (two-dimensional, three-component) state is reached, so that 2D — i.e. without axial variability — are favoured, but they consist of both vortical structures — with vertical vorticity and no vertical velocity — and ‘jettal’ structures, with only vertical, up-and-down, velocity (and horizontal vorticity). Accordingly, $e - Z$ at $k_{\parallel} = 0$ quantifies vortical 2D structures, whereas $e + Z$ at $k_{\parallel} = 0$ quantifies jettal 2D structures. Other statistical indicators are the integral length scales with axial separation, related to either axial velocity components $L_{\parallel}^{(||)}$ or to transverse velocity components $L_{\perp}^{(||)}$.

4.2.2 The nonlinear regime in a subsequent step

Some characteristics of the linear regime are qualitatively present, but the new element is the rise of polarization near the two-dimensional manifold, due to a very specific behaviour of $T^{(e)}$ and $T^{(z)}$ in (22, 23). In short, energy is concentrated near the 2D manifold, in a first phase where the linear effect is dominant. After this first phase, the linear term becomes less and less active, because it is zero at $k_{\parallel} = 0$, and the nonlinear dynamics is essential. This nonlinear dynamics is very close to a 2D-2C cascade for the transverse mode $e - Z$, cascade mediated by $T^{(e)} - T^{(z)}$, with a conventional inverse cascade for energy with reduced dissipation. On the other hand, the mode $e + Z$ for ‘jettal axial energy’ behaves as the spectrum of a passive scalar affected by 2D-2C turbulence: direct cascade and eventual dissipation. All our results from DNS and axisymmetric EDQNM are consistent for confirming this scenario, which is reflected on all derived statistical indicators: The RST ratio $\frac{\langle u_{\parallel}^2 \rangle}{\langle u_{\perp}^2 \rangle}$ begins to increase (linear) but eventually decreases after a maximum towards a zero value (nonlinear polarization with selected damping of ‘jettal’ 2D energy. Instead of the Reynolds stress tensor, the 2D energy components, $2\langle u_{\perp}^2 \rangle L_{\perp}^{(||)}$ and $\langle u_{\parallel}^2 \rangle L_{\parallel}^{(||)}$ are precise indicators of the polarization near the 2D manifold. Their difference is zero in the linear regime, so that its significant value means a large polarization induced by nonlinearity.

4.3 Rotating shear : SLT versus fully nonlinear dynamics

Setting aside other interactions, including coupled fields, such as passive and active (buoyancy) scalars in stratified turbulence, e.g. [11], active vector (magnetic field) in MHD, our last example deals with sheared turbulence in a rotating frame. Considering a mean flow with space-uniform velocity gradients A_{ij} , possibly seen in a rotating frame, our basic dynamical equation is now

$$\dot{\hat{\mathbf{u}}} + \nu k^2 \hat{\mathbf{u}} + \mathbf{M}\hat{\mathbf{u}} + \mathcal{PFT}[(2\boldsymbol{\Omega} + \boldsymbol{\omega}) \times \mathbf{u}] = 0, \quad (24)$$

in which the ‘overhat’ for Fourier transform previously used is replaced by $\mathcal{FT}[\dots]$, better for long arguments.

In agreement with spectral linear theory (SLT), the overdot denotes time-derivation following the characteristic lines given by the eikonal equation

$$\dot{k}_i + A_{ji}k_j = 0, \quad (25)$$

so that the wavevector is considered as time dependent. This is equivalent to follow the mean flow trajectories in physical space, given by

$$\dot{x}_i - \underbrace{A_{ij}x_j}_{\langle U_i \rangle} = 0. \quad (26)$$

As for the nonlinear term, use of a projection operator allows to account for the pressure term, which is enslaved to the solenoidal constraint. Accordingly the linear term generated by the effect of the mean flow, via \mathbf{A} is exact and reduces to a matrix \mathbf{M} which depends only on \mathbf{A} and on the direction of the wavevector (details in [24]).

The case of the rotating shear flow was recently revisited in [25], for a refined analysis of both linear terms, using SLT, and nonlinear terms using pseudo-spectral DNS in deformed coordinates (Rogallo 1981).

In contrast with purely rotating flows, the second-order statistics, generated by e, Z, \mathcal{H} , are not enslaved to nonlinear spectral transfer terms, but competition between purely linear terms and transfer terms is possible. As a single example, the equation for the 3D spectrum of energy is written as

$$\dot{e} + 2\nu k^2 e + \underbrace{\frac{\dot{k}}{k} e + \Re([\mathbf{N} \cdot \mathbf{A} \cdot \mathbf{N}] Z)}_{\text{exact linear part from } e \text{ and } Z} = T^{(e)} \quad (27)$$

Complete equations for the full set (e, Z, \mathcal{H}) are derived and discussed in [7] as well, but with almost exclusive emphasis on cubic correlations, and the triadic structure of $T^{e,Z,H}$ derived from eq. (15).

5 Conclusions and perspectives

Phase coherence is essential in the dynamical and structural approach to turbulence. If it is partially lost looking at two-point second-order velocity correlations, but an important contribution is restored at the level of three-point third-order correlations, which quantify the interscale energy cascade. Identified in a general POD decomposition, this issue remains relevant for quasi-homogeneous turbulence, working in Fourier space, especially for strongly anisotropic flow cases.

On the one hand, artificial phase-randomization is useful to create random realizations from prescribed second-order statistics. Incorporation of artificial random temporal frequencies, from basic KS, is not discussed here

(see [10] and its generalisation in [6]), so that our attention is restricted to ‘translative’ and ‘rotative’ phase terms, which give an optimal spatial randomization following Craya and Rogallo, in eq. (16). Of course, in the absence of artificial temporal frequencies, phase-randomization is a similar problem in KS and in DNS initialization. We should say few words on the more general way to generalize KS to fully anisotropic homogeneous flows. The most general information on second-order statistics is given by prescribing the complete $(e(\mathbf{k}), Z(\mathbf{k}), \mathcal{H}(\mathbf{k}))$ set with dependence on both orientation and modulus of the wave-vector. The best procedure is found by randomly choosing the whole wave-vector, with a probability directly connected to $e(\mathbf{k})$. Instead of incorporating the random phases into $u^{(1)}$ and $u^{(2)}$ components, as in eq. (16), they are introduced into the helical mode components, or a_+ and a_- at $t = 0$ in eq. (17), in a way which maintains the following exact relationship

$$e \propto \langle a_+^* a_+ + a_-^* a_- \rangle,$$

$$\mathcal{H} \propto \langle a_+^* a_+ - a_-^* a_- \rangle,$$

$$Z \propto 2\langle a_+^* a_- \rangle.$$

As a first promising application, one can reproduce realizations of helical anisotropic flows more realistic than, e.g., the forcing of a deterministic ABC helical flow by Mininni, Pouquet and coworkers. In addition, this gives an alternative to the dyadic spectral tensor obtained by DNS from a single realization of initial data (our analysis in sections 2 and 3.) As a second application, it is possible to use in KS, for various calculations including Lagrangian statistics from trajectories, a set (e, Z, \mathcal{H}) which results from fully nonlinear calculation, especially when their anisotropic structure is enslaved to the set $(T^{(e)}, T^{(z)}, T^{(H)})$, which include realistic phase coherence, via generalized Lin equations, such as in eqs. (13, 20, 22, 27) here.

Of course, the dynamical creation of phase coherence in third-order three-point correlations is outside the scope of KS; this is illustrated here by sophisticated triadic closures and full DNS. It is possible, however, to incorporate purely linear dynamics in KS, by retaining the purely linear inviscid part in eq. (24). This was done in rotating, stably-stratified, flows in [5]. To render a synthetic model of turbulence consistent with ‘Rapid Distortion Theory’ for each realization, in mimicking globally some nonlinear behaviour, is an important theme in this bulletin issue. In this context, some models were proposed by the Kassinos’s group (e.g. [13]), but one of the more advanced strategy is by Sharath Girimaji in the present theme issue. This strategy, combining both method and madness, as recently jokingly said by the author, consists of replacing the nonlinear term in eq. (24) by a ad-hoc Langevin stochastic term, and to add a stochastic contribution to the eikonal eq. (25).

The last point calls into play an essential role of KS, hardly discussed here: to provide synthetic trajectories $x_i = \tilde{x}_i(\mathbf{X}, t, t_0)$ from the synthetic velocity field in order to calculate Lagrangian statistics. From this viewpoint, the eikonal equation reflects in Fourier space the mean flow trajectory equation (26), which corresponds to $D\tilde{x}_i/Dt = \langle U_i \rangle$, whereas KS can give access to ‘turbulent’ trajectories given by

$$D\tilde{x}_i/Dt = \langle U_i \rangle(\mathbf{x}) + u_i(\mathbf{x}, t).$$

A possible interpretation of the stochastic part of the Eikonal equation follows, but this is possibly redundant with the use of KS to derive the turbulent trajectories.

Acknowledgments

This essay reflects collective work and discussions with Julian F. Scott and Fabien S. Godefert, partly supported by the French National Research Agency (ANR) under contract number 08-BLAN-0076 ‘ANISO’.

References

- [1] N. AUBRY, M. - P. CHAUVE, AND R. GUYONNET, 1994, ‘Transition to turbulence in a rotating flat disc’, *Phys. Fluid* **6**, (8), 2800–2814.
- [2] F. BELLET, F. S. GODEFERD, J. F. SCOTT AND C. CAMBON, 2006, ‘Wave turbulence in rapidly rotating flows’, *J. Fluid Mech.* **562**, 83–121.
- [3] C. CAMBON AND L. JACQUIN, 1989, ‘Spectral approach to non-isotropic turbulence subjected to rotation’, *J. Fluid Mech.* **202**, 295–317.
- [4] C. CAMBON, N. N. MANSOUR, AND F. S. GODEFERD, 1997, ‘Energy transfer in rotating turbulence’, *J. Fluid Mech.* **337**, 303–332.
- [5] C. CAMBON, F. S. GODEFERD, F. NICOLLEAU, AND J. C. VASSILICOS, 2004, ‘Turbulent diffusion in rapidly rotating flows with and without stable stratification’, *J. Fluid Mech.* **499**, 231–255.
- [6] C. CAMBON, F. S. GODEFERD, AND B. FAVIER, 2012, *Incorporating linear dynamics and strong anisotropy in KS. Application to diffusion in rotating, stratified, MHD turbulence, and to aeroacoustics*, in ‘New approaches in modeling multiphase flows and dispersion in turbulence, fractal methods and synthetic turbulence’, *ERCRAFT Series 18*, ISBN 978-94-007-2505-8.
- [7] C. CAMBON, L. DANAILA, F. S. GODEFERD AND J. F. SCOTT, ‘Third-order correlations and dynamics of strongly anisotropic turbulent flows’ *J. Fluid Mech.* to be submitted.
- [8] S. CHANDRASEKHAR, 1981, *Hydrodynamic and hydrodynamic stability*, Clarendon Press.
- [9] B. FAVIER, F. S. GODEFERD, C. CAMBON, A. DELACHE & W. J. T. BOS, 2011, ‘Quasi-static magnetohydrodynamic turbulence at high Reynolds number’ *J. Fluid Mech.* **681**, 434–461.
- [10] J.C.H. FUNG, J.C.R. HUNT, N.A. MALIK AND R.J. PERKINS, 1992, ‘Kinematic simulation of homogeneous turbulence by unsteady random Fourier modes’, *J. Fluid Mech.* **236**
- [11] F. S. GODEFERD AND C. CAMBON, 1994, ‘Detailed investigation of energy transfers in homogeneous stratified turbulence’, *Phys. Fluids* **6**, 2084–2100.
- [12] Y. KANEDA AND T. ISHIHARA, 2003, ‘Energy dissipation rate and energy spectrum in high resolution direct numerical simulations of turbulence in a periodic box’, *Phys. Fluids* **15**, L21
- [13] S. C. KASSINOS & H. RADHAKRISHNAN, 2012, ‘Advances in structure-based modelling’, *ERCRAFT bulletin* 88, SIG 35 theme issue.
- [14] R.H. KRAICHNAN, 1964, ‘Diffusion by a random velocity field’, *Phys. Fluids* **13**
- [15] C. LAMRIBEN, P.P. CORTET, F. MOISY, 2011, ‘Direct measurements of anisotropic energy transfers in a rotating turbulence experiment’, *Phys. Rev. Lett.* **107** (2), 024503.
- [16] L. LIECHTENSTEIN, F. S. GODEFERD AND C. CAMBON, 2005, ‘Nonlinear formation of structures in rotating stratified turbulence’, *J. Turbulence* **6**, 1–18
- [17] J. L. LUMLEY, 1967, ‘The structure of inhomogeneous turbulent flows’, in *Atmospheric Turbulence and Radio Wave Propagation*, edited by A. M. Yaglom and V. I. Tatarski (Nauka, Moscow, 1967).
- [18] DAVID MC COMB, 2011, ‘Kolmogorov’s theory: K41 or K62 ?’, *ERCRAFT bulletin* 88, SIG 35 theme issue, 11–18.
- [19] Y. MORINISHI, K. NAKABAYASHI, AND S. Q. REN, 2001, ‘Dynamics of anisotropy on decaying homogeneous turbulence subjected to system rotation’, *Phys. Fluids***13** (10), 2012.
- [20] A. C. NEWELL AND B. RUMPF, 2011, ‘Wave Turbulence’, *Annu. Rev. Fluid Mech.* **43**, 59–78.
- [21] S. A. ORSZAG, 1970, ‘Analytical theories of turbulence’, *J. Fluid Mech.* **41**, 363–386.
- [22] S.A. ORSZAG AND G.S. PATTERSON, 1972, ‘Numerical Simulation of Three-Dimensional Homogeneous Isotropic Turbulence’, *Physical Review Letters* **28**
- [23] R. S. ROGALLO, 1981, ‘Numerical experiments in homogeneous turbulence’, NASA Tech. Mem. 81315.
- [24] P. SAGAUT & C. CAMBON, 2008, *Homogeneous Turbulence Dynamics*, , Camb. U. Press, New York.
- [25] A. SALHI, F. JACOBITZ, K. SCHNEIDER, AND C. CAMBON, ‘Anisotropic and multiscale properties in rotating sheared turbulence’, *J. Fluid Mech.*, to be submitted.
- [26] P. J. STAPLEHURST, P. A. DAVIDSON & S. B. DALZIEL, 2008, ‘Structure formation in homogeneous, freely-decaying, rotating turbulence’, *J. Fluid Mech.* **598**, 81–103.
- [27] J. TCHOUFAG, P. SAGAUT & C. CAMBON, 2012, ‘Spectral approach to finite Reynolds number effects on Kolmogorov 4/5 law in isotropic turbulence’, *Phys. Fluids* **24**, 015107.

MANUFACTURED TURBULENCE WITH LANGEVIN EQUATIONS

A. A. Mishra¹ and S. Girimaji¹

¹*Aerospace Engineering Department, Texas A&M University, College Station, Texas, USA*

Abstract

By definition, *Manufactured turbulence*(MT) is purported to mimic physical turbulence rather than model it. The MT equations are constrained to be simple to solve and provide an inexpensive surrogate to Navier-Stokes based Direct Numerical Simulations (DNS) for use in engineering applications or theoretical analyses. In this article, we investigate one approach in which the linear inviscid aspects of MT are derived from a linear approximation of the Navier-Stokes equations while the non-linear and viscous physics are approximated via stochastic modeling. The ensuing Langevin MT equations are used to compute planar, quadratic turbulent flows. While much work needs to be done, the preliminary results appear promising.

1 Introduction

Turbulence is an enigmatic mix of *method* (large scale coherent structures) and *madness* (chaotic, small scale motions). While the coherent structures are evidently flow-dependent, the small-scale chaotic motions exhibit a rather surprising level of independence from the large scales (Kolmogorov hypotheses). Arguably, it is the large scale structures that are dynamically important and the role of the small scale motions is merely to provide a means for dissipating the cascaded energy. It is rather interesting that the dynamically decisive large scales are easier to compute and more difficult to model than the small scales which are more onerous to compute but play a more straightforward role. Any attempt at capturing turbulence physics must pay heed to these crucial matters.

Our charge in this work is to develop simple-to-solve equations that mimic physical turbulence, rather than model it. Here we reserve the term *model* to indicate those attempts to develop closure equations for the moments of the turbulence field. To *mimic* is to yield spatio-temporal realizations of velocity and pressure fields and entire probability distribution functions. We call such a surrogate flow field, *Manufactured Turbulence*(MT). The MT flow-field is intended for use in engineering applications and theoretical analyses as an inexpensive substitute to the Direct Numerical Simulations (DNS) of the Navier-Stokes equations.

In the absence of an analytical theory of turbulence, the computational recourse to turbulence is extensively utilized in industrial and academic applications. Of these, computationally intensive methods like Direct Numerical Simulation and Large Eddy Simulation are limited in their application due to their excessive computational demands. On the other hand, modeling intensive approaches, such as one or two equation models, are encumbered due to their lack of fidelity in many varieties of flows. In this vein, synthetic or manufactured turbulence is a contrivance to generate signals that mimic

real turbulent flow fields. Kinematic Simulation (KS) is predominantly used to this end.

An alternative that is popular in the turbulent combustion community is based on the Langevin equation in a Lagrangian framework. Such *Probability Density Function methods* have been extensively applied and have become established in turbulence research ([1, 2]). This work is based, in essence, upon extensions of the simplistic analogy between the motion of fluid elements in a turbulent flow and the motion of gas molecules. Chung ([3]) used a similar analogy with the motion of fluid elements and Brownian motion, to develop a simplified statistical model for turbulence. Kuznetsov and Frost ([4]) applied a consonant similitude to use a Langevin equation for this purpose. This was extended by Pope and co workers ([5]). In an analogy with the Langevin equation governing the velocity of a particle undergoing Brownian motion, a linear Markov model for fluid particle velocity was developed in [5]. The effects of fluctuating pressure and viscosity are modeled via deterministic drift and diffusion terms. The diffusion term represents a random walk in velocity space. Haworth and Pope ([5]) used the Navier Stokes equation as the starting point for the model formulation, thus adding physical significance to the terms of the Langevin equation and the concomitant coefficients therein. Furthermore, to account for the rapid component of pressure (and specifically, its dependence on mean gradients) an anisotropic drift term was added to the generic Langevin equation.

In this article, we apply a general set of Langevin equations to generate Manufactured Turbulence. It is accepted that linear physics provides a qualitative representation for many features of turbulent flows. However, the exactitude of this linear representation is contingent upon many factors. It is found that the quantitative preponderance of linear theory is highly dependent on the regime of flow. This is explained with respect to the nature of the instabilities manifested in these flows.

2 Mathematical formulation and rationale

The essential components of a turbulent flow field consist of:

1. Linear effects, consisting of inertial physics, embodied in production and *rapid* pressure action.
2. Non-linear effects, that include the *slow* pressure action.
3. Viscous effects.

Of these, the linear effects are the drivers of turbulence and engender the variations in different flows. Thus, it is essential to ensure that these are represented as precisely as possible. The non-linear effects are universal and can be modeled statistically.

Based on physics, pressure action can be decomposed into two components, viz. rapid and slow.

$$\frac{1}{\rho}\nabla^2 p' = -2\frac{\partial U_i}{x_j}\frac{\partial u_j}{x_i} - \frac{\partial^2}{\partial x_i\partial x_j}(u_i u_j - \bar{u}_i \bar{u}_j), \quad (1)$$

where the first and second terms on the right, represent the contributions of rapid and slow pressure, respectively. The adjectives rapid and slow refer to the components of pressure arising, respectively, from the linear and non-linear parts of the source term in the Poisson equation for pressure. The slow component acts to conserve the incompressibility of the velocity field generated by the nonlinear interactions among velocity fluctuations. Similarly, it is the function of rapid pressure to impose the divergence free condition on the fluctuating velocity field produced by linear interactions between the mean and fluctuating fields.

Based on established theory, surrogates for the linear and the non-linear effects of pressure can be developed separately. Thence, these can be appended to give a complete, general surrogate for the pressure effects. In contrast to the slow pressure and its universal nature, the action of the rapid pressure effects are a strong function of the mean velocity field and initial flow conditions. In spite of the apparent simplification afforded by linearity, the action of rapid pressure is not straightforward. Depending on the nature of the mean velocity field and initial conditions of the flow field, the effect of the rapid pressure component can be diametric. Furthermore, this action can alter the fundamental nature of the flow. This is best exhibited in the regime of elliptic flows, where it is established that the rapid pressure effects initiate and sustain the elliptic flow instability ([6]). Most engineering models do not capture the nature of this action and predict a decay of turbulence, contrary to theory and DNS results ([7]). Thus, the linear pressure effects must be represented as accurately as possible. The import of fidelity to linear dynamics, even in KS has been accepted and attempts have been made to coalesce the knowledge developed via RDT in KS. Nicolleau and Vassilicos ([8]) utilized temporal evolution predicted by RDT with the KS velocity field formalism. This was applied and compared contra DNS in [9]. Kaneda and Ishida ([10]) used a similar approach to study the diffusion of a passive scalar. Subsequently, this approach of amalgamating RDT with KS has been extended, for instance in [11]. Under the aegis of RDT, the velocity field can be expressed as a summation of advected Fourier modes. In this formulation, the rapid pressure effects can be represented exactly. To this end, the rapid pressure component of the Langevin set is formulated in spectral space. In spectral space, this formulation can account for the initial conditions accurately and is not hampered by an incomplete basis. The germane equations in this regard are:

$$\frac{d\kappa_l}{dt} = -\kappa_j \frac{\partial U_j}{\partial x_l}, \quad (2)$$

$$\frac{du_j}{dt} = -u_k \frac{\partial U_l}{\partial x_k} (\delta_{jl} - 2\frac{\kappa_j \kappa_l}{\kappa^2}), \quad (3)$$

and the incompressibility constraint is given by $\mathbf{u} \cdot \boldsymbol{\kappa} = 0$. Herein, \vec{u} and $\vec{\kappa}$, or the Fourier velocity amplitude and wave-vector respectively, are considered random variables and are simulated via Monte Carlo techniques.

With regard to the slow component of pressure, it is established that this has a return to isotropy effect, wherein, the anisotropy of the Reynolds stress tensor is reduced. This, in essence, is a redistribution of the turbulent kinetic energy from any given distribution to an

uniform, isotropic distribution. Thus, the slow pressure effects are represented via a stochastic diffusion form. Explicitly,

$$A_{ij}(u, e)dW_j, \quad (4)$$

where A_{ij} is the diffusion tensor and dW is an isotropic Wiener process. Consequently, the representation reduces to

$$de_i = g_i(u, e) + A_{ij}(u, e)dW_j + B_{ij}(u, e)dW'_j. \quad (5)$$

$$du_i = h_i(u, e) + H_{ij}(u, e)dW_j + G_{ij}(u, e)dW'_j. \quad (6)$$

Constraints are applied to the system to ensure physical fidelity. These are:

1. Ensure that \vec{e} remains a unit vector.
2. Maintain orthogonality of \vec{u} and \vec{e} .
3. The PDF of the velocity approaches an isotropic, joint-normal distribution.
4. The evolution of the turbulent kinetic energy is exact in the limit of decaying turbulence.

These ensure realizability of the Reynolds stresses. For details of the derivation, the reader is referred to [12]. The velocity evolution equation is represented as a Langevin equation with an anisotropic drift term. Such surrogates can be thought of as bridging methods between one-point closures and multi-point/spectral closures.

The dissipation model is appended to the formulation to complete the basis. This is of the established form:

$$\frac{d\epsilon}{dt} = \frac{\epsilon^2}{k}(C_1 \frac{P}{\epsilon} - C_2). \quad (7)$$

Consequently, the entire set of equations reduces to:

$$\begin{aligned} du_i = & -u_k \frac{\partial U_l}{\partial x_k} (\delta_{il} - 2e_i e_l) dt - \frac{1}{2} \frac{\epsilon}{k} (1 + \frac{3}{2} a_u) u_i dt \\ & + \frac{\gamma \epsilon}{k} (b_{ij} - II_b \delta_{ij}) u_j dt - \sqrt{a_u \epsilon} dW_i. \\ de_i = & -\frac{\partial U_m}{\partial x_l} e_m (\delta_{il} - e_i e_l) dt - \frac{1}{2} \frac{\epsilon}{k} (a_e + a_u \frac{k}{u_s u_s}) e_i dt \\ & - \frac{\gamma \epsilon}{k} (\delta_{ij} - 2e_i e_j) b_{jl} e_l - \sqrt{a_u \epsilon} \frac{u_i e_l}{u_s u_s} dW_l + \\ & \sqrt{\frac{a_e \epsilon}{k}} (\delta_{il} - e_i e_l - \frac{u_i u_l}{u_s u_s}) dW'_l. \end{aligned} \quad (8)$$

Figure 1 exhibits the representation's performance, wherein the predictions are compared against DNS results ([12]).

3 Linear physics in planar, quadratic flows

Linear theories such as RDT ignore the interaction of turbulence with itself. This is justified via assumptions regarding the times scales (of mean and fluctuating distortions), a weak turbulence assumption, etc. However, the linear instabilities manifested in RDT obviate these assumptions. With increase in the turbulent kinetic energy, the non-linear effects become more important and thus, linear theory cannot suffice, beyond a very limited time period. In this duration, the linear effects structure

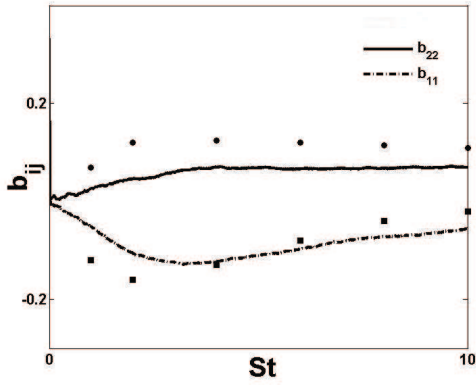


Figure 1: Comparison of the predictions against DNS results

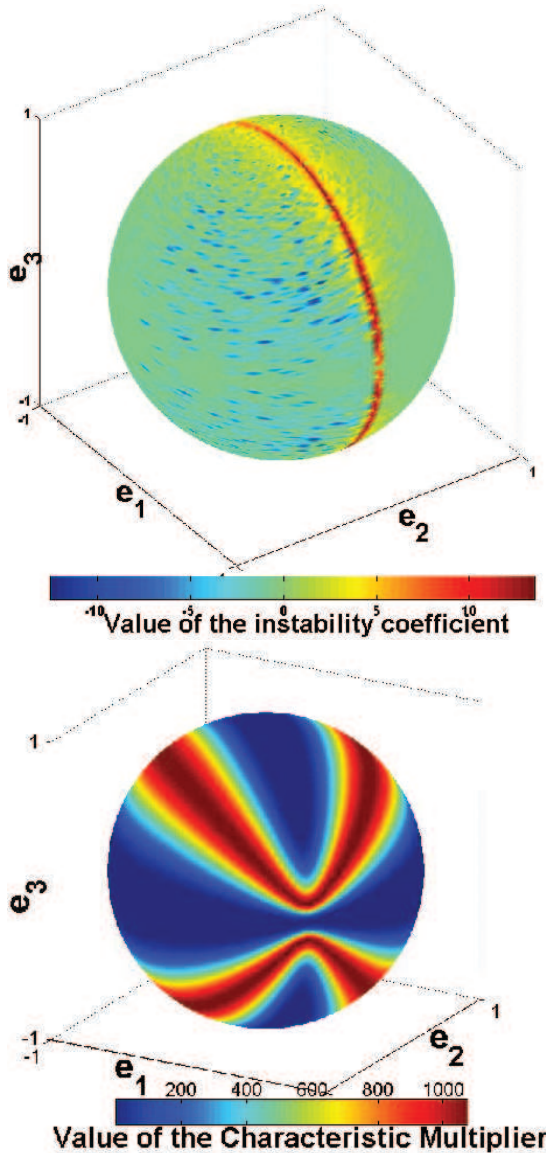


Figure 2: The unstable modes exhibited, with respect to their alignment in (a) a representative hyperbolic flow, (b) in an elliptic flow

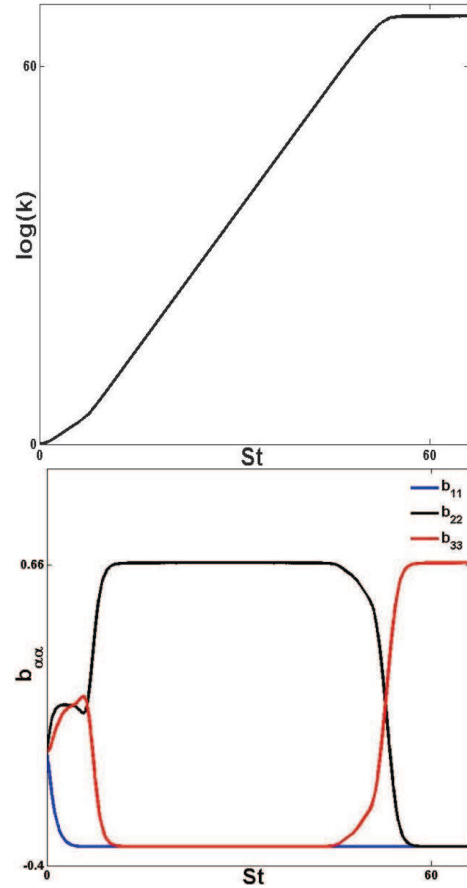


Figure 3: The evolution of (a) the turbulent kinetic energy, (b) Reynolds stress anisotropies in a plane strain flow, under the aegis of the Rapid Distortion Limit

the flow field. Thence, non-linear effects modify the evolution of turbulence. This structuring effect of the linear physics is most evident in the instabilities manifested therein, where certain modes are engendered to grow preferentially. Figure 2 exhibits the unstable modes, in a representative hyperbolic and an elliptic flow, with respect to their alignment. The figure is motivated by a congruous illustration in [13]. As can be observed, the unstable modes in an elliptic flow form a continuous band. However, the unstable modes in a hyperbolic flow lie on a set of zero measure. In the hyperbolic case, all other modes are either stable or can undergo some transient growth. Furthermore, this state of alignment for the unstable modes is in itself unstable and these can be forced off this alignment by any perturbations. This is evident in Figure 3, wherein the hyperbolic flow instability is arrested by the pressure effects. This occurs via the transfer of turbulent kinetic energy out of the plane of applied shear via the pressure strain correlation. The interested reader is referred to [14], wherein the linear aspects of this problem are analyzed in detail. It is observed that this shift is robust and manifests itself for all open streamline flows, as exhibited in Figure 4. In this vein, it is pertinent to question the exactitude of the hyperbolic instability, caused by these modes, in regimes where the non-linear effects become more and more significant. Furthermore, this is contrasted against similar comparisons in other regimes of planar, quadratic flows.

The structuring effects of linear physics are most predominant in purely sheared flows. This is evident the large streamwise length scales observed in boundary lay-

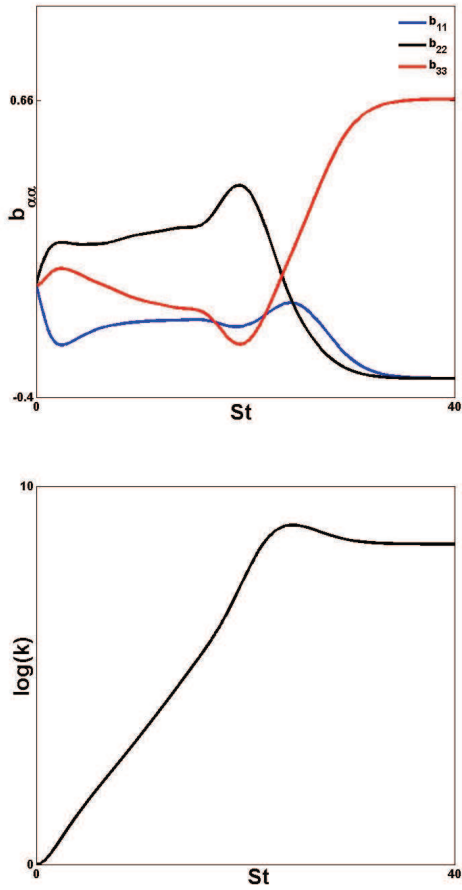


Figure 4: The evolution of (a) the turbulent kinetic energy, (b) Reynolds stress anisotropies in a representative open streamline flow, under the aegis of the Rapid Distortion Limit

ers. Furthermore, it has been observed that the evolution of flow statistics is similar in DNS studies, as compared to RDT simulations ([15]). This is exhibited in Figure 5, where the results of the Langevin equation representation are compared to those from RDT based simulations.

Figure 6. compares the evolution of flow statistics for elliptic flows in the presence and absence of non-linear effects. As can be observed, the results are very similar in the absence of non-linear effects or when they are of a small finite value. This is due to the finite measure of the set of unstable modes. However, this scenario does not persist for all elliptic flows. For instance, in purely rotating flows, it is known that linear theory is inconsistent with DNS results ([15]).

Figure 7. compares the evolution of flow statistics in a representative hyperbolic flow as the non-linear effects become more important. It is observed that due to the non-linear effects, the switch in the anisotropy evolution occurs progressively earlier. This is due to the perturbation of the wave-vector due to the non-linear effects, which force modes off the unstable set.

4 Conclusions

In this article, we exhibit the application of *Manufactured Turbulence* (MT) to study the linear physics in a planar quadratic flow. The MT equations are exact in the Rapid Distortion Limit and use a Langevin equa-

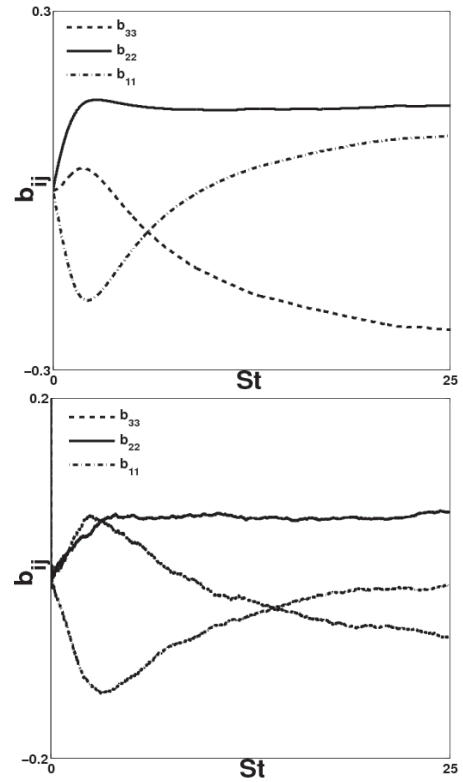


Figure 5: Comparison of the evolution of Reynolds stress anisotropies in a purely sheared flow (a) RDT results, (b) Langevin representation with $\frac{Sk}{\epsilon} = 25$

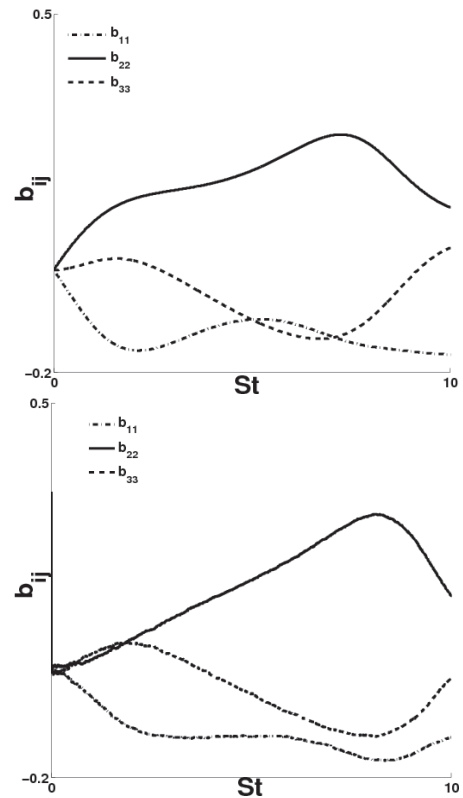


Figure 6: Comparison of the evolution of Reynolds stress anisotropies in a representative elliptic flow (a) RDT results, (b) Langevin representation with $\frac{Sk}{\epsilon} = 50$

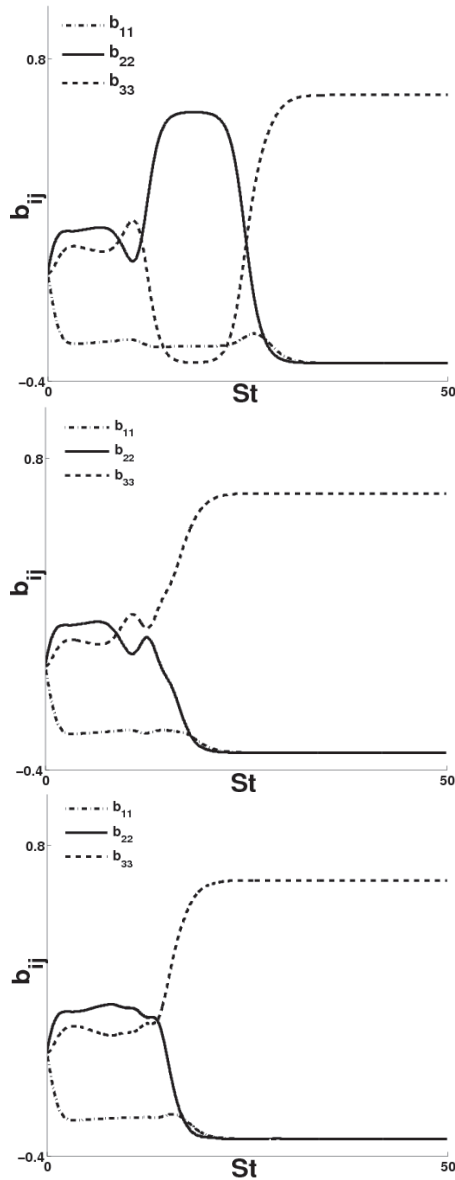


Figure 7: Comparison of the evolution of Reynolds stress anisotropies in a representative hyperbolic flow (a) RDT results, (b) Langevin representation with $\frac{Sk}{\epsilon} = 80$, (c) Langevin representation with $\frac{Sk}{\epsilon} = 60$

tion to simulate the return to isotropy effect of the slow pressure term. Thus, chaotic advection is incorporated using a white noise term. The mathematical formulation of such representations is introduced and the underlying rationale explained.

Thence, this surrogate is applied to study the import of linear physics for planar, quadratic flows. It is found that for purely sheared flows, linear theory provides a very good representation of the evolution of flow statistics, even in the presence of non-linear effects. For general elliptic flows, effects of linear physics are predominant even in the presence of moderate non-linearity. This is due to the banded nature of the instability, where unstable modes lie on a continuous band of finite measure. Thus, perturbations due to the non-linear effects have very little influence on the instability. However, for hyperbolic flows, the linearly unstable modes lie on a set of very small measure. Thus perturbations to these modal alignments may have significant effects on the state of instability and consequently, the evolution of flow statistics. However, only the transient time to reach the asymptotic stage is affected. But the final asymptotic

behavior is still as dictated by linear phenomenon. It is observed that linear effects dominate the overall flow behavior, although non-linear aspects can have an important effect on transients.

References

- [1] S. B. Pope, "Pdf methods for turbulent reactive flows," *Prog. Energy Com. Sci.*, vol. 11, 1985.
- [2] S. B. Pope and Y. L. Chen, "The velocity-dissipation probability density function model for turbulent flows," *Phys. Fluids A*, vol. 2, 1990.
- [3] P. Chung, "A simplified statistical model of turbulent, chemically reacting shear flows," *AIAA journal*, vol. 7, 1969.
- [4] V. Kuznetsov and V. Frost, "Probability distribution of the concentration and intermittency in turbulent jets," *Akademiia Nauk SSSR, Izvestiia, Mekhanika Zhidkosti i Gaza*, 1973.
- [5] D. Haworth and S. B. Pope, "A generalized Langevin model for turbulent flows," *Phys Fluids*, vol. 29, 1986.
- [6] C. Cambon, J. P. Benoit, L. Shao, and L. Jacquin, "Stability analysis and large-eddy simulation of rotating turbulence with organized eddies," *Journal of Fluid Mechanics*, vol. 278, pp. 175–200, 1994.
- [7] G. A. Blaisdell and K. Shariff, "Homogeneous turbulence subjected to mean flow with elliptic streamlines," 1995. Studying Turbulence Using Numerical Simulation Databases. 5: Proceedings of the 1994 Summer Program.
- [8] F. Nicolleau and J. C. Vassilicos, "Turbulent diffusion in stably stratified non-decaying turbulence," *Journal of Fluid Mechanics*, vol. 410, pp. 123–146, 2000.
- [9] C. Cambon, F. S. Godefred, F. Nicolleau, and J. C. Vassilicos, "Turbulent diffusion in rapidly rotating flows with and without stable stratification," *Journal of Fluid Mechanics*, vol. 499, pp. 231–255, 2004.
- [10] Y. Kaneda and T. Ishida, "Suppression of vertical diffusion in strongly stratified turbulence," *Journal of Fluid Mechanics*, vol. 402, pp. 311–327, 2000.
- [11] G. Nicolleau, F. Yu and J. C. Vassilicos, "Kinematic simulation for stably stratified and rotating turbulence," *Fluid Dynamics Research*, vol. 40, pp. 68–93, 2008.
- [12] P. R. V. Sooten and S. B. Pope, "PDF modeling for inhomogeneous turbulence with exact representation of rapid distortions," *Phy Fluids*, vol. 9, 1997.
- [13] C. Cambon, J. Benoit, L. Shao, and L. Jacquin, "Stability analysis and large-eddy simulation of rotating turbulence with organized eddies," *Journal of Fluid Mechanics*, vol. 278, pp. 175–200, 1994.
- [14] A. A. Mishra and S. S. Girimaji, "Pressure-strain correlation modeling: Towards achieving consistency with rapid distortion theory," *Flow, Turbulence and Combustion*, vol. 85, pp. 593–619, 2010.
- [15] C. Cambon, "Linear and non-linear models of anisotropic turbulence," *Annual Rev. Fluid Mech.*, vol. 31, 1999.

SUBGRID-SCALE STATISTICS IN SYNTHETIC HELICAL TURBULENT FIELDS GENERATED BY THE MULTI-SCALE TURNOVER LAGRANGIAN MAP

Y. Li¹ and C. Rosales²

¹*School of Mathematics and Statistics, University of Sheffield, Sheffield, UK S3 7RH*

²*Department of Mechanical Engineering, Universidad Tecnica Federico Santa Maria, Chile*

Abstract

The multi-scale turnover Lagrangian map (MTLM) has recently been proposed as a way to generate synthetic turbulent fields. Several studies show that the synthetic fields reproduce remarkably well many of the small scale statistics, including anomalous scaling for the velocity increments and the coarse-grained turbulent energy dissipation fields. The results inspire further investigation of the method. In this paper, we look into the statistics related to the subgrid-scale stress in the filtered velocity fields generated by the MTLM, and generalize the method so that both energy and helicity spectra can be enforced simultaneously. We observe that the MTLM fields reproduce the plateaus in the scale dependence of the mean subgrid-scale dissipations in the inertial ranges, implying energy and helicity cascades are generated by the MTLM procedure, although the values are somewhat underestimated. The geometrical statistics also show good agreement. Some discrepancies are observed, which can be traced back to the known fact that the MTLM fields are lacking concentrated vortex tubes.

1 Introduction

Synthetic turbulence has been devised as a simplified model to understand aspects of turbulent flow fields. Kinematic simulations have been used widely in the study of particle dispersion (see, e.g. [1, 2]). Other synthetic fields have also been proposed in the inquiry of material deformation and small scale intermittency [3, 4]. On the practical side, realistic synthetic fields have been an important component for the successful simulations of certain turbulent flows, where the initial and/or upstream conditions have significant effects on the later evolution of the flow. The multi-scale turnover Lagrangian map (MTLM) is proposed in [5] where the velocity field is generated by recursive use of a simple Lagrangian map, while maintaining the prescribed energy spectrum. A related method, the minimal multi-scale Lagrangian map (MMLM) is also proposed by the same authors [6]. The latter differs from the former in the way the mapping is iterated. The results show that the two methods are able to generate synthetic fields that reproduce many statistics of the small scales of hydrodynamic turbulence, such as the statistics of the vorticity and the strain rate tensor, including geometrical statistics such as the geometry of the strain rate tensor and its alignment with the vorticity. Besides, the velocity increments and the coarse-grained energy dissipation in the MTLM fields also possess anomalous scaling, with scaling exponents in close agreement with the realistic values [5]. The synthetic velocity fields generated using

these methods have been used as the initial conditions for large eddy simulations (LES). It is shown that considerable time can be saved as lengthy ‘pre-simulation’ is no longer needed, and that the evolution of decaying turbulence is more realistically reproduced [6].

This paper is motivated by the interesting properties of the MTLM and MMLM fields. The purpose is two-fold. First of all, we intend further looking into the inter-scale interaction in the synthetic fields in this paper. On the other hand, we generalize the methods to consider stationary helical isotropic turbulence, where a constant helicity spectrum is imposed. We will use filtering to separate the velocity field into resolved scales and sub-grid scales (SGSs), and examine the inter-scale interactions through the statistics of the SGS stress, including the SGS energy dissipation and SGS helicity dissipation. We aim at, first, checking if the methods generate realistic helical statistics, and second, gaining understanding to the inter-scale interaction in Navier-Stokes (NS) turbulence through the comparison with the synthetic fields.

2 Helicity and helical turbulence

Helicity $h = \mathbf{u} \cdot \boldsymbol{\omega}$, where \mathbf{u} is the velocity and $\boldsymbol{\omega} = \nabla \times \mathbf{u}$ is the vorticity, is a quadratic invariant of the inviscid NS equation. It has been observed in DNS that a Kolmogorov-type helicity spectrum establishes in isotropic helical turbulence with constant helicity input. Let $H(k)$ be the helicity spectrum at wavenumber k , such that $\langle h \rangle = \int_0^\infty H(k) dk$. In the inertial range, it is proposed in [7] that $H(k)$ should be

$$H(k) = c_H \eta \epsilon^{-1/3} k^{-5/3}, \quad (1)$$

where c_H is a constant, and found to be approximately 1.0 by DNS [8]. η is the helicity dissipation rate, and ϵ the energy dissipation rate.

The nonlinear inter-scale interaction in helical turbulence can be studied using the filtering method. Let $G_\Delta(\mathbf{x})$ be a filter kernel with Δ being the filter length, the filtered velocity $\tilde{\mathbf{u}}(\mathbf{x}, t)$ is the convolution between $G_\Delta(\mathbf{x})$ and the velocity field $\mathbf{u}(\mathbf{x}, t)$, i.e., $\tilde{\mathbf{u}}(\mathbf{x}, t) \equiv [G_\Delta * \mathbf{u}](\mathbf{x}, t)$. The filtered velocity \tilde{u}_i satisfies the filtered Navier-Stokes (NS) equations:

$$D_t \tilde{u}_i = -\partial_i \tilde{p} + \partial_j (-\tau_{ij}) + \nu \nabla^2 \tilde{u}_i + \tilde{f}_i, \quad (2)$$

where $\tau_{ij} = \widetilde{u_i u_j} - \tilde{u}_i \tilde{u}_j$ is the subgrid-scale (SGS) stress and \tilde{f}_i is the forcing term. The SGS stress represents the effects of the SGS scales on the resolved scales. The parametrization of τ_{ij} is crucial in simulation techniques such as large eddy simulations.

The effects of τ_{ij} are multi-facet, but one important aspect is the energy flux through the filter scale generated by τ_{ij} , which is defined as

$$\Pi_E = -\tau_{ij}\tilde{S}_{ij}, \quad (3)$$

where $\tilde{S}_{ij} = (\partial_i\tilde{u}_j + \partial_j\tilde{u}_i)/2$ is the filtered strain rate tensor. Π_E is a sink term in the equation for the kinetic energy of the resolved scales $\tilde{u}_i\tilde{u}_i/2$, and is commonly called the SGS energy dissipation.

For helical turbulence, the helicity flux across the filter scale characterizes another aspects of the inter-scale interaction. From the filtered NS equation, one can derive the balance equation for the resolved helicity $h_\Delta = \tilde{\mathbf{u}} \cdot \tilde{\boldsymbol{\omega}}$, where $\tilde{\boldsymbol{\omega}}$ is the filtered vorticity. An crucial contribution to the balance of h_Δ is the SGS helicity dissipation

$$\Pi_H = -2\tau_{ij}\tilde{R}_{ij}, \quad (4)$$

where $\tilde{R}_{ij} = (\partial_i\tilde{\omega}_j + \partial_j\tilde{\omega}_i)/2$. The SGS helicity dissipation represents the helicity flux crossing the filter scale.

3 The Multi-scale Turnover Lagrangian Map

The MTLM is motivated in part by the simple dynamical system found in [9] (see also [10]). The dynamical system describes the velocity and scalar increments over a fixed distance on a material line element. The model highlights the effects of the nonlinear interactions of the increments, whereas only part of the effects of the pressure is accounted for. Numerical solutions show that a range of observations regarding the non-Gaussian behaviours of the increments are reproduced qualitatively by the model. Noting that the nonlinear interaction between the increments essentially arises from the ballistic relative motions between the particles, the MTLM model is developed. We briefly recap the MTLM below, and shows how to maintain the helicity spectrum during the recursive use of the mapping.

The main building block of the MTLM method is the Riemann equation

$$\partial_t \mathbf{u} + (\mathbf{u} \cdot \nabla) \mathbf{u} = 0$$

which describes the motion of a fluid particle if the inter-particle interactions are completely neglected. The solution is $\mathbf{u}(\mathbf{x}, t) = \mathbf{u}(\mathbf{a}, 0)$ where \mathbf{a} is the initial location of the fluid particle which locates at \mathbf{x} at time t . Thus, from the Lagrangian point of view

$$\mathbf{x}(t) = \mathbf{a} + t\mathbf{u}(\mathbf{a}, 0),$$

and the dynamics is reduced to a linear map $\mathcal{L} : \mathbf{a} \rightarrow \mathbf{x}$ (the minimal Lagrangian map [6]), which maps the initial Gaussian random velocity field to a distorted, non-Gaussian field. In the MTLM method, the map is applied recursively, at increasingly finer grids. The incompressibility condition is re-enforced after each mapping by projection onto the divergence-free sub-space. Then, the velocity field is re-scaled, so that the energy spectrum will return to the initial one (usually the Kolmogorov $-5/3$ spectrum in the inertial range with certain empirical functional form in the dissipation range). In other words, at each iteration, a mapping-projection-rescaling three-step procedure is performed. This procedure is first applied to a coarse-grained velocity obtained by low-pass filtering the initial Gaussian velocity field. After the

three-step procedure is applied, the distorted field is assembled with the high wavenumber components of the original Gaussian field, to which the next iteration applies. The new iteration repeats the above procedure but with a finer grid. The iterations are repeated until the last one which is applied to the whole velocity field.

For more details about the MTLM procedure, the readers are referred to [6, 5]. For the data in this paper, the MTLM is applied to a 256^3 uniform grid in the domain $[0, 2\pi]^3$. 6 iterations are used, with resolutions $8^3, 16^3, 32^3, 64^3, 128^3$, and 256^3 , respectively.

We have generalized the MTLM procedure to helical turbulence. For helical turbulence, we have to maintain the helicity spectrum in each iteration. This is accomplished using the helical wave decomposition of the velocity field, as briefly explained below. Given the Fourier components $\hat{\mathbf{u}}(\mathbf{k})$ of the velocity field, it can be decomposed into the sum of two helical waves \mathbf{h}_+ and \mathbf{h}_- [11]:

$$\hat{\mathbf{u}}(\mathbf{k}) = a_+(\mathbf{k})\mathbf{h}_+(\mathbf{k}) + a_-(\mathbf{k})\mathbf{h}_-(\mathbf{k}). \quad (5)$$

According to the properties of the helical waves, the vorticity field is given by

$$\hat{\boldsymbol{\omega}}(\mathbf{k}) = k(a_+\mathbf{h}_+ - a_-\mathbf{h}_-). \quad (6)$$

At the rescaling stage of the MTLM procedure, we introduce two functions $f_+(k)$ and $f_-(k)$, and define the rescaled velocity as

$$\hat{\mathbf{u}}_s(\mathbf{k}) = f_+a_+(\mathbf{k})\mathbf{h}_+(\mathbf{k}) + f_-a_-(\mathbf{k}, t)\mathbf{h}_-(\mathbf{k}). \quad (7)$$

As a consequence,

$$\hat{\boldsymbol{\omega}}(\mathbf{k}) = k(f_+a_+\mathbf{h}_+ - f_-a_-\mathbf{h}_-) \quad (8)$$

By definition, the energy and helicity spectra are $E(k) = (1/2) \oint \hat{\mathbf{u}}_s^* \cdot \hat{\mathbf{u}}_s dS_k$, and $H(k) = \oint \hat{\boldsymbol{\omega}}_s^* \cdot \hat{\mathbf{u}}_s dS_k$, respectively, where S_k is a spherical shell in the Fourier space with radius k . Hence one finds:

$$E(k) = \frac{1}{2} \left[|f_+|^2 \oint |a_+|^2 dS_k + |f_-|^2 \oint |a_-|^2 dS_k \right] \quad (9)$$

$$H(k) = k \left[|f_+|^2 \oint |a_+|^2 dS_k - |f_-|^2 \oint |a_-|^2 dS_k \right] \quad (10)$$

Given the original velocity field $\hat{\mathbf{u}}$, one can find the helical wave components $a_+(\mathbf{k})$ and $a_-(\mathbf{k})$, and hence calculate the integrals in the above equations. With $E(k)$ and $H(k)$ prescribed either as analytical functions or from DNS data, $f_+(k)$ and $f_-(k)$ can then be solved from the above two equations. With $f_-(k)$ and $f_+(k)$ found this way, the velocity field $\hat{\mathbf{u}}_s$ have the prescribed energy and helicity spectra.

4 Results and discussion

4.1 Parameters of the velocity fields

To generate the DNS data sets, we solve the Navier-Stokes equations using the pseudo-spectral method in a periodic $[0, 2\pi]^3$ box. Statistically stationarity is maintained by a forcing term that injects energy and helicity into the flow field at constant rates $\epsilon_f = 0.1$ and $\eta_f = 0.3$, respectively. The details of the forcing term, in particular the method to inject helicity, are explained in [12]. The energy and helicity spectra are plotted in Fig. 1. A short $-5/3$ range is observed in both the energy and helicity spectra.

The energy and helicity spectra of the DNS data are used as the input for the MTLM synthetic fields. Five MTLM fields are generated, with same spectra and parameters but different realizations of initial Gaussian fields. The statistics are averaged over the five fields.

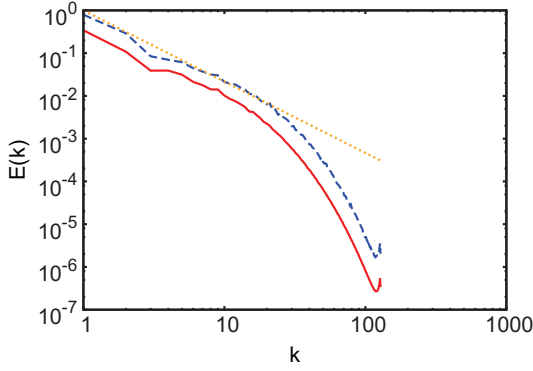


Figure 1: The energy and helicity spectra of the DNS data

4.2 SGS energy and helicity dissipation

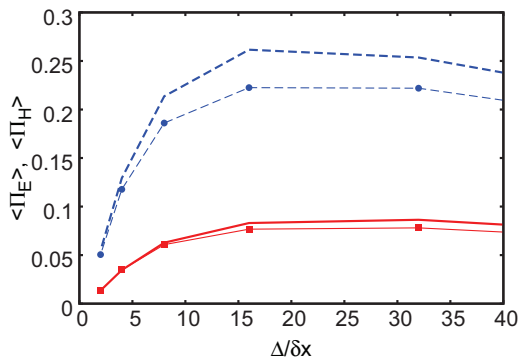


Figure 2: The mean SGS energy and helicity dissipation rates at different filter scales

Fig. 2 shows the mean SGS energy and helicity dissipation rates as functions of filter scales. The lines without symbols are DNS results. For turbulence with infinite Reynolds number, the SGS dissipation rates reach constant values in the inertial ranges and equal the injection rates (0.1 for energy and 0.3 for helicity). For the data in this paper, the DNS results reach approximate plateaus. The plateau values, however, are smaller than the injection rates due to the small Reynolds number. Interestingly, the results calculated from the MTLM fields also approach approximate constant values, although the values are somewhat smaller than the DNS values. Thus, it appears that the MTLM procedure can account for most of the energy flux as well as the helicity flux across the spectra. Note that, as is shown in [13], SGS helicity dissipation is generated when the resolved vortex tubes with non-uniform diameter are twisted. The above results show that the MTLM procedure can capture, at least partially, such subtle effects.

The probability density functions (PDFs) for the SGS dissipation rates are compared in Fig. 3. The DNS results show the well-known features. The PDF for Π_E shows strong positive skewness as well as significant probability for negative fluctuations, i.e., back-scattering. The PDF for Π_H is more intermittent than that for Π_E . The MTLM results, shown with symbols, reproduce all the features of the DNS results, although it also shows that the MTLM results underestimate to some degree the intermittency of the SGS dissipations.

Fig. 4 plots the conditionally averaged SGS energy dissipation for both the DNS and MTLM fields. For the dissipation conditioned on the magnitude of the strain rate tensor, MTLM shows reasonable agreement with

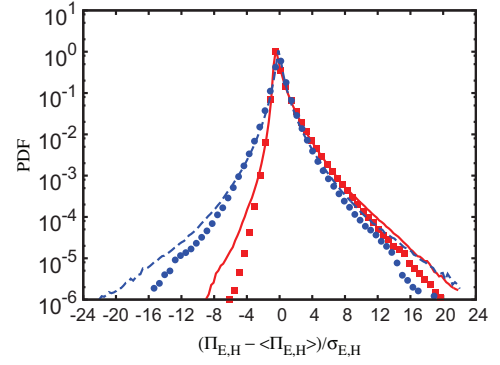


Figure 3: PDFs of normalized SGS helicity and energy dissipations. Solid line: Π_E for DNS; squares: Π_E for MTLM; dashed line: Π_H for DNS; circles: Π_H for MTLM. $\Delta = 16\delta x$

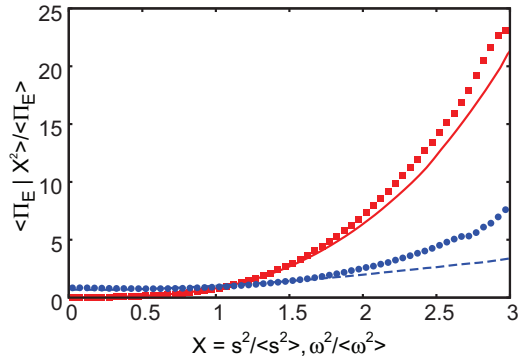


Figure 4: Mean SGS energy dissipation rate conditioned on $s^2/\langle s^2 \rangle$ where $s^2 \equiv 2\tilde{S}_{ij}\tilde{S}_{ij}$, and $\omega^2/\langle \omega^2 \rangle$ where $\omega = |\tilde{\omega}|$. The averages are normalized by $\langle \Pi_E \rangle$. $\Delta = 16\delta x$

DNS values. For large strain rates MTLM overestimates the results, at the order of or smaller than 10%. As for the results conditional on vorticity, the SGS energy dissipation in DNS shows only weak dependence on the magnitude of vorticity, whereas the energy dissipation in the MTLM fields increases slowly with the magnitude of vorticity. This discrepancy is consistent with the known properties of the MTLM fields. It has been found in [6] and [5] that the MTLM fields appear to be missing concentrated vortex filaments at small scales, compared with DNS data. Rather, the small scales are populated by vortex sheets, where strong vorticity and strain rate coincide. The stronger correlation between vorticity and strain rate generates the somewhat overestimated correlation between the vorticity and the SGS energy dissipation shown in Fig. 4.

4.3 Geometrical statistics

We first look into the shape of the SGS stress tensor. Let $(-\tau)_\alpha$, $(-\tau)_\beta$ and $(-\tau)_\gamma$ be the eigenvalues of the deviatoric part of the (minus) SGS tensor $-\tau_{ij}^d \equiv -\tau_{ij} + (\tau_{kk}/3)\delta_{ij}$, such that $(-\tau)_\alpha \geq (-\tau)_\beta \geq (-\tau)_\gamma$ and $(-\tau)_\alpha + (-\tau)_\beta + (-\tau)_\gamma = 0$. The shape of the stress tensor is described by the factor

$$s_\tau^* \equiv \frac{-3\sqrt{6}(-\tau)_\alpha(-\tau)_\beta(-\tau)_\gamma}{[(\tau)_\alpha^2 + (-\tau)_\beta^2 + (-\tau)_\gamma^2]^{3/2}}. \quad (11)$$

$s_\tau^* = 1$ corresponds to an eigenvalue ratio of $(-\tau)_\alpha : (-\tau)_\beta : (-\tau)_\gamma = 2 : -1 : -1$, hence the stress $-\tau_{ij}^d$ tends

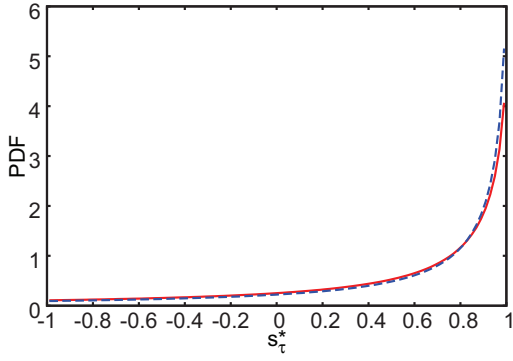


Figure 5: The PDFs for the shape factor s_τ^* of the SGS stress. Solid line: DNS result; dashed line: MTLM. $\Delta = 16\delta x$

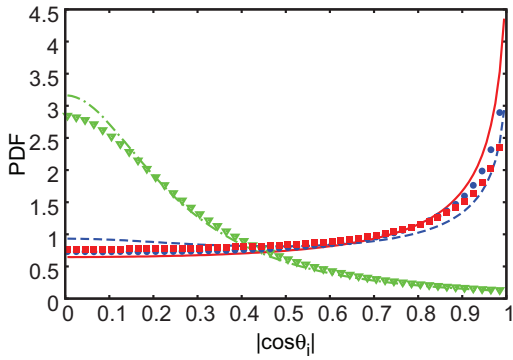


Figure 6: PDFs of $|\cos \theta_i| \equiv |\tilde{\omega} \cdot \mathbf{e}_i|$ where $\mathbf{e}_1 = (-\boldsymbol{\tau})_\alpha$ (solid line and squares), $\mathbf{e}_2 = (-\boldsymbol{\tau})_\beta$ (dashed line and circles), and $\mathbf{e}_3 = (-\boldsymbol{\tau})_\gamma$ (dash-dotted line and gradients). Lines are for DNS results and symbols are for MTLM results. $\Delta = 16\delta x$

to have an axisymmetric state where resolved eddies are stretched in one direction and contracted axisymmetrically in the other two directions. The PDFs for s_τ^* are shown in Fig. 5. The DNS result reproduces the strong peak at $s_\tau^* = 1$, which has been known since, e.g., [14]. The PDF for the MTLM field again also shows a strong peak at $s_\tau^* = 1$, in close resemblance to the DNS results. The peak is somewhat stronger than the DNS result. The difference suggests that the preferential alignment is stronger in vortex sheets.

Non-trivial alignment configurations have been observed between the SGS stress tensor, the vorticity $\tilde{\omega}$, and the stress tensor \tilde{S}_{ij} as well as other quantities. The alignment between the vorticity vector $\tilde{\omega}$ and the eigenvectors of the SGS stress $-\tau_{ij}$ is shown in Figure 6, where $(-\boldsymbol{\tau})_\alpha$, $(-\boldsymbol{\tau})_\beta$ and $(-\boldsymbol{\tau})_\gamma$ are the eigenvectors. As is observed in DNS [15], there is a strong tendency for vorticity to align with the most extensive eigenvector $(-\boldsymbol{\tau})_\alpha$ or the intermediate eigenvector $(-\boldsymbol{\tau})_\beta$ of $-\tau_{ij}$, and alignment with the former is stronger than that with the latter. Meanwhile, $\tilde{\omega}$ tends to be perpendicular to the third eigenvector. These features are all reproduced by the DNS results in Fig. 6. The MTLM results compare well with the DNS results, although the alignment with the intermediate eigenvector appears to be stronger than that with the most extensive one. As is suggested in [14], the alignment between $\tilde{\omega}$ and $(-\boldsymbol{\tau})_\alpha$ comes from the contributions of strong concentrated vorticity. This explanation is consistent with the observation in Fig. 6 and the fact that MTLM fields contain insufficient vortex filaments.

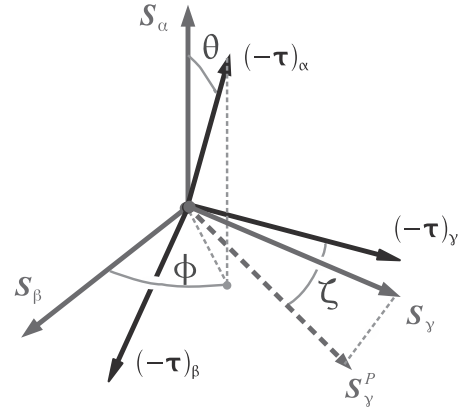


Figure 7: The angles describing the relative orientation of the eigen-frames of $-\tau_{ij}$ and \tilde{S}_{ij}

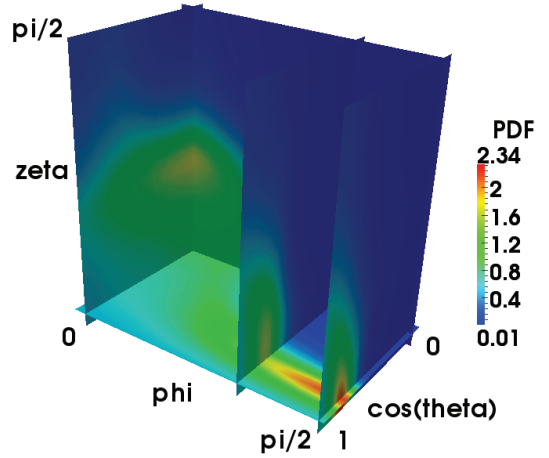


Figure 8: The joint PDF of $(\cos \theta, \phi, \zeta)$ for the eigen-frames of \tilde{S}_{ij} and $-\tau_{ij}$ in the DNS data. $\Delta = 16\delta x$

We next examine the alignment between $-\tau_{ij}$ and the filtered strain rate tensor \tilde{S}_{ij} . To describe the relative alignment between two tensors, we used the three angles θ , ϕ , and ζ defined in Fig. 7 [14]. \mathbf{S}_α , \mathbf{S}_β and \mathbf{S}_γ in the figure are the eigenvectors of \tilde{S}_{ij} , corresponding to eigenvalues $S_\alpha \geq S_\beta \geq S_\gamma$. For a Gaussian random field, the joint PDF of $\cos \theta$, ϕ and ζ is roughly uniform. Thus deviation from the uniform distribution indicates non-trivial geometrical structures in the DNS/MTLM fields. Fig. 8 and Fig. 9 plot the results for the DNS data and MTLM fields, respectively. The PDF for the MTLM fields has two peaks, with a value 4.16 at $(\cos \theta, \phi, \zeta) \approx (0.75, \pi/2, 0)$, and a value 1.22 at approximately $(0., 0., 0.71)$. The corresponding angles (θ, ϕ, ζ) are approximately $(41^\circ, 90^\circ, 0^\circ)$, and $(90^\circ, 0^\circ, 41^\circ)$, which we will call configuration A and B respectively. The double-peak structure has been observed before in experiments and numerical simulations [14] and [15], and also in our DNS results shown in Fig. 8. For DNS data, the locations of the peaks are at approximately $(\cos \theta, \phi, \zeta) = (0.78, \pi/2, 0)$, with peak value 2.34, and $(0., 0., 0.76)$, with peak value 1.65. In terms of the angles, the locations are $(\theta, \phi, \zeta) = (39^\circ, 90^\circ, 0)$, and $(90^\circ, 0^\circ, 44^\circ)$. Therefore, the preferential configurations for the alignment in the MTLM fields are the same as those in the DNS fields. However, the probabilities to observe the configurations are somewhat different. The MTLM fields have a much higher probability to observe

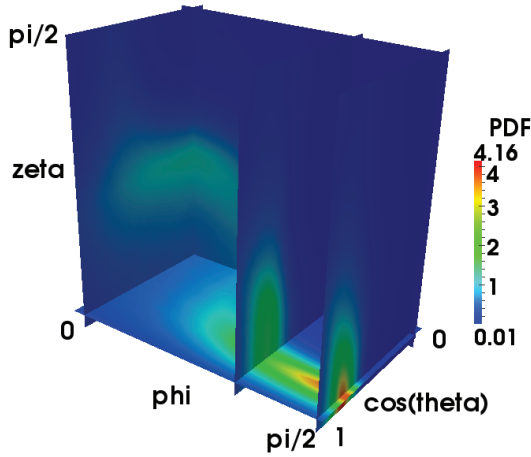


Figure 9: The joint PDF of $(\cos\theta, \phi, \zeta)$ for the eigenframes of \tilde{S}_{ij} and $-\tau_{ij}$ in the MTLM fields. $\Delta = 16\delta x$

configuration A (4.16 compared with 2.34), whereas the probability for configuration B is slightly smaller than that in the DNS fields (1.22 versus 1.65). The difference again can be related to the lack of vortex tubes or filaments in MTLM fields. As is shown in [14], the configuration B is more probable in high vorticity region, which can be plausibly explained in terms of the stretching of strong vortex tubes. Thus it is not surprising that MTLM fields has a smaller probability to observe configuration B. On the other hand, the stronger peak for configuration A in MTLM fields does not have an explanation yet. Nevertheless, we observe that difference in Figs. 8 and 9 is consistent with the results in Fig. 6. As is commented in [15], configuration A in the joint PDF is observed when ω aligns with β_τ , whereas configuration B is observed when ω aligns with α_τ . Fig. 6 shows that in MTLM field it is more probable for ω to align with β_τ , and hence more probable to observe configuration A in the joint PDF as well.

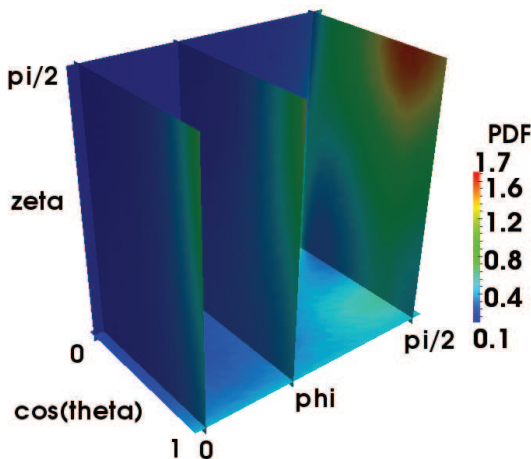


Figure 10: The joint PDF of $(\cos\theta, \phi, \zeta)$ for the eigenframes of \tilde{R}_{ij} and $-\tau_{ij}$ in the DNS data. $\Delta = 16\delta x$

A non-trivial alignment between \tilde{R}_{ij} and $-\tau_{ij}$ is reported in [13], in which the intermediate eigenvector \mathbf{R}_β aligns with $(-\tau)_\gamma$ and simultaneously $(-\tau)_\alpha$ makes a 45° angle with \mathbf{R}_α (the eigenvector corresponding to the largest eigenvalue R_α). The alignment is another signature of the structure of turbulent vorticity fields. The DNS result is plotted in Fig. 10 for com-

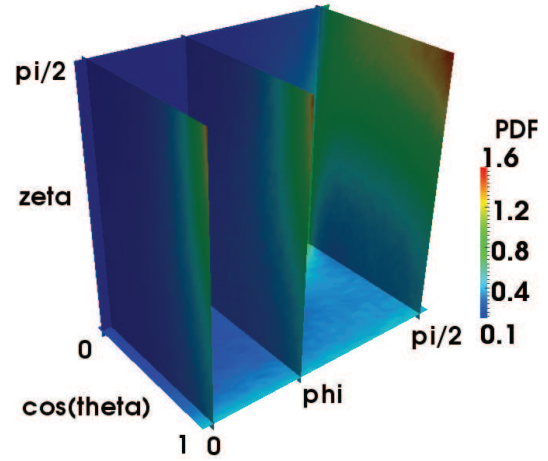


Figure 11: The joint PDF of $(\cos\theta, \phi, \zeta)$ for the eigenframes of \tilde{R}_{ij} and $-\tau_{ij}$ in the MTLM fields. $\Delta = 16\delta x$

pleteness. The peak in the joint PDF corresponds to the peak described above. The MTLM result is shown in Fig. 11. Interestingly, the peak is now shifted to $(\cos\theta, \phi, \zeta) = (1, \pi/2, \pi/2)$ and corresponds to a configuration where \mathbf{R}_α and \mathbf{R}_β simultaneously aligns with $(-\tau)_\alpha$ and $(-\tau)_\gamma$, respectively. The difference indicates that \tilde{R}_{ij} gives more detailed description of the vorticity field, so that the differences in the MTLM and DNS fields are captured in the joint PDF.

5 Conclusions

We present a study on the synthetic turbulent fields generated by the multi-scale turnover Lagrangian map in comparison with hydrodynamic turbulence generated by direction numerical simulations. We look into the statistics of the MTLM fields related to the subgrid-scale stresses, and generalize the method to consider helical turbulence. We observe that MTLM-generated synthetic fields reproduce many of the statistics to good approximations. The MTLM fields reproduce approximately constant positive mean subgrid-scale energy and helicity dissipation rates in the inertial ranges, even though the values are somewhat underestimated. Geometrical statistics are also reproduced, with some small quantitative difference. The analysis demonstrate that the simple MTLM procedure can account for the essential features of inter-scale interaction in helical turbulence. The differences between MTLM and DNS give some hints on the effects of the different structures (such as vortex sheets and vortex tubes) in turbulent fields.

Acknowledgement

The authors gratefully acknowledge the support from the Royal Society International Travel Grants (TG090539). CR also acknowledges the support from Project FONDECYT 11080025.

References

- [1] F. Nicolleau and J. C. Vassilicos. Turbulent pair diffusion. *Phys. Rev. Lett.*, 90:024503, 2003.
- [2] R. H. A. Ijzermans, E. Meneguz, and M. W. Reeks. Segregation of particles in incompressible random

- flows: singularities, intermittency and random uncorrelated motion. *J. Fluid Mech.*, 653, 2010.
- [3] L. Chevillard, R. Robert, and V. Vargas. A stochastic representation of the local structure of turbulence. *Europhys. Lett.*, 89, 2010.
- [4] A. Juneja, D. P. Lathrop, K. R. Sreenivasan, and G. Stolovitzky. Synthetic turbulence. *Phys. Rev. E*, 49, 1994.
- [5] C. Rosales and C. Meneveau. Anomalous scaling and intermittency in three-dimensional synthetic turbulence. *Phys. Rev. E*, 78:016313, 2008.
- [6] C. Rosales and C. Meneveau. A minimal multi-scale Lagrangian map approach to synthesize non-Gaussian turbulent vector fields. *Phys. Fluids*, 18:075104, 2006.
- [7] A. Brissaud, U. Frisch, J. Leorat, M. Lesieur, and A. Mazure. Helicity cascades in fully developed isotropic turbulence. *Phys. Fluids*, 16:1366, 1973.
- [8] S. Y. Chen, R. E. Ecke, G. L. Eyink, X. Wang, and Z. Xiao. Physical Mechanism of the two-dimensional Enstrophy Cascade. *Phys. Rev. Lett.*, 91:214501, 2003.
- [9] Y. Li and C. Meneveau. Origin of non-Gaussian statistics in hydrodynamic turbulence. *Phys. Rev. Lett.*, 95:164502, 2005.
- [10] Y. Li and C. Meneveau. Intermittency trends and Lagrangian evolution of non-Gaussian statistics in turbulent flow and scalar transport. *J. Fluid Mech.*, 558:133–142, 2006.
- [11] Q. Chen, S. Chen, and G. L. Eyink. The joint cascade of energy and helicity in three-dimensional turbulence. *Phys. Fluids*, 15(2):361–374, 2003.
- [12] Y. Li, C. Meneveau, S. Chen, and G. L. Eyink. Subgrid-scale modeling of helicity and energy dissipation in helical turbulence. *Phys. Rev. E*, 74:026310, 2006.
- [13] Y. Li. Geometrical statistics and vortex structures in helical and nonhelical turbulence. *Phys. Fluids*, 22:035101, 2010.
- [14] B. Tao, J. Katz, and C. Meneveau. Statistical geometry of subgrid-scale stresses determined from holographic particle image velocimetry measurements. *J. Fluid Mech.*, 457:35–78, 2002.
- [15] K. Horiuti. Roles of non-aligned eigenvectors of strain-rate and subgrid-scale stress tensors in turbulence generation. *J. Fluid Mech.*, 491:65–100, 2003.

SINGULARITIES IN THE PARTICLE CONCENTRATION FIELD OF INERTIAL PARTICLES IN TURBULENT FLOWS

E. Meneguz and M. W. Reeks

*School of Mechanical and Systems Engineering, Stephenson Building
Newcastle University, Newcastle upon Tyne, NE1 7RU, UK*

1 Introduction

There have been numerous studies devoted to the segregation of particles/droplets in turbulent flows, given its relevance in many environmental and industrial processes (warm rain initiation, [1], and the formation and growth of PM10 particulates in the atmosphere being just two of a multitude of examples). The early studies of segregation showed it to be a maximum when $St \sim 1$, St being the particle Stokes number defined as the ratio of particle response time to the time scale of the small scales of the turbulence. Along with this went the now traditional view that depending upon St , particles are centrifuged out of regions of high vorticity into the high strain regions in between (e.g. [2], [3]). Since these early studies, the problem has been addressed from a number of different perspectives which have not only added insight but challenged this traditional picture of segregation and the role of particle inertia. [4] and [5] have demonstrated for instance that there exists a strong correlation between the segregation of inertial particles and the location of zero acceleration points in DNS of turbulent flows when the Reynolds number is high. Similarly, in Kinematic Simulations (KS) where the sweeping of small scales by large scales do not exist, they have suggested that heavy particles anti-cluster with zero velocity points [4]. Recently, [6] proposed an alternative viewpoint of segregation for $St \gg 1$, involving the history of the particles' compressibility and the accumulation of high concentrations (singularities) within an envelope of *caustics* where particle trajectories cross one another. The occurrence of crossing trajectories is also an important feature of the recent studies of [7] and [8] in which they partition the particle motion into a spatially random uncorrelated motion (RUM) and a mesoscopic motion derived from a smoothly varying particle velocity field which is responsible for the spatially correlated part of the particle motion. By measuring the spatial velocity correlation between pairs of particles, they were able to calculate the contribution the RUM and the mesoscopic velocity field make to the particle's turbulent kinetic energy, and how this varied with St . *Sling-shot* events measured by [9, 10] and [11] are also associated with singularities and RUM as they embody the idea of a particle's accumulated memory of many encounters with turbulent structures similar to the influence of memory on compressibility. In these studies, the authors use the indirect Lagrangian method (ILM), which consists on tracking the evolution of the inverse deformation tensor associated with the particle velocity field along each particle trajectory, requiring the integration of the particle velocity gradient tensor. In contrast to the approach we present, their equations are explicitly non-linear and the existence of singularities is inferred by the change of sign of all the components of the velocity

tensor whenever this exceeds a certain threshold value. In this paper, the Full Lagrangian Method (FLM) [12] is exploited to measure the compressibility of an elemental volume of particles in Kinematic Simulations (KS) of incompressible homogeneous isotropic turbulent flow. In this study [13] we extend our previous KS study [14] by examining in detail the statistics of the compressibility of the particle phase and the rate of occurrence of singularities in the particle concentration field. In addition, we explore the relationships between intermittency as reflected in the moments of the particles concentration and the occurrence of RUM, with the aim of providing a more complete understanding of the occurrence of both features.

2 Physical-mathematical model

We consider a point-particle approach with the dispersed particle phase described as a continuum. Under the assumption that the density of the particle is much higher than the density of the carrier flow, that is $\rho_p/\rho \gg 1$, and neglecting Brownian motion and any body force, the equation of motion of heavy particles reduces to:

$$\frac{d\mathbf{x}}{dt} = \mathbf{v}, \quad \frac{d\mathbf{v}}{dt} = \frac{1}{\tau_p} (\mathbf{u} - \mathbf{v}), \quad (1)$$

where τ_p is the particle relaxation time defined as $\tau_p \equiv 2a_p^2\rho_p/9\nu\rho$.

As previously mentioned (see [12], [15] and [16]), the FLM is based upon the evaluation of the second order deformation tensor $J_{ij} = \partial x_i / \partial x_{0j}$ along the particle trajectory defined by where \mathbf{x}_0 represents the position of the centre of the infinitesimally small volume surrounding each particle at some initial time $t = 0$. The equations of motion of J_{ij} are obtained by differentiating to x_{0j} so that :

$$\frac{dJ_{ij}}{dt} = \dot{J}_{ij}, \quad \frac{d}{dt} \dot{J}_{ij} = \frac{1}{\tau_p} \left(\frac{\partial u_i}{\partial x_k} J_{kj} - \dot{J}_{ij} \right). \quad (2)$$

from which we calculate $|J| = \det(J_{ij})$. As in [14], we are specifically interested in the compression $\mathcal{C}(t) = \ln |J(t)|$ and the rate of compression $\dot{\mathcal{C}}$ which we define as the compressibility (noting its equivalence to the divergence of the particle velocity field along a particle trajectory). $|J|$ can be used to calculate the long term average compressibility $\langle \dot{\mathcal{C}}(\infty) \rangle$. In addition, all the spatially averaged moments of the particle number concentration $n(\mathbf{x}, t)$ can be calculated by computing the particle average of the moments of $|J|$, since it holds that $\bar{n}^\alpha = \langle |J|^{1-\alpha} \rangle$, where $\bar{(\cdot)}$ refers to a volume average, $\langle \cdot \rangle$ an ensemble average along all particle trajectories and α can be any real number.

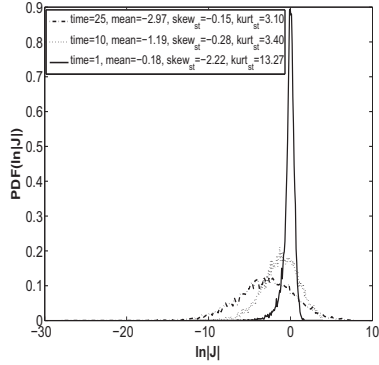


Figure 1: PDF of $\mathcal{C}(t)$ for $St = 0.5$.

With KS, a ‘synthetic’ turbulent flow is created not by solving the NS equations but representing the fluid velocity field as a truncated Fourier series of N modes. A turbulent velocity field is kinematically simulated in a three-dimensional periodic box similar to e.g. [17], [18] and [19]. The modes are chosen in such a way that the associated energy spectrum of the flow field approximates the form originally proposed by [20]. In this work, the number of modes is $N = 200$. All variables are made dimensionless using the typical wavenumber $\kappa_0[m^{-1}]$, and a typical velocity scale of the flow, $u_0[m/s]$.

The fluid velocity field can be written as:

$$\mathbf{u}(\mathbf{x}, t) = \sum_{n=1}^N \left[\frac{\mathbf{a}^{(n)} \times \boldsymbol{\kappa}^{(n)}}{|\boldsymbol{\kappa}^{(n)}|} \cos(\boldsymbol{\kappa}^{(n)} \cdot \mathbf{x} + \omega^{(n)}t) + \frac{\mathbf{b}^{(n)} \times \boldsymbol{\kappa}^{(n)}}{|\boldsymbol{\kappa}^{(n)}|} \sin(\boldsymbol{\kappa}^{(n)} \cdot \mathbf{x} + \omega^{(n)}t) \right], \quad (3)$$

with random coefficients $\mathbf{a}^{(n)}$ and $\mathbf{b}^{(n)}$, random wavenumbers $\boldsymbol{\kappa}^{(n)}$, and random wave frequencies $\omega^{(n)}$. It is noted that $\nabla \cdot \mathbf{u} = 0$, i.e. the flow is incompressible. For details about how the random coefficients, random wavenumbers and wave frequencies are constructed, see [14].

3 Statistics of compression, singularities and RUM

The probability density function (PDF) of the compression $\mathcal{C} \equiv \ln|J|$ is calculated, i.e. $P(\mathcal{C}, t)$: Figure 1 shows the time evolution of this distribution for $St = 0.5$. The values assumed by the third and fourth moments around the mean (respectively the skewness $\mu_3/\mu_2^{3/2}$, and the kurtosis μ_4/μ_2^2 where μ_k denotes the k central moment) are shown in the legend of the figure at three different times $t = 1$, $t = 10$, and $t = 25$, indicating that as time increases the distribution approaches a Gaussian with negative mean. This result is confirmed by [21] who used a method based on a Voronoi tessellation to calculate the particle concentration and showed that the distribution of Voronoi areas is log-normal.

It is worth noticing that this result is also true for $\langle \mathcal{C} \rangle \geq 0$ and $St \geq St_c$, where St_c is the critical St for the flow field considered, below which the average compressibility is negative and above which is positive. It is believed that the explanation for Gaussianity is similar to that for the occurrence of a Gaussian distribution of displacements [22], with $\mathcal{C}'(t)$, the fluctuating value of $\mathcal{C}(t)$

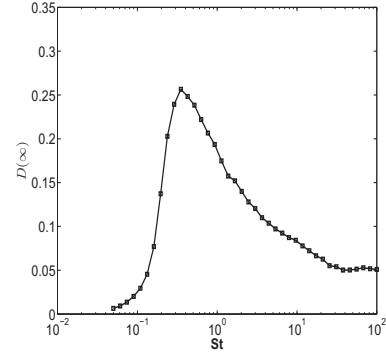


Figure 2: Long term limit of the compression diffusion coefficient, $D_c(\infty)$ as a function of St .

about its mean, being in the limit of $t \gg T_{\dot{\mathcal{C}}}$ a summation of changes $\Delta \mathcal{C}'$ in subintervals Δt ($T_{\dot{\mathcal{C}}} \ll \Delta t \ll t$) which are statistically independent of one another (where $\dot{\mathcal{C}}$ is the time derivative of $\mathcal{C}(t)$ and $T_{\dot{\mathcal{C}}}$ is the integral timescale of $\dot{\mathcal{C}}$). The same argument would not apply to the compressibility which is expected to be non-Gaussian. Note that the occurrence of both positive and negative compression is consistent with the remark that $\langle \mathcal{C} \rangle \geq 0$ does not imply that $\mathcal{C} \geq 0$ and vice versa.

The rate of increase in the width of $P(\mathcal{C}, t)$ defines a compression diffusion coefficient

$$D_c(t) = \frac{1}{2} \frac{d}{dt} \langle \mathcal{C}'^2 \rangle = \langle \mathcal{C}'(t) \dot{\mathcal{C}}'(t) \rangle \quad (4)$$

where $\dot{\mathcal{C}}'(t)$ is the fluctuating component of $\dot{\mathcal{C}}(t)$ with respect to its mean. For $t \gg T_{\dot{\mathcal{C}}}$ for which $\dot{\mathcal{C}}'(t)$ is a stationary random variable, $D_c(t)$ approaches an asymptotic limit $D_c(\infty)$ given by

$$D_c(\infty) = \int_0^\infty ds \langle \dot{\mathcal{C}}'(0) \dot{\mathcal{C}}'(s) \rangle = \langle \dot{\mathcal{C}}'^2(\infty) \rangle T_{\dot{\mathcal{C}}}. \quad (5)$$

Implicit in this finite limit for $D_c(t)$ is that for $t \gg T_{\dot{\mathcal{C}}}$.

$$\langle \mathcal{C}'^2(t) \rangle \rightarrow 2D_c(\infty)t \quad (6)$$

This result together with the approach to Gaussianity confirm what was suggested in [15] for simple random flows, but now true also for more complex stationary random flow velocity fields, namely that for $t \gg T_{\dot{\mathcal{C}}}$ a Gaussian diffusion process, i.e. convection with simple gradient diffusion, accurately describes the dispersion of $\mathcal{C}(t)$ as well as processes that depend on the m -th central moments of \mathcal{C} for $m \leq 4$, thus $P(\mathcal{C}, t)$ is described by an equation of the form:

$$\frac{\partial P}{\partial t} + \langle \dot{\mathcal{C}} \rangle \frac{\partial P}{\partial \mathcal{C}} = D_c(\infty) \frac{\partial^2 P}{\partial \mathcal{C}^2} + \delta(\mathcal{C})\delta(t). \quad (7)$$

$D_c(t)$ has been evaluated in the long term limit and is shown in Figure 2 as a function of Stokes number St . It can be seen that $D_c(\infty)$ is zero for $St = 0$ and has a maximum when $St \sim 0.3$ which as it turns out (within statistical error) is the same value of St as that corresponding to the maximum value of the net compression. For $St > 0.3$, the diffusion coefficient decreases monotonically to a constant value (~ 0.05). The implication

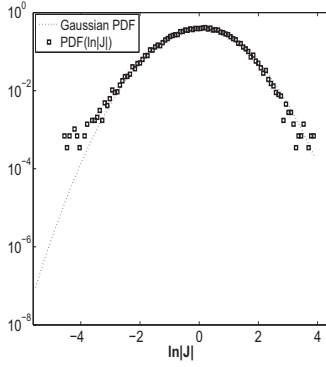


Figure 3: Standardised PDF of $\mathcal{C}(t)$ compared with Gaussian trend, $St = 0.5$.

of Equation (7) in the long term is that convection dominates over dispersion since

$$\frac{\langle \mathcal{C}'^2 \rangle^{1/2}}{\langle \mathcal{C} \rangle} = \frac{(2D_c(\infty)t)^{1/2}}{\langle \dot{\mathcal{C}} \rangle t} \sim t^{-1/2}. \quad (8)$$

In other words, as $t \rightarrow \infty$ the compression would contract to a precise value $\langle \dot{\mathcal{C}} \rangle t$. However this is true only ignoring the influence of the tail of the distribution of $P(\mathcal{C})$ for $\mathcal{C} \leq 0$ since the results in Figure 3 suggests that

$$\frac{\langle \mathcal{C}'^{2m} \rangle^{1/2m}}{\langle \mathcal{C} \rangle} \sim t^\beta \quad (9)$$

with $\beta > 0$ for $m > 2$, in contrast with a Gaussian distribution for which $\beta = -1/2$. The significant skewness towards negative compression (segregation) indicates that singularities in the flow are likely to play a significant role in determining the statistics of the segregation in these long term limits. In this regard Figure 3 shows $P(\mathcal{C}, t)$ obtained at $t = 25$ (see Figure 3) computed with 10^6 particles and normalised to zero mean and unit variance in order to obtain a universal curve. A Gaussian distribution is superimposed. Although the statistics in the tails are insufficient to draw a positive conclusion, it would appear that the deviation from Gaussianity is more pronounced in the left tail (negative compression) than in the right one. This would seem to indicate that the reason for this behaviour is the occurrence of singularities that only take place for $\langle \mathcal{C} \rangle \rightarrow -\infty$. In addition, the decay towards zero of the tail seems to be following an exponential function of the form $Y = A \exp(BX)$ where $x < 0$, therefore diverting from a Gaussian which decays parabolically.

The RUM component of the particle velocity is a measure of the decorrelation of the velocities of two nearby particles. Following the approach proposed by [7], the investigation is extended to the calculation of the mesoscopic and RUM contribution this time not of the velocity but of the compression in order to give more insight into the role that they individually play in the total distribution, especially in relation to the left negative tail, as observed in Figure 3. This is obtained as follows. The total domain is subdivided into $q_c^3 = 80^3$ cells, the trajectories of 10^6 particles are tracked in time and after several realisation of the flow the statistics are collected. For time $t = 30$ in dimensionless units, the RUM contribution is evaluated as:

$$\Phi(\mathbf{x}_{i|j}) = \mathcal{C}(\mathbf{x}_{i|j}) - \sum_{q_j^{-1}}^{q_j} \mathcal{C}(\mathbf{x}_i) \quad (10)$$

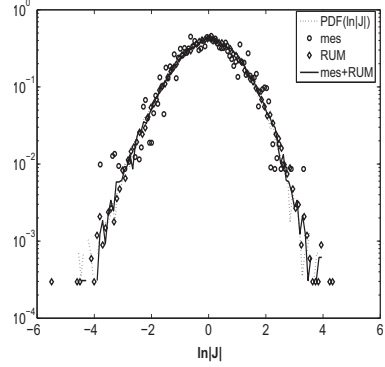


Figure 4: Comparison between mesoscopic and RUM contributions of the compression for $St = 1$.

where $\mathbf{x}_{i|j}$ is the position of the i -th particle found inside the j -th cell at the chosen time, and the subscript $j = 1 \dots q_c$. In order to collect reliable results, cells are filtered and only those with $q_j > 100$ are considered. The mesoscopic contribution is calculated as:

$$\Psi^*(j) = \sum_{i=1}^{q_j} \mathcal{C}(\mathbf{x}_i) / q_j - \bar{\mathcal{C}} \quad (11)$$

with $\bar{\mathcal{C}}$ denoting the particle averaged compression calculated all over the domain. Since in Equation (10) the RUM component is found as a function of the particle position, while in Equation (11) the mesoscopic contribution is evaluated per each cell, to make a sensible and effective comparison among the two quantities $\Psi(\mathbf{x}_{i|j})$ is calculated, which associates each particle with a certain value of $\Psi^*(j)$, depending on the cell in which it is located. As shown in Figure 4 for $St = 1$, both contributions and their summation are compared with the total distribution of \mathcal{C} . All distributions are normalised to zero mean and unit variance and rescaled to facilitate the comparison. Two important observations can be made: firstly, the summation of the mesoscopic and RUM component gives a curve collapsing on the PDF of the compression as expected. Secondly, it is clear (within statistical error) that the deviation from Gaussianity is mainly due to the RUM contribution ultimately linking it with the presence of singularities.

Singularities in the particle concentration field are instantaneous events which cannot be identified with box counting methods. The frequency of singularities is calculated in this study as $\omega_s = N_s / N_{max}$ and represents the ratio between the number of singularities per unit of time N_s and the total number of particles N_{max} . Each singularity is counted every time there is a change of sign in $J(t)$: in this way, the detection of singularities does not imply the use of a threshold which depends on the Stokes number, in contrast to the other recent work (e.g. Ducasse & Pumir, 2009). Figure 5 displays $\omega_s \tau_f$ as a function of St (where $\tau_f \equiv u_0 \kappa_0 / Ku$ is a typical correlation time of the flow, with Ku the Kubo number, u_0 and κ_0 respectively a typical velocity scale and wavenumber of the flow).

The frequency of singularities appears to be equal to zero in the proximity of $St = 0$, increasing until it reaches a maximum for $St \sim 1$ and decreasing towards an equilibrium value for $St \rightarrow 10^2$. Simulation data are well approximated by the curve $y = A \exp(-B/St) St^C$ with $A = 5.62 \times 10^{-5}$, $B = 0.80$ and $C = -0.70$. In the case of [10] the blow-up frequency of sling events multiplied

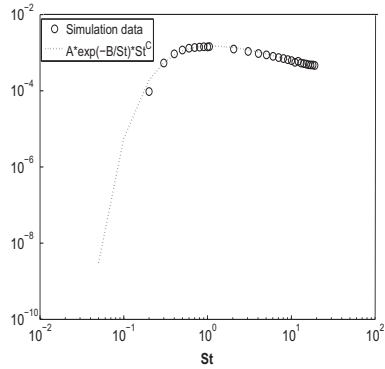


Figure 5: Frequency of singularities multiplied by the typical timescale of the flow, $\omega_s \tau_f$, as a function of St : comparison between simulation data and empirical curve ($A = 5.62 \times 10^{-5}$, $B = 0.80$ and $C = -0.70$).

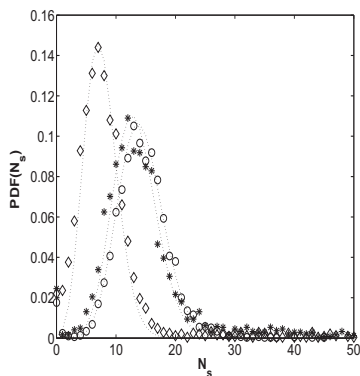


Figure 6: Standardised PDF of singularities; $St = 0.5$ (\diamond), $St = 1.0$ (*), and $St = 5.0$ (\circ); for each case the corresponding Poisson distribution is marked by a dashed line.

by the Kolmogorov timescale shows a dependence of the form: $St^{-2} \times \exp(-A/St) \times (B + CSt^c)$. Previously, [23] have argued a dependence $\sim \exp(-A/St)$.

In addition, the distribution of singularities is calculated over a fixed interval of time respectively for $St = 0.5$, $St = 1$, $St = 5$ as shown in Figure 6. Excluding the influence of an initial transient, when no singularities are observed, each standardised curve representing the PDF is well approximated by a Poisson distribution that describes the probability of the occurrence of an event (singularity) in a specified time span $[0, \Delta t]$ as $\sim \lambda \Delta t = \Lambda$; λ is the rate constant for the occurrence of singularities. The Poisson process implies that starting from some initial fully mixed equilibrium distribution, the decay in the number of particles that have not experienced a singularity is $\sim \exp(-\lambda t)$.

4 Conclusions

We have shown that the distribution of the compression deviates from a Gaussian curve, contrary to what usually assumed (e.g. [21]). The reason for this deviation is the occurrence of singularities, instantaneous events which correspond to very large concentration (in theory infinite) in the particle phase. By using the FLM, we have measured their frequency and showed that their PDF approximates a Poisson distribution whose width depends

on St . We also found that singularities are ultimately related to the RUM component of the compression as observed for $St = 1$.

For more details about this work see [13].

References

- [1] Shaw, R. A. *Particle-turbulence interactions in atmospheric clouds*. Ann. Rev. Fluid Mech. **35**, 183–227, (2003)
- [2] Crowe, C. T. Chung, J. N. & Troutt T. R. *Particle Two-Phase Flow* **626**. Heinemann, Oxford, (1993).
- [3] Wang, L. P. & Maxey, M. R. *Settling velocities and concentration distribution of heavy particles in homogeneous isotropic turbulence*. J. Fluid Mech. **256**, 27–68, (1993).
- [4] Chen, L. Goto, S. & Vassilicos, J. C. *Turbulent clustering of stagnation points and inertial particles*. J. Fluid Mech. **553**, 143–154, (2006).
- [5] Coleman, S. W. & Vassilicos J. C. *A unified sweep-stick mechanism to explain particle clustering in two- and three- dimensional homogeneous isotropic turbulence*. Phys. Fluids **21**, 113301–113310, (2009).
- [6] Wilkinson, M. Mehlig, B. Ostlund, S. & Duncan, K. P. *Unmixing in random flows*. Phys. Fluids **19**, 113303 (2007).
- [7] Fevrier, P. Simonin, O. & Squires, K. D. *Partitioning of particle velocity in gas-solid turbulent flows into a continuous field and a spatially uncorrelated random distribution; theoretical formalism and numerical study*. J. Fluid Mech. **553**, 1–46, (2005).
- [8] Masi, E. Riber, E. Sierra, P. Simonin, O. & Gicquel, L. Y. M. *Modeling the Random Uncorrelated Velocity Stress Tensor for Unsteady Particle Eulerian Simulation in Turbulent Flows*. In 7th Intl. Conf. on Multiphase Flows, Tampa, Florida, (2010).
- [9] Falkovich, G. & Pumir, A. *Intermittent distribution of heavy particles in a turbulent flow*. Phys. Fluids **16**(7) L47–L50, (2004).
- [10] Falkovich, G. & Pumir, A. *Sling effect in collisions of water droplets in turbulent clouds*. Am. Meteorol. Soc. **64**, 4497–4505, (2007).
- [11] Ducasse, L. & Pumir, A. *Inertial particle collisions in turbulent synthetic flows: Quantifying the sling effect*. Phys. Rev. E **80**, 066312, (2009).
- [12] Osipov, A. N. *Lagrangian modelling of dust admixture in gas flows*. Astrophys. Space Sci. **274**, 377–386.
- [13] Meneguz, E. & Reeks, M. W. *Statistical properties of particle segregation in homogeneous isotropic turbulence* J. Fluid Mech. **686**, 338–351, (2011)
- [14] IJzermans, R. H. A. Meneguz, E. & Reeks, M. W. *Segregation of particles in incompressible random flows: singularities, intermittency and random uncorrelated motion (RUM)*. J. Fluid Mech. **653**, 99–136, (2010).

- [15] Reeks, M. W. *Simulation of particle diffusion, segregation, and intermittency in turbulent flows*. In Proc. of IUTAM Symposium on Computational Modelling of Disperse Multiphase Flow (ed. S. Balachandar & A. Prosperetti). pp. 21–30. Elsevier (2004).
- [16] Healy, D. P. & Young, J. B. *Full Lagrangian methods for calculating particle concentration fields in dilute gas-particle flows*. in Proc. R. Soc. Lond. A **461**, 2197–2225, (2005).
- [17] Reeks, M. W. *Eulerian direct interaction applied to the statistical motion of particles in a turbulent fluid* J. Fluid Mech., **97**, 669–690, (1980).
- [18] Maxey, M. R. *The gravitational settling of aerosol particles in homogeneous turbulence and random flow fields*. J. Fluid Mech. **174**, 441–465, (1987).
- [19] Spelt, P. D. M. & Biesheuvel, A., *On the motion of gas bubbles in homogeneous isotropic turbulence* J. Fluid Mech., **336**, 221–244, (1997).
- [20] Kraichnan, R. H., *Diffusion by a random velocity field*, Phys. Fluids, **13**, 22–31, (1970).
- [21] Monchaux, R. Bourgoïn, M. & Cartellier, A. Preferential concentration of heavy particles: a Voronoï analysis. *Phys. Fluids*, **22**, 103304, (2010).
- [22] Taylor, G. I. *Diffusion by continuous movements*. Proc. London Math. Soc. s2 **20**(1), 196–212, (1922).
- [23] Wilkinson, M. & Mehlig, B. *Caustics in turbulent aerosols*. Europhys. Lett. **71**, 186–192, (2005).

CLUSTERING OF LADEN PARTICLES IN KINEMATIC SIMULATION FLOWS

F.C.G.A. Nicolleau, M. Farhan, and A.F. Nowakowski

*Sheffield Fluid Mechanic Group, University of Sheffield, Department of Mechanical Engineering
Mappin Street, Sheffield S1 3JD, United Kingdom*

Abstract

We present preliminary results using a simple synthetic turbulent model (periodic Kinematic Simulation) to understand the evolution of clouds formed of laden particles. In particular, we analyse the relative role of inertia and gravity in the long time geometrical structure of such clouds. This study is limited to isotropic incompressible flows.

1 Introduction

In most natural and industrial situations one may encounter, particles suspended in flows have a finite size and a mass density different from that of the carrier flow. Though a statistical description of such inertial particles in turbulent flow is of interest to engineering, it remains a challenge for researchers to find the exact parameters that affect the clustering of inertial particles in the flow field. In this contribution, we concentrate on two non-dimensional parameters, the Stokes number and the drift parameter, to quantify the clustering pattern of inertial particles.

The dynamics of such inertial particles is different from tracers and they form clusters. Unlike the tracer, particles with size comparable to molecular scales, inertial particles (like water drops in clouds) have finite size and have a much higher mass-density than the surrounding fluid. Thus while the former is passively advected by the fluid, and its motion at any time mimics that of the local fluid motion, the latter (inertial particle) may decorrelate from the advecting fluid motion owing to its inertia and gravity. This phenomenon is referred to in literature either as inertial clustering or preferential concentration.

The classical picture is that clustering of inertial particles in turbulence is the result of particles being centrifuged out of regions of high fluid vorticity (highly rotating) as a result of their inertia and thus preferentially concentrating in the regions of high strain. Evidence of inertial particles preferentially concentrating in regions of low vorticity and high strain is abundant [4].

Preferential concentrations (in the absence of gravity) of inertial particle suspensions in turbulent flows was studied in [2]. The concentration process was related to particles trajectories in phase space. A critical Stokes number was found above which the particles were space filling.

Kinematic Simulation has been heavily used to study particle-pairs but there is already a significant amount of work devoted to sets of more than two particles. In [8] particle triangles and tetrahedrons were studied in

two-dimensional KS and comparisons were made with experimental results. Triangles and tetrahedrons were further investigated in three-dimensional turbulence in [13] and for laden particles in [1].

Particles clouds have also been studied using KS. The fractal dimension of fluid particle clouds was studied in [12]. Segregation was investigated in [6] where collections of heavy and light small spherical particles initially well mixed with each other, were subjected to inertia and gravity. Kinematic simulation predicted that the turbulence can segregate heavy and light falling particles and leads to a well-defined segregation length scale.

The relation between stagnation points topology and the clustering of inertial particles in turbulent flows was investigated in [3].

2 Kinematic Simulation

We use Kinematic Simulations, KS, as a particular kind of synthetic turbulence models to study the preferential location of particles with inertia in the presence of gravity. (See e.g. [11] for more information on KS and synthetic turbulence models.)

The predetermined Eulerian field $u(x, t)$ based on [5] for incompressible isotropic turbulence is reduced to a truncated Fourier series. Here it is modified to model a periodic field, that is by contrast to [5], where one wavevector is randomly chosen for each wavenumber, wavevectors are deterministically chosen on a regular grid:

$$\mathbf{u}(\mathbf{x}, t) = \sum_{i=1}^N \sum_{j=1}^N \sum_{l=1}^N \mathbf{a}_{ijl} \cos(\mathbf{k}_{ijl} \cdot \mathbf{x} + \omega_{ijl} t) + \mathbf{b}_{ijl} \sin(\mathbf{k}_{ijl} \cdot \mathbf{x} + \omega_{ijl} t) \quad (1)$$

where N is the number of points in x , y and z direction, \mathbf{a}_{ijl} and \mathbf{b}_{ijl} are decomposition coefficients corresponding to the wave vector \mathbf{k}_{ijl} , and ω_{ijl} is the unsteadiness frequency. (In this paper $\omega_{ijl} = 0$.)

2.1 Periodic KS

Unlike the classical KS where the wavenumber usually follows a geometric progression; in our case, in order to impose periodic conditions, the wave vector components are distributed arithmetically. The flow is periodic in the three directions x , y and z . Rather than having a random wave vector for each wavenumber, the wave vectors are generated as follows:

$$\mathbf{k} = \frac{2\pi}{l} \begin{pmatrix} n_1 \\ n_2 \\ n_3 \end{pmatrix} \quad (2)$$

where $(n_1, n_2, n_3) \in [1, 2, \dots, N]^3$, so that the velocity field is l -periodic along x , y and z .

The vectors a_{ijl} and b_{ijl} in equation (2) are by construction orthogonal to k_{ijl} with their amplitude chosen according to a prescribed power law energy spectrum $E(k)$. This ensures that the synthetic flow is isotropic and incompressible.

2.2 Energy spectrum

The effect of absence of sweeping and the discrepancy between KS and Richardson theory has been discussed in [16, 14]. Here our choice of discretisation for the periodic box imposes a Reynolds number small enough to discard any such effect. Furthermore, kinematic simulation has been shown to be in a good agreement with laboratory experiments for statistics of multi-particle for Kolmogorov ($-5/3$) energy spectrum (see e.g. [15, 14, 8]).

This study is limited to the steady case ($\omega_{ijl} = 0$) and we use an energy spectrum which does not change with time and has the following form:

$$E(k) = \begin{cases} Ck^{-5/3} & k_{min} < k < k_{max} \\ 0 & \text{otherwise} \end{cases} \quad (3)$$

where C is a constant. The total kinetic energy, E , is obtained by integrating the energy spectrum over the total range of wave number as:

$$E = \int_{k_{min}}^{k_{max}} E(k) dk \quad (4)$$

and the root mean square velocity, r.m.s., of the turbulent fluctuations is calculated as:

$$u' = \sqrt{\frac{2}{3} \int_{k_{min}}^{k_{max}} E(k) dk} \quad (5)$$

The integral length scale of the isotropic turbulence is defined as follows:

$$L = \frac{3\pi \int_{k_{min}}^{k_{max}} k^{-1} E(k) dk}{4 \int_{k_{min}}^{k_{max}} E(k) dk} \quad (6)$$

The Kolmogorov length scale is defined as $\eta = 2\pi/k_{max}$. The ratio between the integral and Kolmogorov length scale is $L/\eta = k_{max}/k_{min}$ which is used to determine the inertial range and the associated Reynolds number: $Re = (L/\eta)^{4/3} = (k_{max}/k_{min})^{4/3}$.

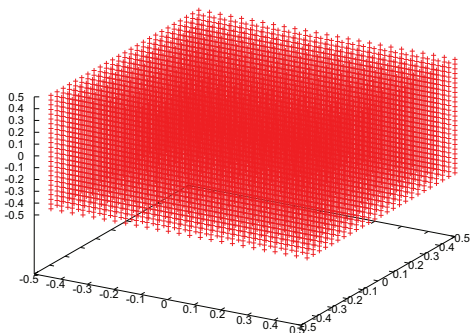


Figure 1: Initial distribution of particles ($t = 0$)

3 Equation of motion of inertial particle

The simplified equations we use for the motion of heavy particles was derived by [9, 7] to study the motion in two phase flows in turbulent flows. The equation for the particle's velocity \mathbf{V} is:

$$\frac{d\mathbf{V}}{dt} = \frac{\mathbf{u} - \mathbf{V} + \mathbf{V}_d}{\tau_a} \quad (7)$$

where τ_a is the aerodynamics response time and $\mathbf{V}_d = \tau_a \mathbf{g}$ the Stokes terminal fall velocity in still fluid or particle drift velocity. For the sake of convenience we introduce two non-dimensional parameters, the drift parameter defined as the ratio of the particle's drift velocity to the turbulence velocity fluctuation rms value u' :

$$\gamma = V_d/u' = \tau_a g/u' \quad (8)$$

and the Stokes number defined as the ratio of the particle's inertial time to the turbulence characteristic time:

$$St = \tau_a u'/L \quad (9)$$

where L is the turbulence integral length-scale.

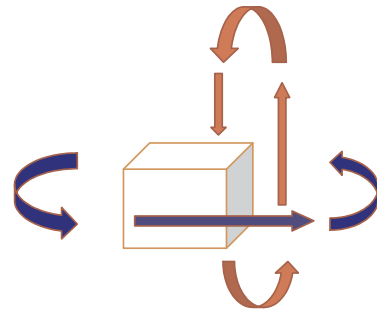


Figure 2: Initial distribution of particles ($t = 0$)

3.1 Particles' tracking

In order to understand better the structure of the KS field and particularly its property in terms of particles' clustering we release particles from a regular spatial distribution as shown in figure 1. The particles are then left to evolve according to equation (7). Whenever a particle leaves the box it is re-injected in agreement with the periodic pattern as illustrated in figure 2.

The cloud of particles is then left to evolve for a time long enough for it to reach its asymptotic state. By asymptotic state we mean that the particles settle in a particular region of the periodic box. That asymptotic region, if it exists, can be thought of as a Lagrangian attractor. This is where the particles will eventually go in our KS. This 'attractor' is different from the classical approach of [2] which is done in phase space. The evolution of the laden particles is studied for different pairs of Stokes numbers and drift parameters.

First the cloud will evolve through a transition phase until it reaches its asymptotic shape. So it is important to allow for enough time for the particles to reach the Lagrangian attractor.

The evolution of the particles cloud in the turbulent flow

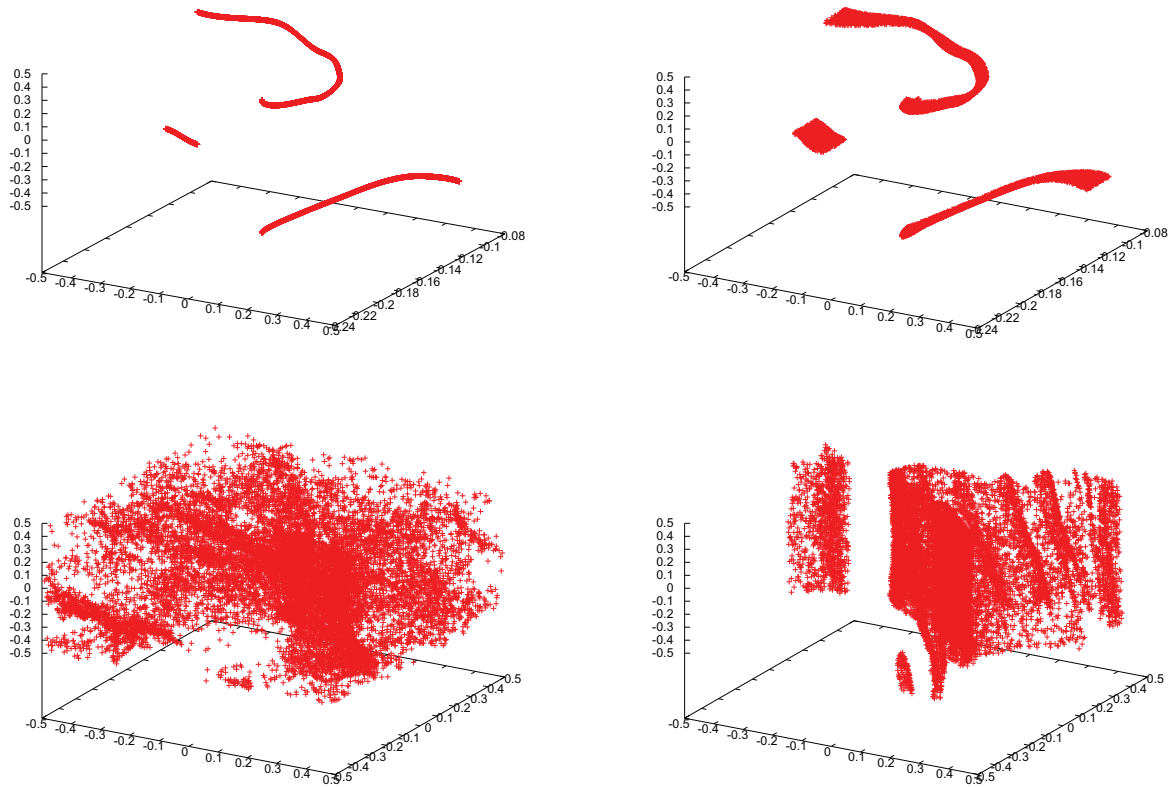


Figure 3: Evolution of the particles cloud for $St = 0.413$ and a) $\gamma = 0.586$, b) $\gamma = 0.598$, c) $\gamma = 0.689$, d) $\gamma = 5.745$

is studied for different pairs of Stokes numbers and drift parameters. For the present work the unsteadiness frequency is set to zero and energy spectrum of the flow field is also kept constant (non decaying turbulence). This frees us from any issue about forcing.

4 Results

We plot the particle positions as in figure 3, we identify tree main cases for the Lagrangian attractor shape:

- i) one-dimensional structure,
- ii) two-dimensional structure,
- iii) no particular shape.

Case i) is illustrated in figure 3a. Case ii) is typically obtained from i) when the gravity effect is important, it is illustrated in figure 3d. In many cases intermediary shapes are observed, in-between one-dimensional and two-dimensional, leading eventually to case iii).

In a systematic approach we divide the study into two main cases:

- i) the Stokes number is kept constant while the drift parameter is varied (§ 4.1);
- ii) the drift parameter is kept constant while the Stokes number is altered (§ 4.2).

4.1 Effect of the variation of the drift parameter at constant Stokes number

A typical case is shown in figure 3 for $St = 0.413$ and $\gamma = 0.586$ (a), 0.598 (b), 0.689 (c), 5.745 (d).

For the case we chose, we can observe a one-dimensional structure (figure 3a) when the effect of gravity is small. Keeping the Stokes number constant and increasing the drift parameter, that is the gravity effect, it can be noticed that the one-dimensional pattern thickens as shown in figure 3b, leading to a ribbon-like shape. Further increase in the drift parameter will change further the topology of the particles clustering pattern reaching eventually a two-dimensional structure. This two-dimensional structure is clearly obtained by thickening the cloud in the vertical direction as can be seen in figure 3d. The one-dimensional structure which forms the basis of that two-dimensional layer seems to be dependent on the pair Stokes number/drift parameter as it is different in figure 3b and figure 3d.

This change from one-dimensional to two-dimensional is quite sudden as the beginning of the process can be clearly identified in figure 3b where the drift parameter has just been increased by 2%.

However, The increase of the drift parameter should not be thought of as only increasing the topological complexity of the Lagrangian attractor and improving particle mixing or preventing particle clustering. The case presented in figure 3c and d corresponds to the same Stokes number as figure 3 a and b but this time increasing the drift parameter (from 0.689 to 5.745) leads to a simpler two-dimensional layered structure.

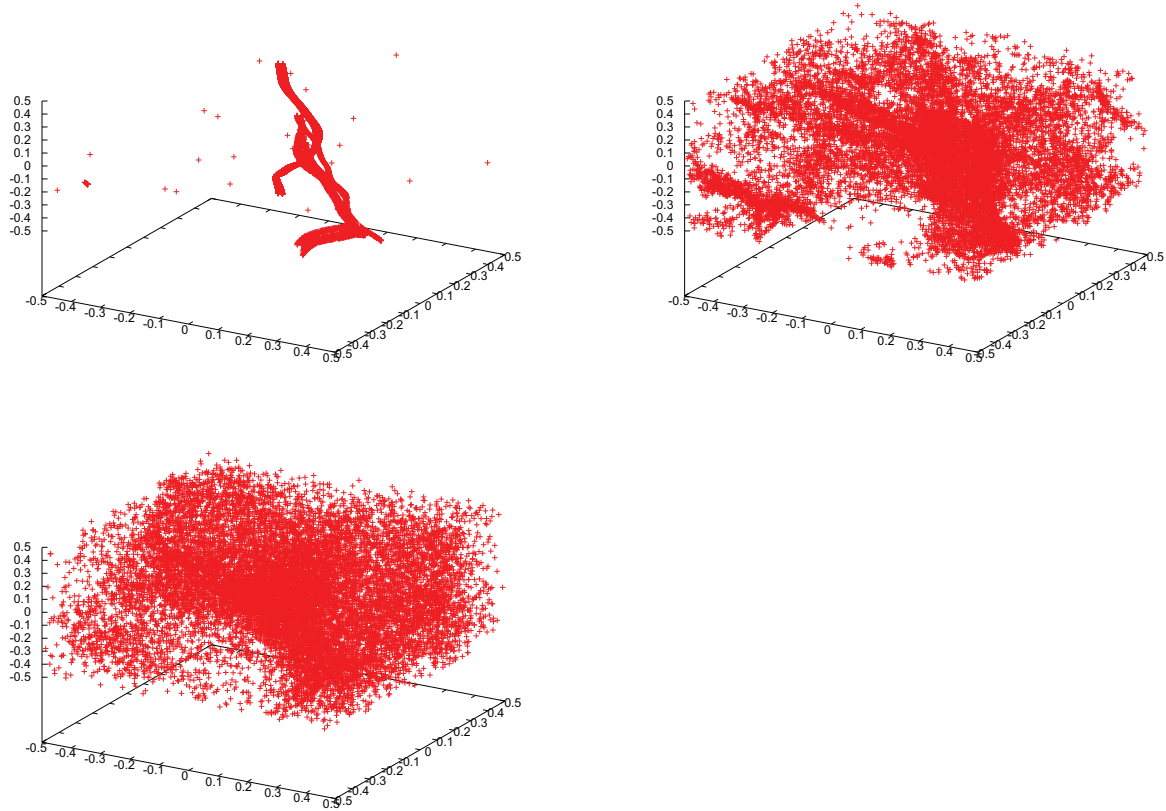


Figure 4: Pattern of particle cluster with $\gamma = 0.689$ and a) $St = 0.207$ b) $St = 0.413$ c) $St = 1.693$

4.2 Effect of Stokes number on particle clustering keeping drift parameter constant

We can also look at the cloud evolution from the opposite perspective that is keeping this time the drift parameter constant and changing the Stokes parameter. Clustering patterns of laden particles with different Stokes numbers are shown in figure 4 for $\gamma = 0.689$ and $St = 0.207$ (a), $St = 0.413$ (b), $St = 1.693$ (c).

In a similar way to the previous study we found that the topology of the particle cluster changes with the Stokes number. We start from the one-dimensional Lagrangian attractor, figure 4a, and then increase the Stokes number. Increasing the Stokes number clearly destroys the one-dimensional structure: the particles are more scattered in figure 4b though they still tend to concentrate along one dimensional curves. Increasing further the Stokes number completely inhibits the one-dimensional structure as can be seen in figure 4c.

5 Conclusion

In this study we tried to identify the preferential regions of agglomeration of laden particles in a periodic Kinematic Simulation box. From these preliminary results, we can conclude that the patterns of the inertial particles clustering in the turbulent flow are strongly dependent on the combination of Stokes number and drift parameter. Depending on the values of these parameters, the particles can cluster on a geometry that can be clearly one-dimensional, two-dimensional, or has no well-defined integer dimension.

For relatively small values of γ and St , the cluster's pattern remains one dimensional. There is a value of St beyond which the cluster is not one dimensional anymore even at small values of γ . This is consistent with the results in [12] where the clouds was not one-dimensional but reaches an asymptotic fractal dimension for fluid particles.

Further increases in γ and St change the one-dimensional structure into a 'thickening' curve; leading first to a two-dimensional pattern. There is a range for γ and St for which particle clusters have no integer dimension.

In this contribution, we presented only qualitative results. Eventually, the aim of all this work is to quantify the values of γ and St for laden particles associated to a particular type of Lagrangian attractors. We will need to develop a more refined characterisation of the attractor structure by using fractal dimension.

Because of its easiness of implementation and low computing cost Kinematic Simulation allows for systematic parametric studies. To understand better the particularity of the KS synthetic Eulerian fields the results need comparison with other validated numerical simulation techniques like Direct Numerical Simulation. Then we hope to be able to relate our approach to the more fundamental work of [2] and beyond to the spectrum properties [10].

References

- [1] Abou-El-Azm, A., Nicolleau, F.: Dispersion of heavy particle sets in an isotropic turbulence using

- kinematic simulation. *Phys. Rev. E* **78**(1), 0616,310 (2008). Doi:10.1103/PhysRevE.78.016310
- [2] Bec, J.: Fractal clustering of inertial particles in random flows. *Phys. Fluids* **15**(11), 81–84 (2003)
- [3] Chen, L., Goto, S., Vassilicos, J.: Turbulent clustering of stagnation points and inertial particles. *J. Fluid Mech.* **553**, 143–154 (2006)
- [4] Eaton, J., Fessler, J.: Preferential concentration of particle by turbulence. *Int. J. Multiphase flow* **20**, 169 (1994)
- [5] Fung, J., Hunt, J., Malik, N., Perkins, R.: Kinematic simulation of homogeneous turbulence by unsteady random fourier modes. *J. Fluid Mech.* **236**, 281–317 (1992)
- [6] Fung, J., Vassilicos, J.: Inertial particle segregation by turbulence. *Phys. Rev. E* **68**, 046,309 (2003)
- [7] Gatignol, R.: The faxen formulae for a rigid particle in an unsteady non-uniform stokes flow. *J. Mech. Theor. Appl.* **1**(2), 143–160 (1983)
- [8] Khan, M., Pumir, A., Vassilicos, J.C.: Kinematic simulation of turbulent dispersion of triangles. *Phys. Rev. E* **68**, 026,313 (2003)
- [9] Maxey, M.R., Riley, J.J.: Equation of motion for a small rigid in a nonuniform flow. *Physics of Fluids* **26**(4), 883–889 (1983)
- [10] Michelitsch, T., Maugin, G., Nicolleau, F., Nowakowski, A., Derogar, S.: Dispersion relations and wave operators in self-similar quasi-continuous linear chains. *Phys. Rev. E* **80**, 011,135 (2009). Doi:10.1103/PhysRevE.80.011135
- [11] Nicolleau, F., Cambon, C., Redondo, J.M., Vassilicos, J., Reeks, M., Nowakowski, A. (eds.): New approaches in modelling multiphase flows and dispersion in turbulence, fractal methods and synthetic turbulence, *Ercoftac Series*, vol. 18. Springer Science (2011). Doi: 10.1007/978-94-007-2506-5
- [12] Nicolleau, F., ElMaihy, A.: Study of the development of a 3-d material surface and an iso-concentration field using ks. *J. Fluid Mech.* **517**, 229–249 (2004). Doi: 10.1017/S0022112004000898
- [13] Nicolleau, F., ElMaihy, A.: Study of the effect of the reynolds number on three- and four-particle diffusion in three-dimensional turbulence using kinematic simulation. *Phys Rev. E* **74**(4), 046,302 (2006). Doi:10.1103/PhysRevE.74.046302
- [14] Nicolleau, F., Nowakowski, A.: Presence of a richardson’s regime in kinematic simulations. *Phys. Rev. E* **83**, 056,317 (2011). Doi: 10.1103/PhysRevE.83.056317
- [15] Nicolleau, F., Vassilicos, J.: Turbulent pair diffusion. *Phys. Rev. Letters* **90**(2), 024,503 (2003). Doi: 10.1103/PhysRevLett.90.024503
- [16] Thomson, D.J., Devenish, B.J.: Particle pair separation in kinematic simulations. *J. Fluid Mech.* **526**, 277–302 (2005)

ON THE COMPLEX MOTION OF INERTIAL PARTICLES NEAR UNSTEADY VORTICES

J. R. Angilella, T. Nizkaya and M. Bués

Nancy-Université, LAEGO, rue du Doyen Roubault, 54501 Vandœuvre-les-Nancy, France

Abstract

Some recent researches about the motion of heavy inertial particles in two-dimensional vortical flows are reviewed. The occurrence of chaotic particle trajectories is discussed in the case where the flow is unsteady. Particle trapping by either points or limit-cycles is also analysed. When both chaotic motion and trapping (by different attractors) exist, inertial particles can have fractal basin boundaries, leading to an unpredictable final destination.

1 Introduction

The motion of inertial particles in fluid flows is known to be very complex in most cases, even if the flow is laminar and unaffected by the particle loading. Though the chaotic advection of inertia-free particles has been widely investigated in the last decades (see for example the review paper by Aref [1]), the complex behaviour of inertial particles is much less understood (Cartwright *et al.* [2]). Various mechanisms can cause complex particle trajectories, like collisions or wake effects. For isolated low-Reynolds number particles these effects are absent, and the main cause of complexity is the spatial dependence of the fluid velocity, which induces a changing hydrodynamic force along the particle trajectory. If, in addition, the particle response time is much smaller than flow time scales (small Stokes number limit), then the velocity of the inclusion is always close to the local fluid velocity, but this does not imply fluid-like lagrangian dynamics. Indeed, even if the slip velocity is small, the particle position can significantly differ from fluid point trajectories. Such particles can be observed to have a chaotic motion within a chaotic flow (i.e. a laminar flow with chaotic fluid points trajectories) [3]. Of course, chaotic particle motion within non-chaotic flows is widely met too [4]. Also, because the dynamics of inertial particles is dissipative, in contrast with fluid point dynamics in incompressible flows, one often observe that these objects converge towards well-defined zones of the flow domain [5].

This accumulation can sometime be surprising, like in vortical flows where heavy particles are generally centrifuged away from the vicinity of vortices. For example, asymptotically stable equilibrium positions have been found for heavy particles in a Burger vortex [6], where the inward drag due to the axial stretching flow balances the centrifugal force. Stable attracting equilibrium points have also been found for low-Re aerosols in isolated co-rotating point vortex pairs [7]. These attracting points are fixed in the reference frame rotating with the vortex pair, and correspond to an equilibrium between the inward drag and the centrifugal force. They have been shown to persist if vortices have different (non-opposite) strengths [8], and also if the vortices move due to the presence of a wall [9][10]. All these trapping points

exist until the particle Stokes number exceeds some critical value.

Attractors in the form of limit-cycles can also be found in inertial particle dynamics. For heavy particles, such limit cycles have been observed in two-dimensional cellular flows [11] [5], but also in counter-rotating point vortices [8]. The criterion proposed recently by Haller & Sapsis [12] is of great interest for the identification of such limit cycles.

In the following sections, the complex motion of heavy inertial particles in two simple and widely met potential flow structures are discussed. The typical behaviours presented in this introduction, namely chaotic motion and trapping, will be illustrated. Some arguments suggesting the existence of fractal basin boundaries will be given.

2 Chaotic particle motion

We have investigated the sedimentation of heavy inertial low-Re particles (e.g. aerosols) in the vicinity of a horizontal fixed vortex (Fig. 1(a)). This is a classical configuration which has already been used in the past to analyse particles in turbulence [13]. The hydrodynamic force acting on the inclusions has been taken to be a simple Stokes drag, together with the gravity force. If the terminal particle velocity is of the order of the flow velocity, and if the vortex intensity is time-periodic (due to some external forcing), then one can check that particle trajectories can be chaotic, as sketched in Fig. 1(a). This chaos is due to the combined effect of differential rotation, which stretches particle clouds, and of gravity, which makes particle clouds drift downward when the vortex weakens. A stretch-and-fold mechanism is therefore at work here, leading to chaotic motion. Because gravity plays a key role here, as the vertical drift prepares the cloud to being folded when the vortex restarts, this sequence has been called "stretch-sediment-and-fold". Clearly, this happens only under appropriate conditions involving the particle properties (terminal velocity, Stokes number St) and the flow time scales. These conditions have been derived [14], in the limit $St \ll 1$, by writing that the particle velocity is equal to the local fluid velocity plus the terminal velocity, plus perturbations due to the fluid acceleration. This, very classical, approach allowed us to write the particle dynamics as a perturbed hamiltonian system, the phase portrait of which is shown, to leading order, in Fig. 2(a). It corresponds to sedimenting inertia-free particles and contains a homoclinic cycle (solid line) attached to a hyperbolic point H where the terminal velocity balances the upward fluid velocity. When the system is perturbed, due to both the particle inertia and the flow unsteadiness, a homoclinic bifurcation can occur and a stochastic zone appears in the vicinity of the homoclinic cycle. Particles sedimenting in the vicinity of the cycle are therefore mixed temporarily within the stochastic zone.

3 Particle trapping

When two point vortices are present (Fig. 1(b)), the flow is unsteady due to the mutual interaction of the vortices. If the total strength is non-zero, vortices rotate at constant speed around their centre of vorticity and the flow observed in the rotating frame is steady. Relative streamlines are sketched, in the case of two identical vortices, in Fig. 2(b). As discussed in the introduction, one can check that heavy inertial particles, in the absence of gravity, can have various equilibrium positions in the rotating frame, where the (inward) drag balances the (outward) centrifugal force. In the case of identical vortices, two equilibrium positions are asymptotically stable: they attract inertial particles (see points P and P' of Fig. 2(b)). The corresponding basins of attraction are smooth and separated [7].

Particles advected in this flow can therefore pack in the vicinity of P and P', and rotate as a solid-body with the vortex pair (they are kept fixed in the rotating frame). These equilibrium points can therefore be denoted as "hydrodynamic Lagrange points", even though they correspond to dissipative dynamics. They have been shown to be rather robust, in that they persist (i) if vortices have different strengths [8], (ii) if gravity is present [10], (iii) if the vortex pair moves away because of a wall [9].

In case (i) the full trapping diagram has been obtained [8], and one observe that one or two trapping points always exist, provided the vortex strength ratio differs from -1 and the particle Stokes number is small enough. Any vortex pair can therefore behave as a dust trap, provided vortices live long enough and do not have opposite strengths. In cases (ii) and (iii) the trapping points are no longer fixed in the rotating frame, and move periodically.

Finally, trapping points have been shown to exist *temporarily* if viscosity is taken into account [7]. In this case vortices eventually merge after a few turnovers. However, if the flow Reynolds number is large enough, direct numerical simulations show that heavy inertial particles accumulate near the theoretical points P and P', and are eventually centrifuged away when vortex coalescence occurs.

4 Particle trapping and fractal basin boundaries

When the two point vortices interact in the vicinity of a wall (modelled as a symmetry line in inviscid fluids), one can easily check that the rotation of the vortices (with non-opposite strengths) is no longer steady. In addition, the distance between them is no longer constant. If the wall is far enough, the distance between vortices is periodic, with period half the wall-free rotation period [15]: the wall therefore induces a natural oscillation of the vortices, like in Ref. [16]. This unsteadiness will affect the particle dynamics even though, as noticed above, the trapping points P and P' will persist. Indeed, the homoclinic cycles in the leading-order (i.e. inertia-free) particle dynamics (Fig. 2(b)), will break, due to the natural unsteady forcing induced by the wall. A stochastic zone will therefore exist in the vicinity of these cycles, and particles might wander there and mix.

Particles exiting the stochastic zone will therefore be either centrifuged away, or trapped by P or P'. Because of the strong chaotic mixing occurring in the stochastic zone, the basins of attraction of P and P' will no longer be separated: we expect them to have a fractal bound-

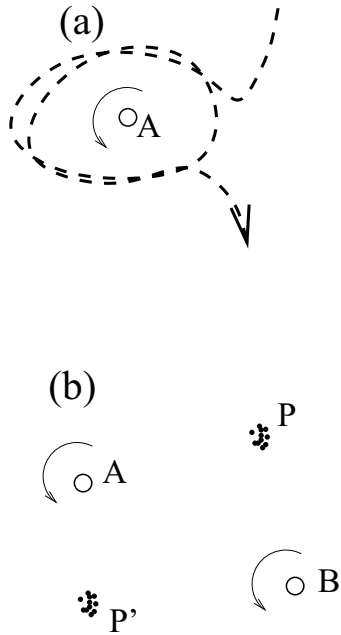


Figure 1: Sketches of the flow configurations considered in this paper: fixed unsteady horizontal vortex (a), vortex pair (b). Solid lines are streamlines, dashed lines are particle trajectories. Points A and B are the vortex centres, P and P' are trapping points

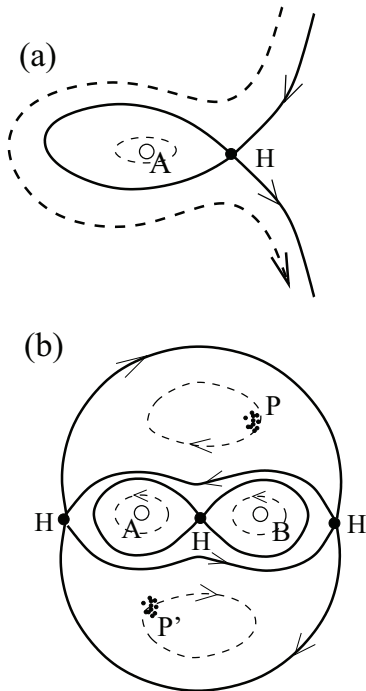


Figure 2: Sketches of the leading-order particle phase portraits in the flows (a) and (b) of Fig. 1. Hyperbolic saddle-points are indicated with an H, solid lines are homoclinic cycles

ary. This means that for all scale λ (below the typical vortex size and above the particle radius), the probability of having two particles, with an initial separation λ , trapped by different attractors is non-zero. Computations of this uncertainty probability are currently in progress (in collaboration with A. Motter (Northwestern University) and R. Vilela (Federal University of Sao Paulo)), and should confirm this point.

5 Conclusion

Even though the flows discussed in this paper are very specific, we believe that the behaviours of inertial particles described here can be met in various contexts. The stretch-sediment-and-fold mechanism (section 2) is based on the finite terminal velocity of the inclusions, and on the unsteady differential rotation: it does not depend on the detailed shape of the rotating flow. Trapping points (section 3) are a very interesting topic, especially if particles are heavy. Note that, because the spatial coordinates of trapping points depend on the Stokes number, particles with different physical properties will converge towards different attracting points, provided their Stokes number is below some critical value. Trapping therefore induces separation.

The application of these various elementary situations to turbulent flows must be done with care, as turbulence cannot be reduced to interacting vortices. Note however that, in two dimensional rotating turbulence, anticyclonic pairing occurs repeatedly, leading to large anticyclonic structures. These structures can trap particles, under certain conditions, because the Coriolis force (due to the frame rotation) drives particles towards the vortex cores [17]. This suggests that particles trapped temporarily by attracting points, during vortex pairing, might then drift to the centre of the resulting vortex when coalescence is complete. Repeated vortex pairings and dust capture could therefore be a mechanism of interest for particle-laden two-dimensional rotating turbulence.

References

- [1] H. AREF. The development of chaotic advection. *Phys. Fluids*, 14(4):1315–1325, 2002.
- [2] J. CARTWRIGHT, U. FEUDEL, G. KAROLYI, A. DE MOURA, O. PIRO, and T. TEL. Dynamics of finite-size particles in chaotic fluid flows. pages 51–87, 2010. *Non-linear Dynamics and Chaos: Advances and Perspectives*. THIEL, M. Ed. Springer-Verlag Berlin Heidelberg.
- [3] J.B. MACLAUGHLIN. Particle size effects on lagrangian turbulence. *Phys. Fluids*, 31(9):2544–2553, 1988.
- [4] O.A. DRUZHININ, L.A. OSTROVSKY, and Y. A. STEPANYANTS. Dynamics of particles in the steady flows of an inviscid fluid. *CHAOS*, 3(3):359–367, 1993.
- [5] M. R. MAXEY. The motion of small spherical particles in a cellular flow field. *Phys. Fluids*, 30:1915–1928, 1987.
- [6] E. MARCU, B. MEIBURG and P.K. NEWTON. Dynamics of heavy particles in a Burgers vortex. *Phys. Fluids*, 7(2):400–410, February 1995.
- [7] J. R. ANGILELLA. Dust trapping in vortex pairs. *Physica D: Nonlinear Phenomena*, 239:1789–1797, 2010.
- [8] T. NIZKAYA, J. R. ANGILELLA, and M. BUES. Note on dust trapping in vortex pairs with unequal strengths. *Phys. Fluids*, 22:113301, 2010.
- [9] R.D. VILELA and A. E. MOTTER. Can aerosols be trapped in open flows ? *Phys. Rev. Let.*, 99(264101), 2007.
- [10] R. H. A. IJZERMANS and R. HAGMEIJER. Accumulation of heavy particles in N-vortex flow on a disk. *Phys. Fluids*, 18:063601, 2006.
- [11] M. R. MAXEY and S. CORRSIN. Gravitational settling of aerosol particles in randomly oriented cellular flow fields. *J. Atmos. Sci.*, 43(11):1112–1134, 1986.
- [12] T. SAPSIS and G. HALLER. Clustering criterion for inertial particles in 2d time-periodic and 3d steady flows., *Chaos*, 20:017515, 2010.
- [13] J. DAVILA and J. HUNT. Settling of small particles near vortices and in turbulence. *J. Fluid Mech.*, 440:117–145, 2001.
- [14] J. R. ANGILELLA. Chaotic particle sedimentation in a rotating flow with time-periodic strength. *Phys. Rev. E*, 78(16):066310, 2008.
- [15] J. R. ANGILELLA. Asymptotic properties of wall-induced chaotic mixing in point vortex pairs. *Phys. Fluids*, 2011. In press.
- [16] A. WONHAS and VASSILICOS. Mixing in frozen and time-periodic two-dimensional vortical flows. *J. Fluid Mech.*, 442:359–385, 2001.
- [17] P. TANGA, A. BABIANO, and A. DUBRULLE, B. PROVENZALE. Forming planetesimals in vortices. *Icarus*, 121:158–170, 1996.

APPLICATIONS OF SYNTHETIC TURBULENCE TO FILAMENT MODELS OF MAGNETIC FLUX ROPES AND QUANTUM TURBULENCE

A. Baggaley

*School of Mathematics and Statistics, Newcastle University
Newcastle, NE21 4FL, United Kingdom*

Abstract

We consider two separate systems, the magnetic field generated by the turbulent flow of a rarefied plasma, and quantum turbulence in superfluid helium. In both systems either the magnetic field or the vorticity field are confined to thin filaments; we model these numerically as discretised lines. To appropriately model either system we must supplement the filament model with a turbulent flow field. In order to reduce the complexity of the numerical model we make use of ‘synthetic’ turbulence models, using the so-called Kinematic Simulations (KS) model; a summation of random Fourier modes. We shall show that observational and experimental results can be reproduced using the filament approach, in combination with the KS flow field.

1 Introduction

The evolution of magnetic field \mathbf{B} , embedded in a flow at a velocity \mathbf{u} is governed by the induction equation,

$$\frac{\partial \mathbf{B}}{\partial t} = \nabla \times (\mathbf{u} \times \mathbf{B}) + \eta \nabla^2 \mathbf{B}, \quad (1)$$

if the magnetic diffusivity, η , is constant. The equation for the evolution of the fluid vorticity, $\boldsymbol{\omega} = \nabla \times \mathbf{u}$, takes a similar form,

$$\frac{\partial \boldsymbol{\omega}}{\partial t} = \nabla \times (\mathbf{u} \times \boldsymbol{\omega}) + \nu \nabla^2 \boldsymbol{\omega}, \quad (2)$$

where ν is the kinematic viscosity. Whilst the similarity is striking, vorticity is functionally related to the velocity field, whereas the magnetic field is not.

In rarefied plasmas, such as the Solar corona, hot gas in spiral and elliptical galaxies, galactic and accretion disc halos there is strong observational evidence that the magnetic field is confined to thin filaments or flux tubes [1, 2]. It is interesting to note that these are some of the highest temperatures in the universe. At the opposite end of the temperature scale, close to absolute zero, helium-4 enters the superfluid (inviscid) phase through Bose-Einstein condensation. Due to quantum mechanical constraints in a superfluid vorticity is constrained to thin quantised vortices with a fixed size and strength [3].

Both these systems are therefore ideal candidates for numerical modelling using filament methods. If we can assume that the average radius of curvature is much larger than the filaments core size, then we can approximate the filaments as three dimensional space curves. Numerically these can be represented as a collection of N oriented points. In both systems we can readily define appropriate evolution equations for these filaments,

however before doing so we shall describe the basic algorithms of the filament model.

2 Filament models

We represent the set of filaments in our system as space curves $\mathbf{s} = \mathbf{s}(\xi, t)$ of infinitesimal thickness, where t is the time and ξ is arc length. The filaments are numerically discretised to leave a set of N oriented points. We can readily define numerical approximations to spatial derivatives along the filaments. Let \mathbf{s}_i be the i^{th} point on the filament; the points behind and in front have positions \mathbf{s}_{i-1} and \mathbf{s}_{i+1} respectively. We denote $\ell_i = |\mathbf{s}_i - \mathbf{s}_{i-1}|$, $\ell_{i+1} = |\mathbf{s}_{i+1} - \mathbf{s}_i|$, hence:

$$\mathbf{s}'_i = \frac{\ell_i \mathbf{s}_{i+1} + (\ell_{i+1} - \ell_i) \mathbf{s}_i + \ell_i \mathbf{s}_{i-1}}{2\ell_{i+1} \ell_i} + (O)(\ell^2) \quad (3)$$

$$\mathbf{s}''_i = \frac{2\mathbf{s}_{i+1}}{\ell_{i+1}(\ell_{i+1} + \ell_i)} - \frac{2\mathbf{s}_i}{\ell_{i+1} \ell_i} + \frac{2\mathbf{s}_{i-1}}{\ell_i(\ell_{i+1} + \ell_i)} + (O)(\ell^2) \quad (4)$$

In section 4 we define the appropriate velocity fields for the filaments. Here we shall assume that the filaments move with a velocity $\mathbf{u}(\mathbf{s}, t)$. In order to numerically time-step the filaments we use a 3rd order Adams–Bashforth scheme. Given an evolution equation, for the i^{th} point, of the form $d\mathbf{s}_i/dt = \mathbf{u}_i$, the recursion formula is

$$\mathbf{s}_i^{n+1} = \mathbf{s}_i^n + \frac{\Delta t}{12} (23\mathbf{u}_i^n - 16\mathbf{u}_i^{n-1} + 5\mathbf{u}_i^{n-2}) + \mathcal{O}(\Delta t^4). \quad (5)$$

where Δt is the time-step and the superscript n refers to the time $t_n = n\Delta t$ ($n = 0, 1, 2, \dots$). Lower order schemes are used for the initial steps of the calculations, when older velocity values are not available.

As the points along the filament move, the separation between neighbours along the same filament is not constant. In general this is not a problem, we have defined finite-difference schemes which work with an adaptive mesh size. However the distance between points sets the resolution of the calculation, therefore we must set some upper-bound on the distance between points before we re-mesh the filaments through the introduction of new points. Our criterion is the following: if the separation between two points, \mathbf{s}_i and \mathbf{s}_{i+1} , becomes greater than some threshold quantity δ (which we call the minimum resolution), we introduce a new point at position $\mathbf{s}_{i'}$ given by

$$\mathbf{s}_{i'} = \frac{1}{2}(\mathbf{s}_i + \mathbf{s}_{i+1}) + \left(\sqrt{R_{i'}^2 - \frac{1}{4}\ell_{i+1}^2} - R_{i'} \right) \frac{\mathbf{s}''_{i'}}{|\mathbf{s}''_{i'}|}, \quad (6)$$

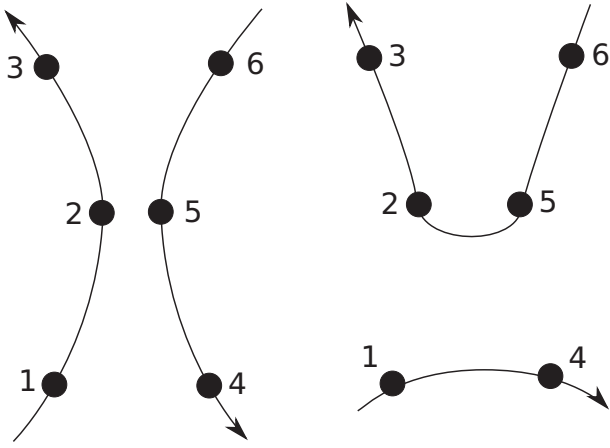


Figure 1: A schematic of the reconnection procedure used in the filament model

where $R_{i'} = |\mathbf{s}_{i'}''|^{-1}$. In this way $\mathbf{s}_{i'}'' = (\mathbf{s}_i'' + \mathbf{s}_{i+1}'')/2$, that is to say the insertion of new points preserves the curvature. Our procedure is thus superior to simpler linear interpolation.

Conversely, points along the filament are removed if their separation becomes less than $\delta/2$, ensuring that the shortest length-scale of the calculation remains fixed. Importantly the vector fields in both systems are divergence free, $\nabla \cdot \mathbf{B} = \nabla \cdot \boldsymbol{\omega} = 0$. The model maintains this constraint the filaments in our system must always form closed loops.

Periodic boundary conditions are readily enforced by re-inserting points, which leave a periodic cube, on the opposite side. So-called ‘ghost’ particles can be used to simplify the algorithms for calculating spatial derivatives.

3 Reconnections

Both systems that we shall consider are highly turbulent, therefore we must pay particular attention to energy dissipation. In rarefied plasmas an important (if not dominant) mechanism for the dissipation of magnetic energy is the reconnection of magnetic lines rather than magnetic diffusion [4]. Magnetic reconnection is usually modelled with the induction equation (perhaps including the Hall current), and magnetic dissipation is enhanced due to the development of small-scale motions and magnetic fields. This approach may or may not apply to magnetic fields concentrated into flux ropes, where magnetic energy losses are strongly reduced at large scales and, hence, more energy can be deposited at the smaller scale of order the tube radius, where reconnections occur. By modelling the magnetic field in the thin filament approach we explore this possibility.

We know from experiments [5] and from more microscopic models [6] that superfluid vortex lines can reconnect with each other when they come sufficiently close, as envisaged by Feynman [7]. Superfluid vortex reconnections do not violate Kelvin’s theorem as near the axis of the vortex core, where density and pressure vanish and velocity diverges, the governing Gross-Pitaevski equation (GPE) differs from the classical Euler equation.

Reconnections, which provide both a dissipation mechanism as well as topological changes to the filaments, are not a natural solution to our model. Hence we model reconnection events algorithmically in the following way.

If two discretisation points, which are not neighbours, become closer to each other than the local discretisation distance, a numerical algorithm reconnects the two filaments by simply switching flags for the points in front and behind the filament, subject to the criterion that the total length decreases. As in both systems we can use line length as a proxy for the energy of the system, this criterion ensures reconnection events are dissipative. A schematic of the reconnection procedure is shown in Fig. 1.

Self-reconnections (which can arise if a filament has twisted and coiled by a large amount) are treated in the same way. Finally in both systems parallel filaments are not able to reconnect. Therefore prior to reconnection we form local (unit) tangent vectors \mathbf{s}' , and, using the inner product, we check that the two filaments are not parallel.

4 Evolution equations

4.1 Frozen flux

The magnetic flux, Ψ , through a surface \mathbf{S} moving with the fluid, is defined as

$$\Psi = \int_{\mathbf{S}} \mathbf{B} \cdot d\mathbf{S}. \quad (7)$$

In the limit of zero magnetic diffusivity Ψ is a conserved quantity. Hence fluid motion along the magnetic field lines do not change the field, but motions transverse to the field carry the field with them. The magnetic field is said to be ‘frozen in’, and a magnetic flux tube will simply be advected by the flow. Thus at a the i^{th} point on the magnetic filament the evolution equation is simply written,

$$\frac{d\mathbf{s}_i}{dt} = \mathbf{u}_p(\mathbf{s}_i, t). \quad (8)$$

Here \mathbf{u}_p is the velocity field of the electrically conducting fluid the field is embedded in. In this work we shall use a synthetic model of turbulence, introduced in section 5, to act as the velocity field of a turbulent plasma.

Each particle is also assigned a flag B for the strength of magnetic field at that point on the loop. Assuming magnetic flux conservation and incompressibility, magnetic field strength in the flux tube is proportional to its length. Magnetic field is initially constant at all points, $B = B_0$. When a new particle is introduced, the magnetic field strength is doubled at the points involved. Likewise as points are removed, due to local contraction the magnetic field strength is halved. We have verified that this prescription reproduces accurately an exact solution of the induction equation for a simple shear flow [8].

4.2 Quantised vortex dynamics

We consider a system of liquid helium. At zero temperature the systems is purely superfluid, and as discussed earlier, vorticity is confined to thin vortex filaments. The evolution of the quantised vortex filament (at the point \mathbf{s}) is given by the Biot-Savart law

$$\frac{d\mathbf{s}}{dt} = -\frac{\Gamma}{4\pi} \oint_{\mathcal{L}} \frac{(\mathbf{s} - \mathbf{r})}{|\mathbf{s} - \mathbf{r}|^3} \times d\mathbf{r}. \quad (9)$$

The line integral extends over the entire vortex configuration \mathcal{L} . The singularity at $\mathbf{s} = \mathbf{r}$ is removed in a

standard way by considering local and non-local contributions to the integral. If \mathbf{s}_i is the position of the i^{th} discretisation point along the vortex line, Eq. 9 becomes [9]

$$\frac{d\mathbf{s}_i}{dt} = \frac{\Gamma}{4\pi} \ln \left(\frac{\sqrt{\ell_i \ell_{i+1}}}{a} \right) \mathbf{s}'_i \times \mathbf{s}''_i - \frac{\Gamma}{4\pi} \oint_{\mathcal{L}'} \frac{(\mathbf{s}_i - \mathbf{r})}{|\mathbf{s}_i - \mathbf{r}|^3} \times d\mathbf{r}. \quad (10)$$

Here \mathcal{L}' is the original vortex line without the section between \mathbf{s}_{i-1} and \mathbf{s}_{i+1} . In this work we use parameters which refer to superfluid ^4He : circulation $\Gamma = 9.97 \times 10^{-4} \text{ cm}^2/\text{s}$ and vortex core radius $a_0 \approx 10^{-8} \text{ cm}$, but our results can be generalised to turbulence in low temperature $^3\text{He-B}$.

At finite temperatures superfluid helium is a two fluid system: a viscous normal fluid component coexisting with an inviscid superfluid component. The superfluid vortices interact with the thermal excitations which make up the normal fluid, introducing a mutual friction force between the two fluid components. This means that turbulence in the quantum fluid can be driven by the flow of the normal fluid or vice-versa.

The governing equation of motion of the superfluid vortex lines, at point \mathbf{s} is given by the Schwarz equation [9]

$$\frac{d\mathbf{s}}{dt} = \mathbf{u}_s + \alpha \mathbf{s}' \times (\mathbf{u}_n - \mathbf{u}_s) - \alpha' \mathbf{s}' \times [\mathbf{s}' \times (\mathbf{u}_n - \mathbf{u}_s)], \quad (11)$$

where α , α' are temperature dependent friction coefficients [10], \mathbf{u}_n is the normal fluid's velocity (modelled using KS), and the velocity \mathbf{u}_s is the velocity field the quantised vortices calculated using Eq. (10).

In both the flux rope magnetic field model, and the vortex filament method we strictly should model the turbulent fluid ($\mathbf{u}_p/\mathbf{u}_n$) using the Navier-Stokes equation. This would allow for us to introduce a coupling between the systems due to either the Lorentz force, in the case of magnetic flux tubes, or the effect of mutual friction on the normal fluid, in the quantum turbulence model. In both our systems one can offer compelling arguments as to why this coupling can effectively be ignored. If we assume that the magnetic field is weak then the Lorentz force can be assumed to be small and so neglected, this is referred to as the kinematic regime. Likewise if the temperature is relatively high, in superfluid helium, then the normal fluid is the dominant component in the two fluid system. Here we prescribe a turbulent like flow which is numerically efficient to calculate.

5 KS model

We shall model both the turbulent plasma and normal fluid using the Kinematic Simulation (KS) model of a turbulent flow [11]. Here velocity at a position \mathbf{x} and time t is

$$\mathbf{u}(\mathbf{x}, t) = \sum_{n=1}^{N_{\text{KS}}} (\mathbf{A}_n \times \mathbf{k}_n \cos \phi_n + \mathbf{B}_n \times \mathbf{k}_n \sin \phi_n), \quad (12)$$

where $\phi_n = \mathbf{k}_n \cdot \mathbf{x} + \omega_n t$, N is the number of modes, \mathbf{k}_n and $\omega_n = k_n u_n$ are their wave vectors and frequencies. An advantage of using this flow is that the energy spectrum, $E(k_n)$ is controllable via appropriate choice of \mathbf{A}_n and \mathbf{B}_n . We also note that the flow is incompressible, $\nabla \cdot \mathbf{u} = 0$. In all simulations we adopt an energy spectrum

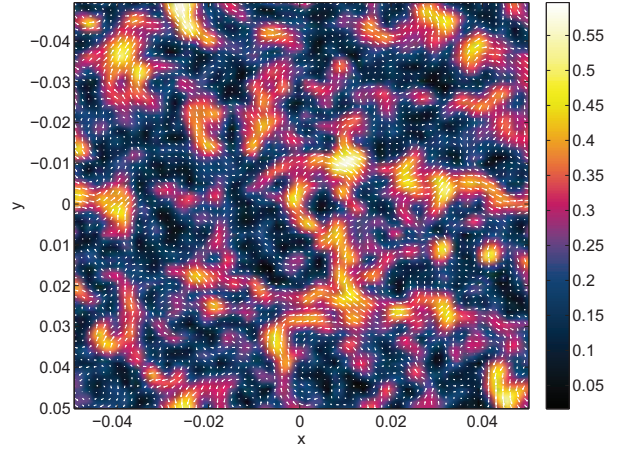


Figure 2: A slice in the xy -plane ($z = 0$) of the magnitude of the velocity (u) of the KS flow with $N_{\text{KS}} = 100$, and $\text{Re} = (k_{N_{\text{KS}}}/k_1)^{4/3} = 17.11$, with velocity vectors overlaid in white

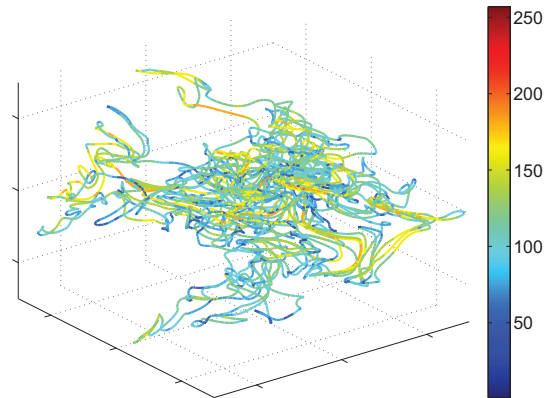


Figure 3: A typical state of the growing magnetic field in the flux rope dynamo simulations. The colour coding is according to the local magnetic field strength

which reduces to $E(k) \propto k^{-p}$ for $1 \ll k \ll k_{N_{\text{KS}}}$, with $k = 1$ at the integral scale; $p = 5/3$ produces the Kolmogorov spectrum, and $k_{N_{\text{KS}}}$ is the cut-off scale. The effective Reynolds number $\text{Re} = (k_{N_{\text{KS}}}/k_1)^{4/3}$ is defined by the condition that the dissipation time equals the eddy turnover time at $k = k_{N_{\text{KS}}}$. Finally we have adapted Eq. (12) to periodic boundary conditions by enforcing a 2π dependence in each component of the wavevector \mathbf{k} .

6 Flux Rope Dynamo

We shall now discuss the set-up and results of the filament model for the magnetic field. We initially consider a set of random loops dispersed throughout a periodic unit cube. The filaments are advected by the KS flow and we find the total filament length, a proxy for the magnetic energy, grows exponentially ($B(t) \approx B_0 \exp(\sigma t)$); as we would expect from kinematic dynamo theory [12]. In Fig. 3 we show a snapshot of the flux rope dynamo showing the tangled structure of the magnetic field. Of interest in this work is the amount of magnetic energy released in each reconnection event, and the statistics of energy release. To place the reconnection-based dynamo into a proper perspective, we compare it with a dynamo

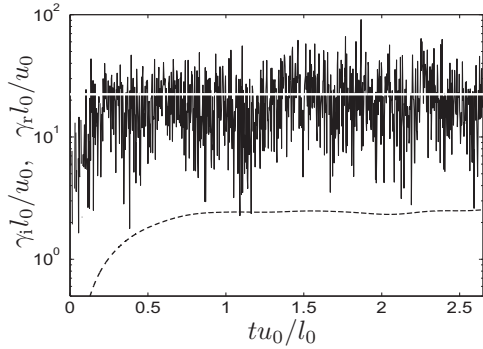


Figure 4: Magnetic energy release rates from the induction equation (dashed) and the flux rope model (solid). The former has a mean value of 2.4 (here $R_m = UL/\eta = 1200$) once the eigensolution has developed. The latter has a mean value of 23 (thick horizontal line)

obtained for the same velocity field, but by solving the induction equation, i.e. Eq. (1). In particular, we compare the rates of magnetic energy dissipation, which can be identified with the plasma heating rate. We assume that the part of the magnetic energy which drives plasma motion at a reconnection site (such as jets) is eventually dissipated into heat as well, so that we consider that the whole magnetic energy released is converted into heat. For the induction equation, the relevant quantity is

$$\gamma_i = d \ln M / dt = \int_V \eta \mathbf{B} \cdot \nabla^2 \mathbf{B} dV \left[\int_V \mathbf{B}^2 dV \right]^{-1}, \quad (13)$$

where M is the total magnetic energy. A similar quantity can be obtained for the reconnection-based dynamo by adding the contributions of all reconnection events to the magnetic energy release:

$$\gamma_r = \frac{d \ln M}{dt} = \frac{1}{8\pi M \tau} \sum_{i=1}^{N_\tau} B_i^2 S_i L_i, \quad (14)$$

where τ is a time interval during which N_τ reconnections occur (we take τ to be equal to ten time steps; individual reconnection events occur in a single time step), and B_i , S_i and L_i are the magnetic field strength, the cross-sectional area and length of the reconnected (and thus removed) flux tube segment associated with a particle number i . From our assumption of frozen flux, $B_i S_i = \psi = \text{const}$, the total magnetic energy M is,

$$M = \sum_{i=1}^N \frac{B_i^2}{8\pi} S_i L_i = \frac{\psi}{8\pi} \sum_{i=1}^N B_i L_i, \quad (15)$$

where N is the number of discretisation points in the system, and

$$\gamma_r = \tau^{-1} \sum_{i=1}^{N_\tau} B_i L_i \left[\sum_{i=1}^N B_i L_i \right]^{-1}. \quad (16)$$

The initial condition for the induction equation is obtained by Gaussian smoothing of the magnetic field in the ropes (this procedure preserves $\nabla \cdot \mathbf{B} = 0$). To evolve the induction equation, we use the Pencil Code [13] on a 256^3 mesh in a periodic box.

Figure 4 shows the energy release rates in simulations where the growth rate of the magnetic field is $\sigma = 0.16$ in both simulations (with the unit time l_0/u_0). The dashed

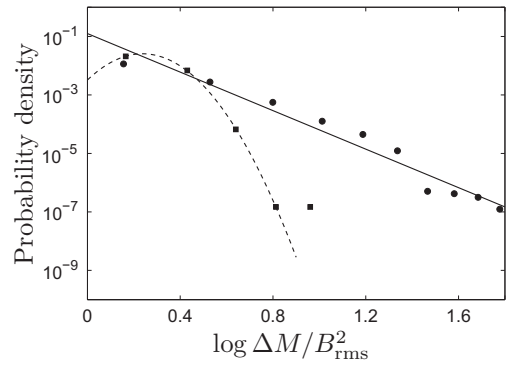


Figure 5: Probability density for the normalized magnetic energy release in individual reconnection events, $\Delta M/B_{\text{rms}}^2$, from the time series of Fig. 4, for the flux rope dynamo (circles) and the diffusive dynamo with the same magnetic field growth rate and velocity field form (squares). A power-law fit to the former and a Gaussian fit to the latter are shown solid and dashed, respectively

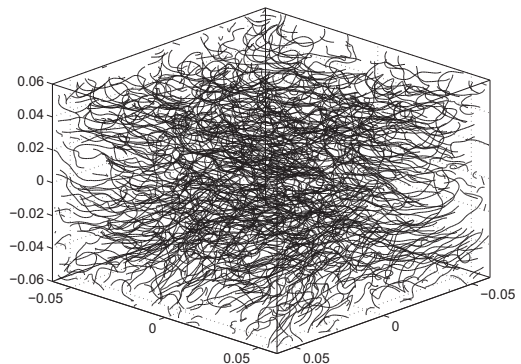


Figure 6: A snapshot of the system of quantised vortex filaments during the statistically steady state ($t = 6$ s) seen in Fig. 7

line shows the energy release rate from a simulation of induction equation with magnetic Reynolds number, $R_m = UL/\eta = 1200$, which has the mean energy release rate $\gamma_i \approx 2.4$. The solid line shows the corresponding results from the flux rope dynamo, with the mean value plotted as a dashed horizontal line. The mean value of the energy release rate from the reconnecting flux rope dynamo is $\gamma_r \approx 23$, an order of magnitude larger. Also note strong fluctuations in the energy release rate from the reconnection model, which are absent in the solutions of the induction equation.

A remarkable feature of the energy release in the filament dynamo model is that its probability distribution has a power law as shown in Fig. 5, $f(x) \propto x^{-s}$, where $x = \Delta M/B_{\text{rms}}^2$ is the magnetic energy released in a reconnection event normalized to the mean magnetic energy, with the slope $s \approx 3.3$. A similar exponent arises in a reconnection model for the corona [14] where, however, dynamo action is not included. Thus, weak ‘flares’ dominate the energy release in our reconnection-based system, as in the Parker’s nanoflare model of coronal heating [15].

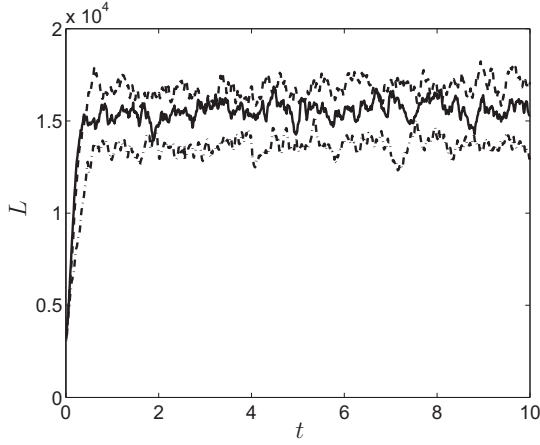


Figure 7: Vortex line density L (cm^{-2}) vs time t (s) shown for differing normal fluid Reynolds numbers (Re_n): $\text{Re}_n = 22.7$ (dot-dashed line), $\text{Re}_n = 57.1$ (solid line), and $\text{Re}_n = 112.9$ (dashed line)

7 Velocity statistics in quantum turbulence

We now present the results of the simulations of quantum turbulence, with an imposed turbulent normal fluid, using the KS model. Our initial system is a set of random vortex loops in a periodic cube of size D . The mutual friction between the system of quantised vortices and the ‘turbulent’ normal fluid leads to a rapid growth in the total length of the filaments, Λ , and hence the vortex line density $L = \Lambda/D^3$. Eventually the line density saturates, as dissipation due to reconnections balances energy input from the normal fluid, and a statistically steady state is reached, as is seen in Fig. 7; figure 6 shows a snapshot of the system in this state.

We calculate the velocity field induced by the quantised vortices, Eq. (9) at points on a 512^2 Cartesian mesh in the xy -plane ($z = 0$). This procedure is repeated for the KS flow, Eq. (12). We take the Fourier transform of these velocity fields to calculate the energy spectra for both the normal and superfluid components. These spectra are displayed in Fig. 8. The imposed Kolmogorov spectrum is clearly visible in the energy spectrum of the normal fluid. It is also clear, at large scales, that the energy spectrum of the quantum fluid is classical in its nature, with a $k^{-5/3}$ scaling; this result has also been reported experimentally [16]. Whilst one may expect this at finite temperatures due to the coupling to the normal fluid, this remarkable feature of quantum turbulence has also been seen in numerical simulations at zero temperature [17].

Despite the classical nature of the superfluid energy spectrum, the statistics of superfluid velocity components display power-law behaviour. The probability density functions (normalized histogram, or PDF for short) scale as $\text{PDF}(v_{s,i}) \propto v_{s,i}^b$ ($i = 1, 2, 3$) with average exponent $b = -3.1$, see Fig. 9. This scaling was observed in turbulent helium experiments [18], and was also recently calculated in turbulent atomic condensates [19]; its cause is the singular nature of the superfluid vorticity [19]. The vortex line velocity ds/dt obeys non-Gaussian scaling too. The statistics of velocity components in ordinary turbulence, on the contrary, are Gaussian [20].

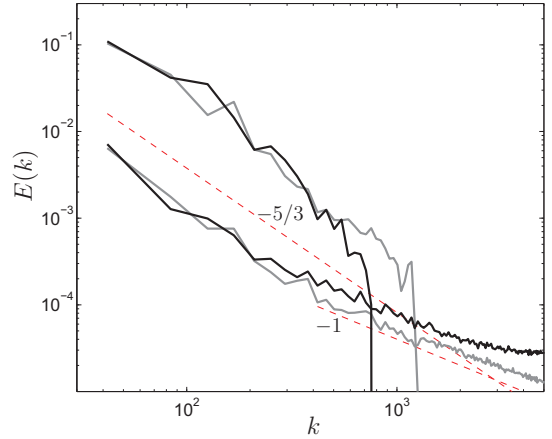


Figure 8: Normal fluid’s (upper two lines) and superfluid’s (lower two lines) energy spectrum $E(k)$ vs k (cm^{-1}). Grey lines: $\text{Re}_n = 112.9$ ($L = 8889 \text{ cm}^{-2}$, $k_\ell = 2\pi/\ell = 592 \text{ cm}^{-1}$); black lines: $\text{Re}_n = 49.85$ ($L = 7058 \text{ cm}^{-2}$, $k_\ell = 527 \text{ cm}^{-1}$). Dashed lines: $k^{-5/3}$ (top) and k^{-1} (bottom) scalings

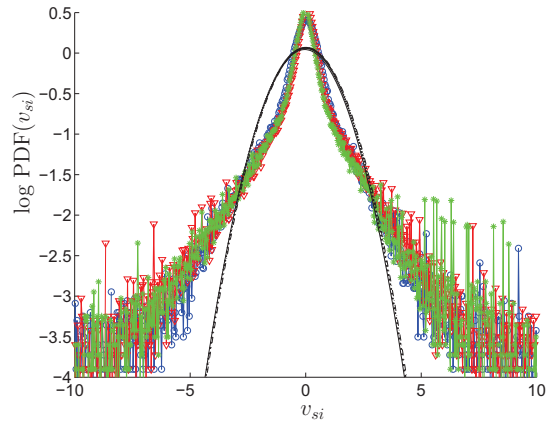


Figure 9: PDF of superfluid velocity components (cm/s) v_{sx} (blue circles), v_{sy} (red triangles) and v_{sz} (green asterisks) sampled over the vortex-points. The overlapping black dotted, dash dotted and solid lines are respectively the Gaussian fits to the same data, $\text{gPDF}(v_{s,i}) = (1/(\sigma\sqrt{2\pi})) \exp(-(v_{s,i} - \tilde{\mu})^2/(2\sigma^2))$, ($i = 1, 2, 3$) where σ and $\tilde{\mu}$ are the standard deviation and the mean

8 Summary

We have shown that filament models provide efficient methods to simulate complex physical systems, reproducing experimental and observational phenomena. Furthermore we have shown that the KS model, a ‘synthetic’ turbulent field, can be used to model the turbulent system our filaments exist in. Indeed the analytic form of the KS flow particularly suits the Lagrangian nature of the filament method as no interpolation of the velocity field is required.

In the magnetic flux rope model, where magnetic dissipation is suppressed at all scales exceeding the reconnection length, the rate of conversion of magnetic energy into heat in the reconnection dynamo is a order of magnitude larger than in the corresponding diffusion-based dynamo. This result, here obtained for a kinematic dynamo, can have serious implications for the heating of rarefied, hot plasmas where magnetic reconnections dominate over magnetic diffusion such as the corona of the sun and star, galaxies and accretion. In contrast to the fluctuation dynamo based on magnetic diffusion, the probability distribution function of the energy released in the flux-rope dynamo has a power law form not dissimilar to that observed for the solar flares.

The quantum turbulence calculations presented reproduce the main observed features, including the classical $k^{-5/3}$ Kolmogorov energy spectrum, thought to be associated with large-scale, energy-containing polarization of vortex lines. We have also reproduced the the observation of non-Gaussian velocity statistics which distinguish quantum turbulence from its classical analogue.

References

- [1] A. I. Gomez de Castro, R. E. Pudritz, and P. Bastien, *ApJ* **476**, 717 (1997).
- [2] C. T. Russell, E. R. Priest, and L. C. Lee, Washington DC American Geophysical Union Geophysical Monograph Series **58** (1990).
- [3] C. Barenghi, R. Donnelly, and W. Vinen, *Quantized vortex dynamics and superfluid turbulence*, Lecture notes in physics, Springer, 2001.
- [4] E. Priest and T. Forbes, *Magnetic Reconnection*, Cambridge University Press, Cambridge, UK, 2000.
- [5] M. Paoletti, M. Fisher, and D. Lathrop, *Physica D* **239**, 1367 (2010).
- [6] J. Koplik and H. Levine, *Phys. Rev. Lett.* **71**, 1375 (1993).
- [7] R. Feynman, Elsevier, 1955, volume 1 of *Progress in Low Temperature Physics*, pp. 17 – 53.
- [8] A. W. Baggaley, C. F. Barenghi, A. Shukurov, and K. Subramanian, *Astron. Nachr* **331** (2010).
- [9] K. W. Schwarz, *Phys. Rev. B* **38**, 2398 (1988).
- [10] C. F. Barenghi, R. J. Donnelly, and W. F. Vinen, *Journal of Low Temperature Physics* **52**, 189 (1983).
- [11] D. R. Osborne, J. C. Vassilicos, K. Sung, and J. D. Haigh, *Phys. Rev. E* **74**, 036309 (2006).
- [12] S. Childress and A. Gilbert, *Stretch, Twist, Fold: The Fast Dynamo*, Springer, Berlin, 1995.
- [13] A. Brandenburg, *Comp. Phys. Comm.* **147**, 471 (2002).
- [14] D. Hughes, M. Paczuski, R. O. Dendy, P. Helander, and K. G. McClements, *Phys. Rev. Lett.* **90**, 131101 (2003).
- [15] E. N. Parker, *The Astrophysical Journal* **264**, 642 (1983).
- [16] J. Maurer and P. Tabeling, *EPL (Europhysics Letters)* **43**, 29 (1998).
- [17] T. Araki, M. Tsubota, and S. K. Nemirovskii, *Phys. Rev. Lett.* **89**, 145301 (2002).
- [18] M. S. Paoletti, M. E. Fisher, K. R. Sreenivasan, and D. P. Lathrop, *Phys. Rev. Lett.* **101**, 154501 (2008).
- [19] A. C. White, C. F. Barenghi, N. P. Proukakis, A. J. Youd, and D. H. Wacks, *Phys. Rev. Lett.* **104**, 075301 (2010).
- [20] A. Vincent and M. Meneguzzi, *J. Fluid Mech.* **225**, 1 (1991).

SYNTHETIC TURBULENCE VIA THE MINIMAL LAGRANGIAN MAP

C. Rosales

*Department of Mechanical Engineering,
Universidad Técnica Federico Santa María, Chile*

1 The Minimal Lagrangian Map

Several approaches have been introduced for the generation of synthetic turbulence, understood as the construction of field variables having characteristic features of turbulent fluctuations, but computable at reduced cost compared with a numerical solution of Navier-Stokes equations. These methods have been based on stochastic processes, multiplicative constructions or restricted dynamics (Refs. [1]-[5], for example). Some of them are limited to one-dimensional signals, while those producing three-dimensional velocity fields give basically Gaussian statistics, and do not reproduce the non-Gaussianity of turbulent flows. The non-Gaussian statistics is a crucial feature of turbulence and has important consequences on its dynamics. The development of essential nonlinearities, such as the predominance of vortex stretching and the self-amplification of the strain rate, are directly related to it, as well as phase coherency of Fourier modes. These phase correlations imply coherence of motions, which manifest in the typical structure of a turbulent field, characterized by locally organized flow patterns, at different scales. In contrast, synthetic Gaussian fields present only incoherent disorderly motion. All these factors imply that when synthetic Gaussian turbulence is employed as initial condition or inlet boundary condition in numerical simulations, it dissipates very quickly, and thus a significant part of the total simulation time (or of the computational domain in the second case) has to be used for the regeneration of realistic turbulence.

Here we present a method that has been introduced and studied in detail in Refs. [6]-[8]. This approach has been called “Minimal Turnover Lagrangian Map” (MTLM) and it has shown to be able to generate three-dimensional synthetic fields endowed with many realistic turbulent characteristics for velocity fields as well as for passive scalar variables. The basic idea is to build a velocity field by distorting an initially random field over a hierarchy of spatial scales as described below. At each scale, the deformation is equivalent to the inertial advection of fluid particles during the local characteristic time scale (“turnover time”) according to Kolmogorov phenomenology. The field is kept solenoidal by projecting onto its divergence-free part.

If we consider a system of fluid particles in which all interactions among them are suppressed (i.e. no pressure or viscous effects), the equation of motion reduces to the Riemann equation

$$\partial_t \mathbf{u} + \mathbf{u} \cdot \nabla \mathbf{u} = 0, \quad (1)$$

corresponding to material points moving with constant velocity \mathbf{u} in Lagrangian coordinates. A fluid particle at position \mathbf{x} at $t = 0$ is simply mapped to

$$\mathbf{X}(t) = \mathbf{x} + t\mathbf{u}(\mathbf{x}, 0), \quad (2)$$

(whence the Lagrangian map denomination), where t is

a parameter of the map, while

$$\mathbf{u}(\mathbf{X}(t), t) = \mathbf{u}(\mathbf{x}, 0). \quad (3)$$

Even though the motion of a single particle under this equations is rather trivial, consideration to an ensemble of them leads to interesting and highly non-trivial results. Similarly, if there is a scalar property θ passively advected by this velocity field, its transport equation simplified in a consistent way with (1) is

$$\partial_t \theta + \mathbf{u} \cdot \nabla \theta = 0, \quad (4)$$

where diffusion effects are excluded. Hence, the scalar is carried along by the fluid particles unchanged: $\theta(\mathbf{X}(t), t) = \theta(\mathbf{x}, 0)$.

To resemble the multiscale nature of turbulence these mappings are applied over a hierarchy of spatial scales $\ell_n = 2^{-n}\ell_0$, $n = 1, \dots, M$, with ℓ_0 being of the order of the turbulence integral scale, L , and the number M of scales is such that $\ell_M \sim \eta$, where η is the Kolmogorov length scale. Since the procedure applied to the velocity and the scalar are similar, the generic variable ϕ is used here to denote the vector \mathbf{u} or the scalar θ . For each scale ℓ_n (or level n in the sequence), the field ϕ is decomposed into low-pass and high-pass filtered parts:

$$\phi(\mathbf{x}) = \phi_n^<(\mathbf{x}) + \phi_n^>(\mathbf{x}) \quad ; \quad \phi = \mathbf{u}, \theta. \quad (5)$$

The low-pass filtered fields $\phi_n^<$ are obtained by filtering, in wavenumber space, the fields obtained at the previous scale ℓ_{n-1} : $\widehat{\phi}_n^<(\mathbf{k}) = H(\pi/\ell_n - k)\widehat{\phi}_{n-1}(\mathbf{k})$, where $\widehat{\cdot}$ denotes Fourier-transformed quantities, and H is the Heaviside function. For the first scale, the initial fields ϕ_0 are generated by specifying Fourier modes with random phases and amplitudes modulated to match prescribed spectra, $E(k)$ and $E_\theta(k)$, for the energy and the scalar variance respectively. In the case of the velocity, the field is also made solenoidal.

These low-pass filtered fields are distorted by displacing fluid particles located at positions $\mathbf{x}_0 \equiv \mathbf{x}(t = 0)$ over a grid with mesh spacing ℓ_n , to new positions \mathbf{X} given by (2),

$$\phi_n^<(\mathbf{X}) = \phi_n^<(\mathbf{x}_0) \quad ; \quad \mathbf{X} = \mathbf{x}_0 + t_n \mathbf{u}_n^<(\mathbf{x}_0), \quad (6)$$

where the parameter t_n is determined as

$$t_n = \frac{\ell_n}{u_{\text{rms},n}^<}, \quad (7)$$

and $u_{\text{rms},n}^<$ is the root-mean-square value for $u_n^<$. New field values, $\bar{\phi}_n^<$, at Eulerian positions \mathbf{x} on the regular grid are obtained by interpolation from the values of $\phi_n^<(\mathbf{X})$ for the surrounding fluid particles which have come into the neighborhood of \mathbf{x} after the mapping. The interpolation used is a simple weighted average over a

ball of radius ℓ_n around \mathbf{x} , with the inverse of the distance $|\mathbf{X} - \mathbf{x}|$ as the weighting function:

$$\bar{\phi}_n^<(\mathbf{x}) = \frac{\sum_{|\mathbf{X}-\mathbf{x}|<\ell_n} |\mathbf{X}-\mathbf{x}|^{-1} \phi_n^<(\mathbf{X})}{\sum_{|\mathbf{X}-\mathbf{x}|<\ell_n} |\mathbf{X}-\mathbf{x}|^{-1}}. \quad (8)$$

As indicated before, the total deformation introduced at each scale is equivalent to a displacement during the phenomenological turnover time $\tau_n \approx \langle \varepsilon \rangle^{-1/3} \ell_n^{2/3}$, where $\langle \varepsilon \rangle$ is the mean energy dissipation rate. As given by (7), t_n is shorter than τ_n so that in order to accumulate the appropriate deformation at each scale, the mapping is applied several times before advancing to the next scale (the reason is to allow the introduction of spatial distortion but to avoid at the same time a re-randomization of the field by destruction of the coherency introduced by the mapping at the previous scales; in any case, the number of repetitions of the mapping for each scale is quite small).

After each mapping displacement, the resulting interpolated fields are rescaled in order to keep constant their r.m.s. values. Additionally, the velocity field is restored to its zero divergence condition. This is done by projection in wavenumber space, and thus the solenoidal velocity field, $\tilde{\mathbf{u}}_n^<$, to be used for the next particle displacement has as Fourier transform

$$\widehat{\tilde{\mathbf{u}}_n^<} = |\widehat{\tilde{\mathbf{u}}_n^<}| \frac{\mathbf{P}\widehat{\tilde{\mathbf{u}}_n^<}}{|\mathbf{P}\widehat{\tilde{\mathbf{u}}_n^<}|}, \quad (9)$$

where $P_{ij} = \delta_{ij} - k_i k_j / k^2$. This is the only difference between the procedure applied to $\mathbf{u}_n^<$ and the procedure applied to $\theta_n^<$, which do not require any projection in Fourier space.

After deforming the fields at scale ℓ_n , their Fourier modes $\widehat{\phi}_n^<$ are rescaled to maintain the prescribed spectra, and combined with their high-pass-filtered parts, which have remained unaltered at the current scale:

$$\widehat{\phi}(\mathbf{k}) = \widehat{\phi}_n^<(\mathbf{k}) \sqrt{E_\phi(k) / \frac{1}{2} \sum_{|q|=k} |\widehat{\phi}_n^<(\mathbf{q})|^2} + \widehat{\phi}_n^>(\mathbf{k}). \quad (10)$$

These recomposed fields contain now hierarchically deformed scales up to a size ℓ_n , and smaller random scales which are still Gaussian. They are the starting fields for the next scale ℓ_{n+1} . Progressing in this way until reaching ℓ_M gives rise to the synthetic velocity and scalar fields.

2 Synthetic Turbulent Fields

Several synthetic fields were computed on a periodic cubic domain $[0, 2\pi]^3$ with $N = 256^3, 512^3$ and 1024^3 points. The spectra for kinetic energy and scalar variance prescribed are standard Kolmogorov and Kolmogorov-Oboukhov functions, with exponential decay in the dissipative range. For the scalar θ an inertial-convective regime is taken, with Schmidt number $Sc = 0.7$. Parameters in these functions (such as viscosity, diffusivity) are specified such that the Kolmogorov scale is of the order of the mesh resolution. With this, the equivalent Reynolds numbers \Re_λ (on Taylor scale) for the synthetic turbulence are in a range from 159 to 406.

Figure 1 shows the probability distribution (normalized by their standard deviations) of the longitudinal

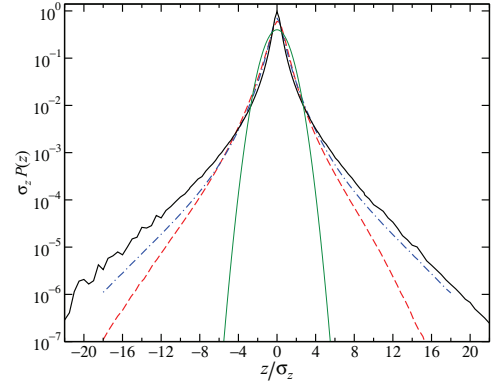


Figure 1: PDF for: $\nabla_{\parallel} \mathbf{u}$ (dashed line), $\nabla_{\perp} \mathbf{u}$ (dotted-dashed line) and $\nabla \theta$. Synthetic field at $Re_\lambda = 406$ with 1024^3 generating points. Green line is a normalized Gaussian distribution

N	Re_λ	Pe_λ	$F[\nabla \theta]$	$F[\nabla_{\parallel} \mathbf{u}]$
256^3	159	111	11.65	6.37
512^3	255	178	20.01	7.94
1024^3	406	284	28.45	10.33

Table 1: Flatness for scalar and longitudinal velocity gradients, obtained at different Reynolds numbers. Pe_λ is the Péclet number

velocity gradient ($\nabla_{\parallel} \mathbf{u}$), the transverse velocity gradient ($\nabla_{\perp} \mathbf{u}$) and the scalar gradient ($\nabla \theta$) for a case with $Re_\lambda = 406$. These distributions depart strongly from the Gaussian and resemble quite well those observed in real turbulence, with tails that flare out tending to adopt a stretched exponential form. While the PDFs for $\nabla_{\perp} \mathbf{u}$ and $\nabla \theta$ are symmetrical, the PDF for the $\nabla_{\parallel} \mathbf{u}$ presents negative skewness. For all the cases computed this skewness is about -0.4 , which agrees very well with the known value in Navier-Stokes turbulence. It is apparent also from the figure that the flatness for $\nabla \theta$ is higher than for the velocity gradients. Some values for the flatness are given in Table 1, and they match correctly experimental values for Re_λ and Pe_λ in these ranges [9, 10].

In order to probe the statistics of these fields at all (not just the smallest) scales, they are evaluated also for the longitudinal and transverse velocity increments, δu_r and δv_r , respectively, and for the scalar increments, $\delta \theta_r$, as a function of points separation r . Results for the PDF of $\delta \theta_r$ are shown in Fig. 2. In this plot, the separations are expressed as multiples of the smallest resolved scale ℓ_M . The strong non-gaussianity seen at dissipative scales

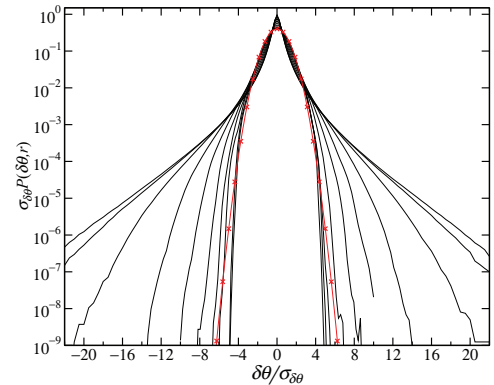


Figure 2: PDF of normalized scalar increments for $Re_\lambda = 406$. The curves are for $r/\ell_M = 2^n$ ($n = 0, \dots, 8$) and 500 from the outermost. Red line with \times marks is a Gaussian

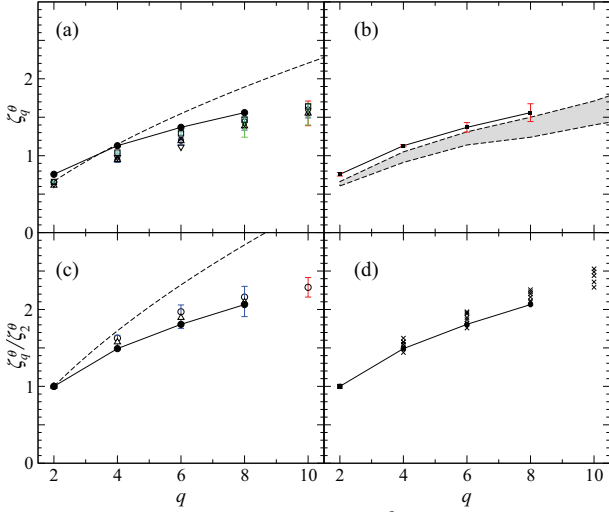


Figure 6: Scaling exponents for $S_q^\theta(r)$. In all the plots the black symbols joined by a line correspond to a MTLM synthetic field. See text

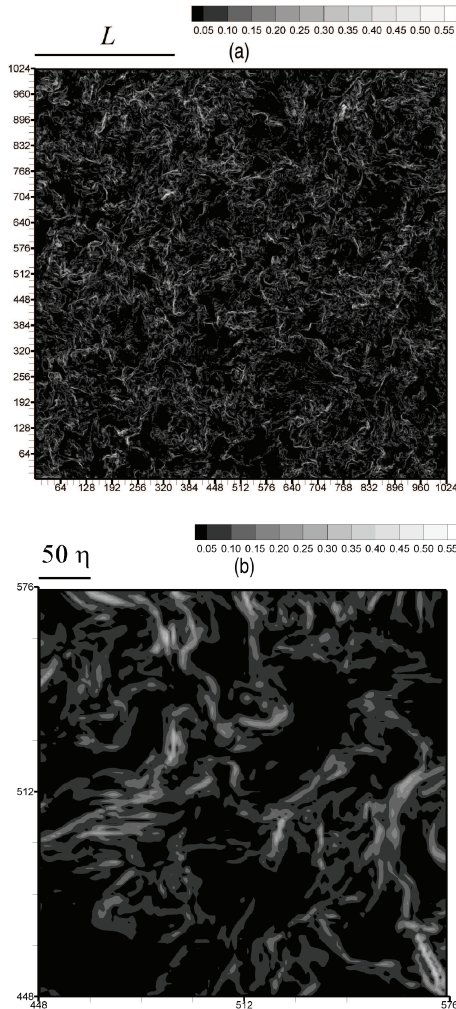


Figure 7: Contours of isovorticity. (a) 1024^2 slice for a MTLM field at $Re_\lambda = 047$. (b) Zoom-in view for the 128^2 central subregion in (a)

In Fig. 6d these relative exponents are shown again including all the data in Fig. 6a normalized in this way. The dashed lines in Fig. 6 correspond to scaling given by the Kraichnan model [20]. Although the advection of passive scalars by that kind of synthetic Gaussian velocity fields can lead also to the growth of some degree of intermittency, it seems that not only repeated stochastic

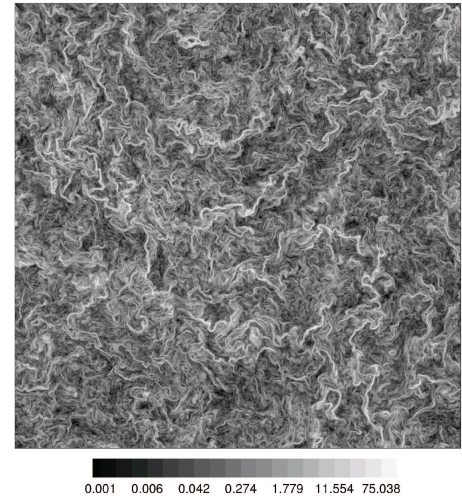
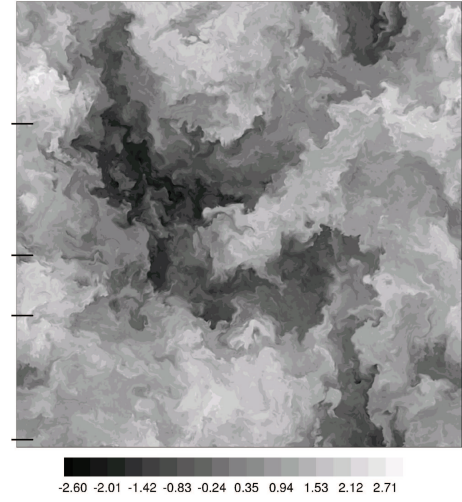


Figure 8: (a) Contours of θ/θ_{rms} (marks on left are the locations for 1D horizontal profiles in Fig. 9) (b) Contours of $\chi/\langle\chi\rangle$ at the same plane

straining suffices to replicate the anomalous scaling of turbulence, but also the spatial structure and coherency of the velocity field, acquired by self-distortion, has an important role.

Figure 7 shows contour of vorticity magnitude, ω , for a slice of a 1024^3 -node synthetic field (the values are normalized by the maximum ω in the field). The figure depicts also the integral scale L and a multiple of Kolmogorov scale η , according to the parameters used in the synthesizing. The strong vorticity appears concentrated in thin elongated regions, with a very small space-filling volume fraction, embedded in a background of weak ω , resembling the spatial distribution of vorticity in turbulent flows. By contrast, for a Gaussian synthetic field, ω has a structureless fine-grained uniform pattern. A more detailed analysis of these structures has shown that they are akin to vortex sheets [6, 7].

Contours of θ normalized by its r.m.s. value can be seen in Fig. 8a. The characteristic aspect of inertial-convective turbulent mixing is apparent, with θ organized into regions of relatively low fluctuations separated by large jumps. The magnitude of these jumps is of the order of θ_{rms} . Convoluted boundaries for the regions of relative homogeneity extend for distances of the order of the integral scale, contrasting with the abrupt variation of θ in the direction transversal to them. Figure 9 provides another view by means of one-dimensional cuts through Fig. 8a, displaying clearly the sharp jumps in θ through the boundaries separating region of lower

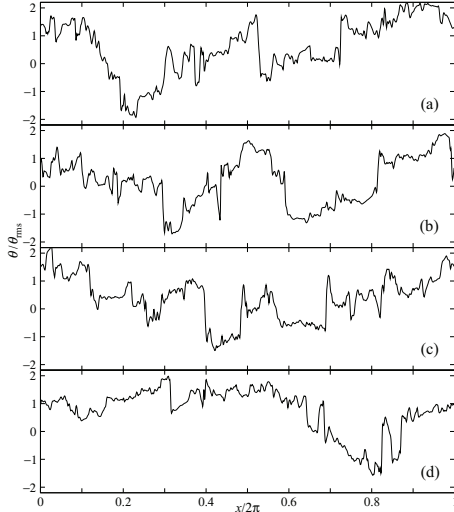


Figure 9: Horizontal cuts through Fig. 8a, at the positions marked in that figure

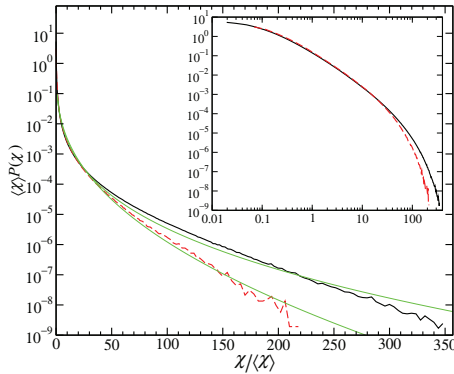


Figure 10: PDF of normalized χ . Solid line: $Re_\lambda = 406$, dashed line: $Re_\lambda = 255$. The inset shows the same curves in logarithmic scale. Green curve is fitting of the form $\chi^{-1/2} \exp(-a\chi^b)$

fluctuations. All this features are very similar to the “ramp-cliff” structures observed in real turbulence. In Fig. 8 it is also shown the scalar dissipation normalized by its mean, illustrating the high intermittency of χ . Note that the tone scale for χ contours is exponential, so that the long light-toned convolute d lines that stand out from the darker background are extremely sharpened ridges taking place along the same locations where the “cliffs” for θ occur. The PDF of χ is shown in Fig. 10. The low dissipation range ($\langle \chi \rangle < 1$) is the most probable, as can be seen in the inset. These low dissipation regions are plausibly associated with the “plateaux” among the cliffs. There are however rare but very intense deviations above the mean, corresponding to the ridges whose spatial distribution is shown in Fig. 8b. Figure 10 also shows least-square fittings of the form $P(\chi) \propto \chi^{-1/2} \exp(-a\chi^b)$. This kind of function is to be expected when $\nabla\theta$ has as PDF with stretched exponential form, and it has been observed to fit well the results in Navier-Stokes turbulence, as it occurs here over a considerable range. The PDF for the energy dissipation was found also to have a qualitatively similar distribution.

Several characteristics of the statistical geometry associated with the structure of the synthetic MTLM fields have been studied, for the velocity and vorticity fields, as well as for aspects that stem from the joint statistics of velocity and scalar fields (Refs. [6]-[8]), showing an interesting similarity with Navier-Stokes turbulence. Figure 11 shows for example the PDF for the cosines of the an-

gles between the vorticity vector ω and the eigenvectors $\{\mathbf{e}^{(1)}, \mathbf{e}^{(2)}, \mathbf{e}^{(3)}\}$ of the strain-rate tensor S_{ij} , designated according to the ordering of the corresponding eigenvalues $\lambda_1 < \lambda_2 < \lambda_3$, obtained for 256^3 -node synthetic field with $Re_\lambda = 84$, using an early form of the procedure [6]. Even in that case, the preferential alignment of ω with the intermediate eigenvector $\mathbf{e}^{(2)}$ is very well reproduced, and the whole turbulent distribution for the three angles is well captured.

Finally Fig. 12 presents the joint PDF of the second and third invariants of the velocity gradient tensor, Q and R , normalized by the magnitude of the rate of strain $Q_* \equiv Q/\langle S_{ij}S_{ij} \rangle$, $R_* \equiv R/\langle S_{ij}S_{ij} \rangle^{3/2}$, for the same velocity field of Fig. 11. The distribution matches well the observations in real turbulence, with predominance of the probability in the $(R < 0, Q > 0)$ and $(R > 0, Q < 0)$ quadrants, and with a tail extending into this last quadrant along the line $(\frac{1}{2}R)^2 + (\frac{1}{3}Q)^3 = 0$ which separates the region of real and complex eigenvalues of $\partial_j u_i$. The concentration along this side of the line is an indication of bi-axial extension as the prevalent state of strain. Such situation is associated in turbulence with the formation of vortex sheets and the production of negative skewness for longitudinal velocity gradients. In this synthetic case it can be attributed to the squeezing of fluid elements into sheet-like structures produced by the Lagrangian map.

3 Conclusion and Perspectives

A review of some of the features of the MTLM synthetic turbulence approach have been presented. This procedure is intended as an inexpensive method for generating surrogate fields for numerical simulations. It is remarkable that many nontrivial characteristics of turbulence can still be reproduced when some of the physical process involved have been simplified and split in this very drastic way. Two of the key components of turbulence are the self-distortion of the velocity field and the multi-scale structure of the field. The first is provided in this case by the Lagrangian map, while the second is explicitly introduced by the hierarchy of scales used. The construction is essentially kinematical, while the enforcing of the solenoidal condition introduces a pressure-like effect that limits the compressive action of the mapping in the regions of fluid elements convergence leading to the formation of structures similar to vortex sheets. It has been already shown that this kind of synthetic field produces the correct time evolution when used as initial condition in turbulence numerical simulations [6]. Current ongoing work has as objective the extension of the method to

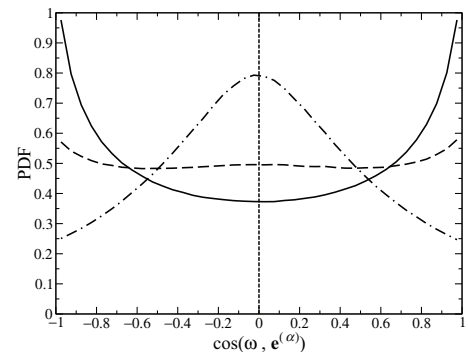


Figure 11: PDF of the cosine of the angle between ω and eigenvectors $\mathbf{e}^{(1)}$ (dashed line), $\mathbf{e}^{(2)}$ (solid line) and $\mathbf{e}^{(3)}$ (dashed-dotted line) of the strain-rate tensor

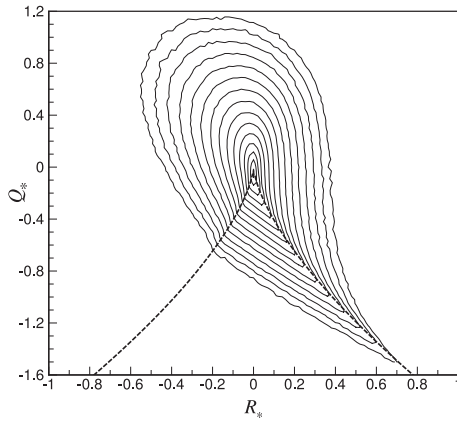


Figure 12: Joint PDF of normalized invariants Q_* and R_*

inhomogeneous anisotropic turbulence and the application of the method for the generation of synthetic inlet turbulence in spatially developing flows.

Acknowledgments

This research was supported by the Chilean National Commission for Scientific & Technological Research (CONICYT) through Project FONDECYT 11080025.

References

- [1] L. Chevillard, R. Robert and V. Vargas, *A stochastic representation of the local structure of turbulence*, EPL, **89**, 54002 (2010).
- [2] K. J. Falconer and T. C. O’Neil, *Vector-valued multifractal measures*, Proc. R. Soc. Lond. A, **452**, 1433 (1996).
- [3] A. Jujena, D. P. Lathrop, K. R. Sreenivasan, and G. Stolovitski, *Synthetic turbulence*, Phys. Rev. E, **95**, 5179 (1994).
- [4] L. Biferale, G. Boffeta, A. Celani, A. Crisanti, and A. Vulpiani, *Mimicking a turbulent signal: Sequential multifractal processes*, Phys. Rev. E, **57**, R6261 (1998).
- [5] S. Basu, E. Foufoula-Georgiou and F. Porté-Agel, *Synthetic turbulence, fractal interpolation and large-eddy simulation*, Phys. Rev. E, **70**, 026310 (2004).
- [6] C. Rosales and C. Meneveau, *A minimal multi-scale Lagrangian map approach to synthesize non-Gaussian turbulent vector fields*, Phys. Fluids, **18**, 075104 (2006).
- [7] C. Rosales and C. Meneveau, *Anomalous scaling and intermittency in three-dimensional synthetic turbulence*, Phys. Rev. E, **78**, 016313 (2008).
- [8] C. Rosales, *Synthetic three-dimensional turbulent passive scalar fields via the minimal Lagrangian map*, Phys. Fluids, **23**, 075106 (2011).
- [9] K. R. Sreenivasan and R. A. Antonia, *The phenomenology of small-scale turbulence*, Annu. Rev. Fluid Mech. **29**, 435 (1997).
- [10] Z. Warhaft, *Passive scalars in turbulent flows*, Annu. Rev. Fluid Mech., **32**, 203, (2000).
- [11] T. Watanabe and T. Gotoh, *Statistics of a passive scalar in homogeneous turbulence*, New J. Phys., **6**, 40 (2004).
- [12] T. Gotoh, D. Fukayama and T. Nakano, *Velocity statistics in homogeneous steady turbulence obtained using a high-resolution direct numerical simulation*, Phys. Fluids, **14**, 1065 (2002).
- [13] O. N. Boratav and R. B. Pelz, *Coupling between anomalous velocity and passive scalar increments in turbulence*, Phys. Fluids, **10**, 2122 (1998).
- [14] E. Lévêque, G. Ruiz-Chavarria, C. Baudet, and S. Ciliberto, *Scaling laws for the turbulent mixing of a passive scalar in the wake of a cylinder*, Phys. Fluids, **11**, 1869 (1999).
- [15] S. Chen and R. H. Kraichnan, *Simulations of a randomly advected passive scalar field*, Phys. Fluids, **10**, 2867 (1998).
- [16] L. Mydlarski and Z. Warhaft, *Passive scalar statistics in high-Péclet-number grid turbulence*, J. Fluid Mech., **358**, 135 (1998).
- [17] R. A. Antonia, E. J. Hopfinger, Y. Gagne and F. Anselmet, *Temperature structure functions in turbulent shear flows*, Phys. Rev. A, **30**, 2704 (1984).
- [18] C. Meneveau, K. R. Sreenivasan, P. Kailasnath, and M. S. Fan, *Joint multifractal measures: Theory and applications to turbulence*, Phys. Rev. A, **41**, 894 (1990).
- [19] F. Moisy, H. Willaime, J. S. Andersen and P. Tabeling, *Passive scalar intermittency in low temperature helium flows*, Phys. Rev. Lett., **86**, 4827 (2001).
- [20] R. H. Kraichnan, *Anomalous scaling of a randomly advected passive scalar*, Phys. Rev. Lett., **72**, 1016 (1994).

ERCOFTAC Workshops and Summer Schools

Title	Location	Date	Organisers	Email addresses
3rd International workshop on the turbulent combustion of sprays	Rottmannsaal, Heidelberg-Handschuhsheim, Germany	2/09/2012	Gutheil, E. Masri, A. R. Mastorakos, E. Merci, B. Raman, V. Roekaerts, D. Sadiki, A.	gutheil@iwr.uni-heidelberg.de assaad.masri@sydney.edu.au em257@eng.cam.ac.uk bart.merci@ugent.be v.raman@mail.utexas.edu d.j.e.m.roekaerts@tudelft.nl sadiki@ekt.tu-darmstadt.de
9 th European fluid mechanics conference	Rome, Italy	9/09/2012 - 13/09/2012	Verzicco, R.	verzicco@uniroma2.it
13 th Workshop on two-phase flow predictions	Halle, Germany	17/09/2012 - 20/09/2012	Sommerfeld, M.	martin.sommerfeld@iw.uni-halle.de
20 th Polish national fluid dynamics conference	Gliwice, Poland	17/09/2012 - 20/09/2012	Wroblewski, W. Drobniaak, S.	wlodzimierz.wroblewski@polsl.pl drobniaak@imc.pcz.czesl.pl
Coronary arterial and microvascular fluid structure interactions: evolving concepts and investigative approaches	London, UK	17/09/2012	Kilner, P.	richard.seoud-ieo@ercoffac.org AdmMgr-ercoffac@live.com
Computational aeroacoustics (course)	Munich, Germany	30/10/2012 - 31/10/2012	Bailly, C.	richard.seoud-ieo@ercoffac.org
ERCOFTAC Workshop – Direct and Large Eddy Simulation 9	Dresden, Germany	3/04/2013 - 5/04/2013	Fröhlich, J. Giesecke, A. Rüdiger, F. Stiller, J.	Jochen.Froehlich@tu-dresden.de
Unsteady Separation in Fluid-Structure Interaction	Mykonos, Greece	17/06/2013 - 22/06/2013	Braza, M. Bottaro, A.	mariana.braza@imff.fr alessandro.bottaro@unige.it

ERCOFTAC Special Interest Groups

1. Large Eddy Simulation

Geurts, B.J.
University of Twente, Holland.
Tel: +31 53 489 4125
b.j.geurts@utwente.nl

4. Turbulence in Compressible Flows

Dussauge, Jean-Paul
IUSTI, Marseille
jean-paul.dussauge@polytech.univ-mrs.fr

5. Environmental CFD

Armenio, V.
Università di Trieste, Italy.
Tel: +39 040 558 3472
Fax: +39 040 572 082
armenio@dica.units.it

10. Transition Modelling

Dick, E.,
University of Ghent, Belgium.
Tel: +32 9 264 3301
Fax: +32 9 264 3586
erik.dick@ugent.be

12. Dispersed Turbulent Two Phase Flows

Sommerfeld, M.
Martin-Luther University, Germany.
Tel: +49 3461 462 879
Fax: +49 3461 462 878
martin.sommerfeld@iw.uni-halle.de

14. Stably Stratified and Rotating Flows

Redondo, J.M.
UPC, Spain.
Tel: +34 93 401 7984
Fax: +34 93 401 6090
redondo@fa.upc.edu

15. Turbulence Modelling

Jakirlic, S.
Darmstadt University of Technology, Germany.
Tel: +49 6151 16 3554
Fax: +49 6151 16 4754
s.jakirlic@sla.tu-darmstadt.de

20. Drag Reduction and Flow Control

Choi, K-S.
University of Nottingham, England.
Tel: +44 115 9513 792
Fax: +44 115 9513 800
kwing-so.choi@nottingham.ac.uk

24. Variable Density Turbulent Flows

Anselmet, F.
IMST, France.
Tel: +33 4 91 505 439
Fax: +33 4 91 081 637
anselmet@irphe.univ-mrs.fr

28. Reactive Flows

Tomboulides, A.
University of Western Macedonia
tel: (+30-24610) 56630
fax: (+30-24610) 56631
atompoulidis@uowm.gr
ananiast@auth.gr

32. Particle Image Velocimetry

Stanislas, M.
Ecole Centrale de Lille, France.
Tel: +33 3 20 337 170
Fax: +33 3 20 337 169
Michel.Stanislas@ec-lille.fr

33. Transition Mechanisms, Prediction and Control

Hanifi, A.
FOI, Sweden.
Tel: +46 8 5550 3197
Fax: +46 8 5550 3397
ardeshir.hanifi@foi.se

34. Design Optimisation

Giannakoglou, K.
NTUA, Greece.
Tel: +30 210 772 1636
Fax: +30 210 772 3789
kgianna@central.ntua.gr

35. Multipoint Turbulence Structure and Modelling

Cambon, C.
ECL Ecully, France.
Tel: +33 4 72 186 161
Fax: +33 4 78 647 145
claude.cambon@ec-lyon.fr

36. Swirling Flows

Braza, M.
IMFT, France.
Tel: +33534322839
Fax: +33534322992
braza@imft.fr

37. Bio-Fluid Mechanics

Poelma, C.
Delft University of Technology, Holland.
Tel: +31 15 278 2620
Fax: +31 15 278 2947
c.poelma@tudelft.nl

38. Micro-thermofluidics

Borhani, N.
EPFL, Switzerland.
Tel: +41 21 693 3503
Fax: +41 21 693 5960
navid.borhani@epfl.ch

39. Aeroacoustics

Bailly, C.
Ecole Centrale de Lyon, France.
Tel: +33 4 72 186 014
Fax: +33 4 72 189 143
christophe.bailly@ec-lyon.fr

40. Smoothed Particle Hydrodynamics

Le Touze, D.
Ecole Centrale de Nantes, France
Tel: +33 2 40 37 1512
Fax: +33 2 40 37 2523
David.LeTouze@ec-nantes.fr

41. Fluid Structure Interaction

Longatte, E.
EDF, France.
Tel: +33 1 30 87 80 87
Fax: +33 1 30 87 77 27
elisabeth.longatte@edf.fr

42. Synthetic Models in Turbulence

Nicolleau, F.
University of Sheffield, England.
Tel: +44 114 22 27867
Fax: +44 114 22 27890
f.nicolleau@sheffield.ac.uk

43. Fibre Suspension Flows

Hämäläinen, J.
Lappeenranta University of Technology, Finland.
Tel: +358 40 596 1999
jari.hamalainen@lut.fi

44. Fundamentals and Applications of Fractal Turbulence

Fortune, V.
Université de Poitiers, France.
Tel: +33 5 49 45 40 44
Fax: +33 5 49 45 36 63
veronique.fortune@lea.univ-poitiers.fr

45. Uncertainty Quantification in Industrial Analysis and Design

Meyers, J.
Katholieke Universiteit Leuven, Belgium.
Tel: +32 16 322 502
Fax: +32 16 322 985
johan.meyers@mech.kuleuven.be

ERCOFTAC Pilot Centres

Alpe – Danube – Adria

Dr. Gergely Kristóf
Department of Fluid Mechanics,
Budapest University of Technology and
Economics
Bertalan L. utca 4-6
1111 Budapest, Hungary
Tel: +36 1 463 4073
Fax: +36 1 463 4072
kristof@ara.bme.hu

Belgium

Geuzaine, P.
Cenaero,
CFD Multi-physics Group,
Rue des Frères Wright 29,
B-6041 Gosselies,
Belgium.
Tel: +32 71 919 334
philippe.geuzaine@cenaero.be

Czech Republic

Bodnar, T.
Institute of Thermomechanics AS CR,
5 Dolejskova,
CZ-18200 Praha 8,
Czech Republic.
Tel: +420 224 357 548
Fax: +420 224 920 677
bodnar@marian.fsik.cvut.cz

France – Henri Bénard

Cambon, C.
Ecole Centrale de Lyon.
LMFA,
B.P. 163,
F-69131 Ecully Cedex,
France.
Tel: +33 4 72 18 6161
Fax: +33 4 78 64 7145
claude.cambon@ec-lyon.fr

France South

Braza, M.
IMF Toulouse,
CNRS UMR – 5502,
Allée du Prof. Camille Soula 1,
F-31400 Toulouse Cedex,
France.
Tel: +33 534 322 839
Fax: +33 534 322 992
Braza@imft.fr

France West

Danaila, L.
CORIA, University of Rouen,
Avenue de l'Université BP12,
76801 Saint Etienne du Rouvray
France.
Tel: +33 2 32 95 37 02
luminita.danaila@coria.fr

Germany North

Gauger, N.R.
Computational Mathematics Group
RWTH Aachen University
Schinkelstr. 2
D-52062 Aachen
Germany
Tel: +49 241 80 98 660
Fax: +49 241 80 92 600
gauger@mathces.rwth-aachen.de

Germany South

PD Dr. Ing. Stefan Becker
Universität Erlangen, IPAT
Cauerstr. 4
91058 Erlangen
Germany
Tel: +49 9131 85 29451
Fax: +49 9131 85 29449
sb@ipat.uni-erlangen.de

Greece

Papailiou, K.D.
National Tech. University of Athens,
Laboratory of Thermal Turbomachines,
9 Iroon Polytechniou,
P.O. Box 64069,
Gr-15710 Athens,
Greece.
Tel: +30 210 772 1634
Fax: +30 210 772 1658
kpapail@lnt.ntua.gr

Iberian East

Onate, E.
Universitat Politecnica de Catalunya,
Edificio C-1, Campus Norte,
Gran Capitan s/n,
E-08034 Barcelona,
Spain.
Tel: +34 93 401 6035
Fax: +34 93 401 6517
onate@cimne.upc.es

Iberian West

Vassilis T.
Research Professor of Fluid Mechanics
School of Aerospace Engineering
Technical University of Madrid (UPM)
Tel: +34 91 336 32 98
Fax: +34 91 336 32 95
vassilios.theofilis@upm.es

Italy

Martelli, F.
University of Florence,
Department of Energy,
Via Santa Marta 3,
I-50139 Firenze, Italy.
Tel: +39 055 479 6237
Fax: +39 055 479 6342
francesco.martelli@unifi.it

Netherlands

Ooms, G.
J.M. Burgerscentrum,
National Research School for Fluid
Mechanics,
Mekelweg 2,
NL-2628 CD Delft,
Netherlands.
Tel: +31 15 278 1176
Fax: +31 15 278 2979
g.ooms@tudelft.nl

Nordic

Wallin, S.
Swedish Defence Research Agency FOI,
Information and Aeronautical Systems,
S-16490 Stockholm,
Sweden.
Tel: +46 8 5550 3184
Fax: +46 8 5550 3062
stefan.wallin@foi.se

Poland

Rokicki, J.
Warsaw University of Technology,
Inst. of Aeronautics & Applied Mechanics,
ul. Nowowiejska 24,
PL-00665 Warsaw,
Poland.
Tel: +48 22 234 7444
Fax: +48 22 622 0901
jack@meil.pw.edu.pl

Switzerland

Jenny, P.
ETH Zürich,
Institute of Fluid Dynamics,
Sonneggstrasse 3, ML H 38,
CH-8092 Zürich,
Switzerland.
Tel: +41 44 632 6987
Fax: +41 44 632 1147
jenny@ifd.mavt.ethz.ch

United Kingdom

Standingford, D.
Zenotech Ltd.
University Gate East, Park Row,
Bristol, BS1 5UB
England.
Tel: +44 117 302 8251
Fax: +44 117 302 8007
david.standingford@zenotech.com



Best Practice Guidelines for Computational Fluid Dynamics of Dispersed Multi-Phase Flows

Editors

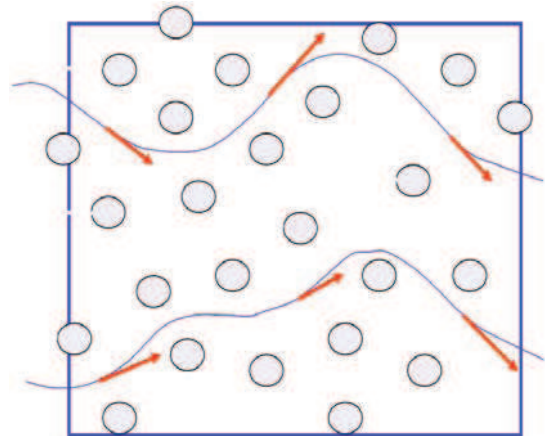
Martin Sommerfeld, Berend van Wachem
&
René Oliemans

The simultaneous presence of several different phases in external or internal flows such as gas, liquid and solid is found in daily life, environment and numerous industrial processes. These types of flows are termed multiphase flows, which may exist in different forms depending on the phase distribution. Examples are gas-liquid transportation, crude oil recovery, circulating fluidized beds, sediment transport in rivers, pollutant transport in the atmosphere, cloud formation, fuel injection in engines, bubble column reactors and spray driers for food processing, to name only a few. As a result of the interaction between the different phases such flows are rather complicated and very difficult to describe theoretically. For the design and optimisation of such multiphase systems a detailed understanding of the interfacial transport phenomena is essential. For single-phase flows Computational Fluid Dynamics (CFD) has already a long history and it is nowadays standard in the development of air-planes and cars using different commercially available CFD-tools.

Due to the complex physics involved in multiphase flow the application of CFD in this area is rather young. These guidelines give a survey of the different methods being used for the numerical calculation of turbulent dispersed multiphase flows. The Best Practice Guideline (BPG) on Computational Dispersed Multiphase Flows is a follow-up of the previous ERCOFTAC BPG for Industrial CFD and should be used in combination with it. The potential users are researchers and engineers involved in projects requiring CFD of (wall-bounded) turbulent dispersed multiphase flows with bubbles, drops or particles.

Table of Contents

1. Introduction
2. Fundamentals
3. Forces acting on particles, droplets and bubbles
4. Computational multiphase fluid dynamics of dispersed flows
5. Specific phenomena and modelling approaches
6. Sources of errors
7. Industrial examples for multiphase flows
8. Checklist of 'Best Practice Advice'
9. Suggestions for future developments



Copies of the Best Practice Guidelines can be acquired electronically from the ERCOFTAC website:

www.ercoftac.org

Or from:

ERCOFTAC CADO
Crown House
72 Hammersmith Road
London W14 8TH, United Kingdom

Tel: +44 207 559 1429

Fax: +44 207 559 1428

Email: Richard.Seoud-ieo@ercoftac.org

The price per copy (not including postage) is:

ERCOFTAC members

First copy	Free
Subsequent copies	45 Euros
Students	30 Euros

Non-ERCOFTAC academics	90 Euros
Non-ERCOFTAC industrial	180 Euros